Sulfur Poisoning of Pd and PdCu Alloy Hydrogen Separation Membranes

Submitted in partial fulfillment of the requirements for

the degree of

Doctor of Philosophy

in

Chemical Engineering

Casey P. O'Brien

B.S., Chemical Engineering, University of Colorado at Boulder

Carnegie Mellon University
Pittsburgh, PA

May, 2011

Acknowledgements

To begin, I would like to thank the National Energy Technology Laboratory for funding my Ph.D. work and for providing me with access to their facilities. I would also like to thank the people that have helped me with my Ph.D. research, most importantly my Ph.D. advisors Professor Andy Gellman and Dr. Jim Miller, and my project manager at NETL, Dr. Bryan Morreale I would also like to thank the rest of my Ph.D. committee: Professors John Kitchin, Myung Jhon, and Sridhar Seetharaman. I would also like to thank Dr. Bret Howard, Dr. Esteban Broitman, Dr. Vladimir Pushkarev, Dr. Petro Kondratyuk, and William Michalak for their help. Thanks again to all that have helped me complete my Ph.D. work.

Many of the results in Chapter 2 were adapted with permission from references [1, 2].

Abstract

Separation of high purity H_2 from coal-derived syngas is a key unit process in next generation gasification processes. Dense Pd and $Pd_{47}Cu_{53}$ (mol%) alloy membranes are promising candidates for separating H_2 from mixed gases due to their rare combination of high permeability and high selectivity to H_2 separation. However, ppm concentrations of H_2S, a coal gasification byproduct, can severely inhibit hydrogen transport across Pd and $Pd_{47}Cu_{53}$ membranes in the temperature range that the membrane would need to be operated in a gasification process (~500 to ~700 K). This thesis is an experimental investigation of hydrogen transport (H_2 dissociation and H atom permeation) across Pd and $Pd_{47}Cu_{53}$ alloy membranes. The objective of this thesis was to understand how H_2S inhibits hydrogen transport across Pd and $Pd_{47}Cu_{53}$ alloy membranes.

H_2S slows hydrogen transport across Pd membranes mainly by producing a Pd_4S film on the surface of the Pd membrane that is about an order-of-magnitude less permeable to hydrogen than Pd. In contrast to Pd, the $Pd_{47}Cu_{53}$ alloy is resistant to bulk sulfidation; H_2S slows hydrogen transport across $Pd_{47}Cu_{53}$ by decreasing the rate of H_2 dissociation on the $Pd_{47}Cu_{53}$ surface. H_2S also decreases the rate of H_2 dissociation on the Pd_4S surface, but not as significantly as that on the $Pd_{47}Cu_{53}$ surface.

At high temperatures (~900 K), the rate of hydrogen permeation through the $Pd_{47}Cu_{53}$ alloy is not significantly affected by 1000 ppm H_2S. It is likely that the sulfur tolerance exhibited by the $Pd_{47}Cu_{53}$ alloy at high temperatures is due to its resistance to bulk sulfidation. However, our results indicate that the $Pd_{47}Cu_{53}$ alloy is not thermodynamically resistant to sulfidation. Thin metal (Fe, Ni, Co, Cr, Mo, Pt) films on the surface of the $Pd_{47}Cu_{53}$ alloy catalyzed its corrosion to $Pd_{13}Cu_3S_7$ and Cu_2S during exposure to H_2S, which suggests that sulfidation of $Pd_{47}Cu_{53}$ is kinetically limited by a surface reaction. This result is important because understanding why $Pd_{47}Cu_{53}$ alloy membranes are resistant to sulfidation may lead to the development of membrane materials that can tolerate the harsh conditions of coal gasification processes.

Table of Contents

List of Tables

List of Figures

Chapter 1

General Introduction

1.1 Summary

Dense Pd membranes are promising candidates for hydrogen separation from mixed gases because of their near-infinite selectivity for H_2 separation and very high permeability. However, Pd membranes are not viable for hydrogen separation from sulfur-containing gases, such as those derived from coal gasification, because H_2S can severely inhibit hydrogen transport across Pd membranes in concentrations as little as ppm-levels. PdCu alloys show sulfur tolerance relative to Pd at high temperatures (~900 K), but hydrogen transport across PdCu alloys is also severely inhibited by H_2S at low temperatures (~600 K). The objective of this thesis is to understand how H_2S slows hydrogen transport across Pd and PdCu membranes. In this chapter, the literature relevant to the objective of this thesis is reviewed and the scope of this thesis is outlined.

1.2 Hydrogen from coal gasification

About 45% of the electricity generated in the United States in 2009 was derived from coal, mainly coal combustion power plants, and that percentage is not expected to change significantly for at least 25 years [3]. However, coal combustion power plants utilize only about one-third of the energy available in coal and were responsible for about 36% of the total CO_2 emissions in the United States in 2008 [4]. Next generation gasification processes are being developed that will have better efficiency, reduced CO_2 emissions, and more versatility than coal combustion power plants.

In contrast to coal combustion, which uses the heat generated from burning coal to drive a steam turbine, coal gasification produces mainly CO and H_2 (syngas) which can be used in a variety of ways. Syngas can be used to generate electricity in a gas/steam turbine combined cycle; or to produce liquid fuels via Fischer-Tropsch synthesis; or to produce H_2 for use in fuel cells or as a chemical commodity. H_2 production from syngas requires an increase in the H_2 yield via the water gas shift reaction, $CO + H_2O \leftrightarrow CO_2 + H_2$, followed by H_2 separation from the H_2/CO_2 gas mixture.

Pressure swing adsorption is currently the most common industrial process for high purity (99.99%) H_2 separation, however, operating costs of pressure swing adsorption are high [5]. Alternatively, a membrane that is selectively permeable to H_2 would greatly decrease the cost of hydrogen separation if the membrane could be operated at temperatures near that of the water-gas shift reaction (~500 to ~700 K). There are several different types of H_2 separation

membranes, including dense polymeric, microporous ceramic, dense ceramic, porous carbon, and dense metallic membranes. Of these types of membranes, only dense metallic membranes are capable of producing very high purity H_2 at temperatures near that of the water-gas shift reaction [6]. Pd and Pd alloy membranes, in particular, have received significant attention for such applications because of their very high permeability to H_2 [7-10].

1.3 Pd hydrogen separation membranes

Dense Pd membranes are capable of producing very high purity H_2 from mixed gases because of the unique way in which hydrogen crosses the membrane. Molecular H_2 dissociatively adsorbs on the catalytically active Pd membrane surface, producing H atoms which are able to diffuse through the bulk of the Pd lattice and associatively desorb from the opposite surface [11]. Only H atoms permeate through dense Pd membranes at a significant rate, and a nearly infinite selectivity for hydrogen separation can be achieved by the use of dense Pd membranes [9]. The rare combination of the very high H_2 dissociation activity of the Pd surface [12-16] and the very high H atom permeability of bulk Pd [8, 9, 17] distinguishes the performance of pure Pd membranes from other pure metal membranes [17].

Pure Pd membranes are not viable options for H_2 separation from coal-derived gases because H_2S, a coal gasification byproduct, severely reduces the rate of hydrogen permeation across Pd membranes in concentrations as little as ppm-levels [9, 18, 19]. The effect of H_2S on H_2 permeation through Pd has been

studied by many groups over a wide range of temperatures (593-1173 K) and H_2S concentrations (4 to 6200 ppm H_2S) [9, 18, 20-26]. H_2S severely inhibited H_2 transport across Pd in nearly all of the experimental conditions studied [9, 18, 20, 22-26]. For example, immediately following exposure to 4 ppm H_2S, the rate of H_2 permeation through a Pd membrane was reduced to about 40% of its baseline H_2 flux and continued to decrease to less than 30% of its baseline H_2 flux over the next several days [18]. In many of the cited studies [9, 22, 25, 26], a palladium-sulfide (Pd_4S) film was observed on the surfaces of the Pd membranes following H_2S exposure. In one study [21], H_2S did not significantly reduce the rate of H_2 permeation through a Pd membrane, which was attributed to the thermodynamic instability of Pd_4S at the temperature (1173 K) of the experiment. Thus, there is circumstantial evidence that the formation of Pd_4S is at least partially responsible for retarding H_2 permeation through Pd: Pd_4S is observed when H_2 permeation through Pd is inhibited by H_2S, but H_2S has no effect on H_2 permeation through Pd at conditions where Pd_4S is unstable. The fundamental mechanisms by which H_2S and/or Pd_4S inhibit H_2 permeation through Pd, however, are not very clear.

By correlating Pd_4S growth kinetics to the decay in H_2 flux through a Pd membrane during H_2S exposure, Morreale *et al.* [9, 25] suggested that the very low H atom permeability of Pd_4S was responsible for the decline in H_2 flux during H_2S exposure. Others have suggested that H_2S inhibits H_2 transport through Pd by poisoning the catalytic surface for H_2 dissociation, either by blocking H atom adsorption sites [20, 22, 24, 27] or by increasing the barrier to H_2 dissociation [27, 28] or both. For example, by studying the effect of pre-adsorbed sulfur on the

temperature programmed desorption of H_2 on a Pd(100) surface, Burke and Madix found that each adsorbed sulfur atom blocks about 4 H atom adsorption sites. In addition to blocking H atom adsorption sites, density functional theory calculations by Wilke and Scheffler [27, 28] show that pre-adsorbed sulfur atoms on the Pd(100) surface increase the barrier to H_2 dissociation.

In summary, Pd hydrogen separation membranes perform well in gas streams that do not contain H_2S. However, Pd membranes are not viable options for hydrogen separations from gas streams that contain H_2S, such as coal gasification product gases, because H_2S sulfides the bulk of Pd and severely inhibits hydrogen transport across Pd membranes. PdCu alloy hydrogen separation membranes are attractive alternatives to pure Pd membranes because of their sulfur tolerance relative to Pd [9, 29-31] and their high permeability to hydrogen [9, 10, 18]. A brief summary of the literature regarding PdCu alloy membranes is given in the next section.

1.4 PdCu alloy hydrogen separation membranes

The $Pd_{47}Cu_{53}$ (mol%) alloy is a particularly attractive alternative to pure Pd membranes due to its high permeability, which is similar to that of Pd in the ~600 to ~700 K temperature range [7, 9, 10] and its sulfur tolerance at high temperatures (~900 K) [7, 9, 19]. The high permeability of the $Pd_{47}Cu_{53}$ alloy is related to its crystal structure, which is body-centered-cubic (BCC) at temperatures less than ~700 K and face-centered-cubic (FCC) at temperatures

above ~800 K (see Figure 1.1) [32]. The H atom permeability of BCC $Pd_{47}Cu_{53}$ is about an order-of-magnitude greater than that of FCC $Pd_{47}Cu_{53}$ [7, 9].

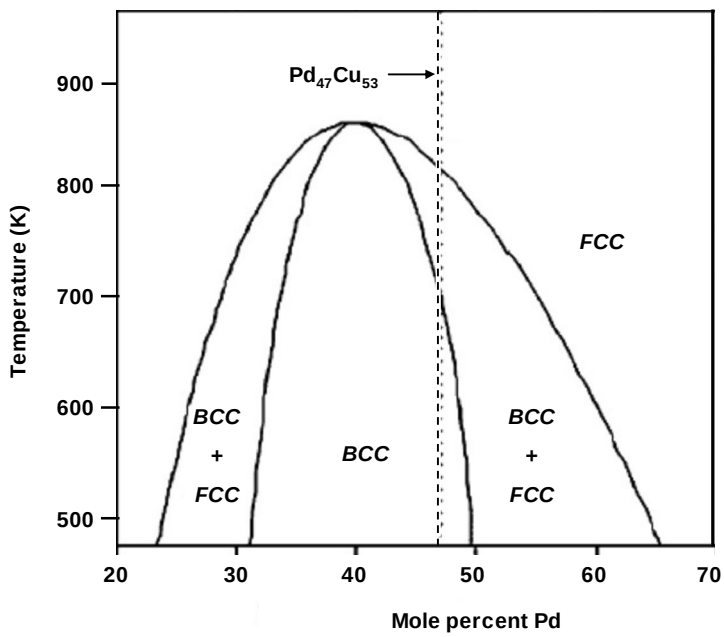

Figure 1.1 Pd-Cu phase diagram adapted from [32]. The $Pd_{47}Cu_{53}$ alloy has a body-centered-cubic (BCC) crystal structure at temperatures less than ~700 K and a face-centered-cubic (FCC) crystal structure at temperatures greater than ~800 K. In between ~700 K and ~800 K, the $Pd_{47}Cu_{53}$ alloy has mixed BCC/FCC crystal structure. The H atom permeability of BCC $Pd_{47}Cu_{53}$ is about an order-of-magnitude greater than that of FCC $Pd_{47}Cu_{53}$.

Aside from their relatively high permeability to H_2, the main interest in using PdCu alloy membranes for hydrogen separation from mixed gases is due to their sulfur tolerance relative to Pd [9, 18]. There have been several studies on

the effect of H_2S on hydrogen permeation through PdCu alloys [7, 9, 18, 19, 21, 22, 30, 33, 34]. The results of all of these studies will not be summarized here, but the results of the Ph.D. work of Morreale [9] are the primary motivation of this thesis and his work will be summarized here briefly. Morreale characterized the effect of 1000 ppm H_2S on hydrogen permeation through Pd, $Pd_{70}Cu_{30}$, $Pd_{47}Cu_{53}$, and $Pd_{40}Cu_{60}$ membranes in the 623 to 908 K temperature range. A summary of Morreale's results is presented in Figure 1.2, which shows the sulfur tolerance of Pd, $Pd_{70}Cu_{30}$, $Pd_{47}Cu_{53}$, and $Pd_{40}Cu_{60}$ membranes versus temperature. Sulfur tolerance is arbitrarily defined here as the ratio of the hydrogen flux through the Pd and PdCu membranes after 5 days of exposure to 1000 ppm H_2S in H_2 to the hydrogen flux measured during exposure to pure H_2:

$$\text{Sulfur Tolerance} = \frac{\text{H}_2 \text{ flux in 1000 ppm H}_2\text{S}}{\text{H}_2 \text{ flux in pure H}_2}.$$

In the 623 to 908 K temperature range, the H_2 flux through Pd after 5 days of exposure to 1000 ppm H_2S is about one-fifth the H_2 flux in pure H_2. The sulfur tolerance of the $Pd_{70}Cu_{30}$, $Pd_{47}Cu_{53}$, and $Pd_{40}Cu_{60}$ alloys is nearly zero at 623 K. Unlike Pd, however, the sulfur tolerance of $Pd_{70}Cu_{30}$, $Pd_{47}Cu_{53}$, and $Pd_{40}Cu_{60}$ increases with increasing temperature. At 908 K, all three PdCu alloys have sulfur tolerance relative to Pd and hydrogen transport through the $Pd_{47}Cu_{53}$ alloy is not significantly inhibited by 1000 ppm H_2S.

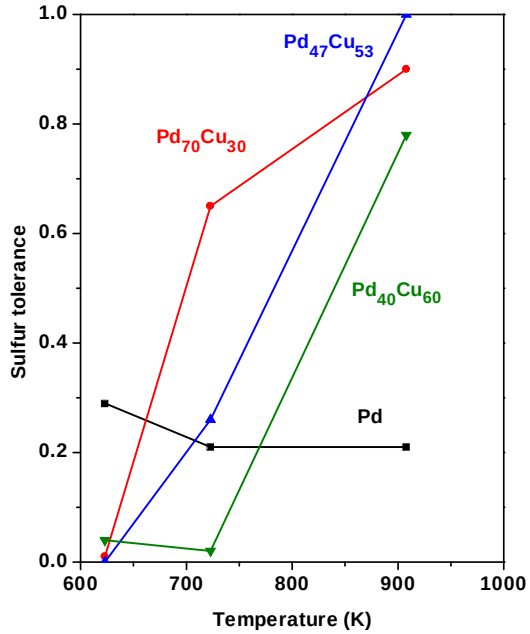

Figure 1.2 Sulfur tolerance (ratio of the H_2 permeation flux after 5 days of exposure to 1000 ppm H_2S to the H_2 permeation flux in pure H_2) of Pd, $Pd_{70}Cu_{30}$, $Pd_{47}Cu_{53}$, and $Pd_{40}Cu_{60}$ versus temperature (adapted from [4]). The sulfur tolerance of Pd is roughly constant (~0.2) in the 623 to 908 K temperature range. The sulfur tolerance of the PdCu alloys is ~0.0 at 623 K, but the sulfur tolerance of the PdCu alloys increases with temperature. The $Pd_{47}Cu_{53}$ alloy is completely sulfur tolerant at 908K.

Morreale also observed that the $Pd_{47}Cu_{53}$ and $Pd_{40}Cu_{60}$ alloys resisted bulk sulfidation in the 623 to 908 K temperature range [9]. The $Pd_{70}Cu_{30}$ alloy also resisted bulk sulfidation at 908 K, but there were two different sulfur products (Pd_4S and $Pd_{13}Cu_3S_7$) observed on the surface of the $Pd_{70}Cu_{30}$ alloy at 623 and 723 K. Another significant, and unexpected, result of Morreale's Ph.D work was a link between the presence of Fe-, Cr-, and Ni-sulfide particles on the surface of

PdCu alloys to improved sulfur tolerance. It is not clear how the Fe-, Cr-, and Ni-sulfide particles improved the sulfur tolerance of the PdCu alloys.

In summary, PdCu alloys are attractive alternatives to pure Pd membranes due to their high permeability and their sulfur tolerance relative to Pd at high temperature (~900 K). However, PdCu membranes are not viable for coal gasification processes because H_2S blocks hydrogen transport through PdCu membranes almost completely in the temperature range that the membrane would need to be operated (~500 to ~700 K).

1.5 Scope of the thesis

Although Pd and PdCu alloy membranes are not viable options for coal gasification processes, understanding how H_2S slows hydrogen transport through Pd and PdCu membranes, and why PdCu alloys are sulfur tolerant at high temperature, may lead to the development of advanced membrane materials that can tolerate the conditions of a coal gasification process. This thesis is an experimental investigation of hydrogen transport (H_2 dissociation and H atom permeation) across Pd and PdCu membrane. The aim of this thesis is to understand how H_2S slows hydrogen transport across Pd and PdCu membranes, and to understand why PdCu alloys are sulfur tolerant relative to Pd at high temperatures.

Pd and the $Pd_{47}Cu_{53}$ alloy have been used throughout this thesis as benchmarks for understanding hydrogen transport across dense metal membranes in the presence of H_2S. Two main experimental techniques were used in this

thesis. The rate of hydrogen permeation through Pd and $Pd_{47}Cu_{53}$ was measured in a membrane testing apparatus. A H_2-D_2 exchange experiment was developed in this thesis to investigate: (1) the effect of alloying Pd and Cu on the kinetics of H_2 dissociation and (2) the effect of H_2S on the rate of H_2 dissociation over Pd, $Pd_{47}Cu_{53}$, and $Pd_{70}Cu_{30}$ surfaces. The effect of H_2S on the bulk and surface compositions of Pd and $Pd_{47}Cu_{53}$ membranes was characterized by x-ray diffraction, x-ray photoelectron spectroscopy, and scanning electron microscopy.

Chapter 2

Experimental and Analytical Techniques

2.1 Summary

In this thesis, a combination of experimental and analytical techniques was used to investigate hydrogen transport across Pd and PdCu membranes. A membrane testing apparatus was used to measure the rate of H_2 permeation through Pd and $Pd_{47}Cu_{53}$ foil membranes during exposure to both pure H_2 and a 1000 ppm H_2S in H_2 gas mixture. A fixed bed H_2-D_2 exchange experiment was developed in this thesis to investigate the effect of H_2S on the rate of H_2 dissociation on Pd, $Pd_{70}Cu_{30}$, and $Pd_{47}Cu_{53}$ alloy surfaces. The effect of H_2S on the bulk and near-surface compositions of Pd and $Pd_{47}Cu_{53}$ was characterized by x-ray diffraction (bulk), scanning electron microscopy (bulk), and x-ray photoelectron spectroscopy (near-surface). A description of the experimental and analytical techniques, including the principles of operation of the analytical instruments, is given in this chapter.

2.2 Experimental techniques

2.2.1 Pd and $Pd_{47}Cu_{53}$ foil membrane testing

Hydrogen permeation through Pd and $Pd_{47}Cu_{53}$ foil membranes was measured using a membrane testing apparatus at the National Energy Technology Laboratory, which is shown schematically in Figure 2.1. Circular (~1.8 cm^2) membrane foils were cut from 25 µm thick Pd (Alfa Aesar, 99.9% metals purity) and 25 µm thick $Pd_{47}Cu_{53}$ (ATI Wah Chang, 99.0% metals purity) foils. The membranes were mounted into a Swagelok® VCR tube assembly and then installed in the membrane testing apparatus. The H_2 partial pressure in the retentate was varied from ~130 kPa to ~270 kPa while the permeated H_2 was collected at ambient pressure (~100 kPa). The temperature was measured using Omega type-K thermocouples positioned ~5 mm from the surface of each side of the membrane; the operating temperature was given by the average of the two temperatures. The H_2 flux through the membrane was measured using a bubble flowmeter (Alltech Digital Flowmeter Model 4074). Following data collection, the membranes were cooled to room temperature in He and Ar and then dismounted for characterization.

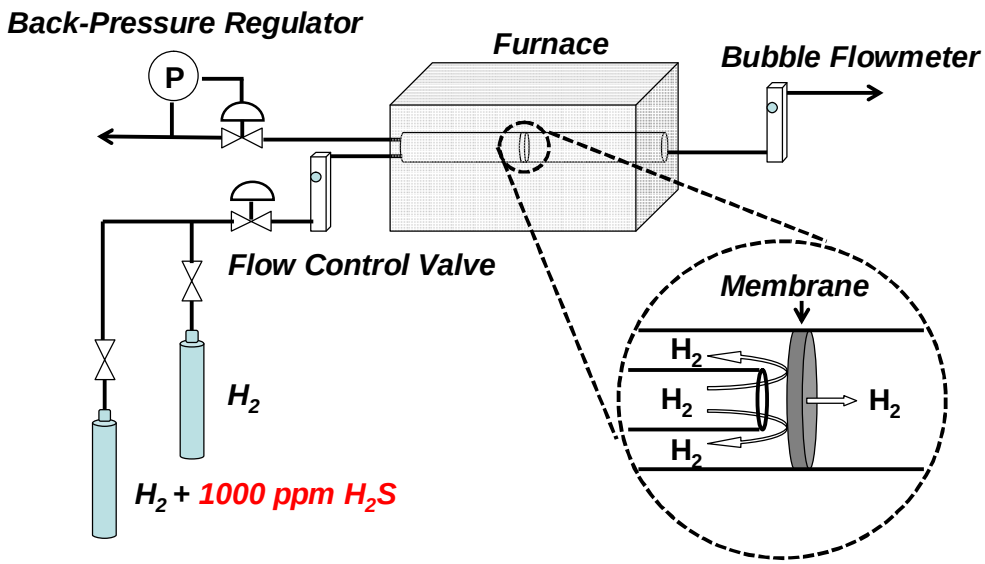

Figure 2.1 Schematic of the membrane foil testing apparatus. 25 µm thick Pd and $Pd_{47}Cu_{53}$ foil was mounted in a Swagelok® VCR tube assembly that was surrounded by a furnace. The foil membranes were exposed to flowing gases of pure H_2 or 1000 ppm H_2S in H_2 at elevated temperature and pressure while the permeated H_2 flux was measured with a bubble flowmeter at ambient pressure.

2.2.2 *H_2-D_2 exchange over Pd, Cu, $Pd_{70}Cu_{30}$, and $Pd_{47}Cu_{53}$*

The effect of H_2S on the kinetics of H_2 dissociation over Pd, $Pd_{70}Cu_{30}$, and $Pd_{47}Cu_{53}$ foil surfaces was investigated by a H_2-D_2 exchange experiment that was developed in this thesis. A schematic of the H_2-D_2 exchange reactor is shown in Figure 2.2.

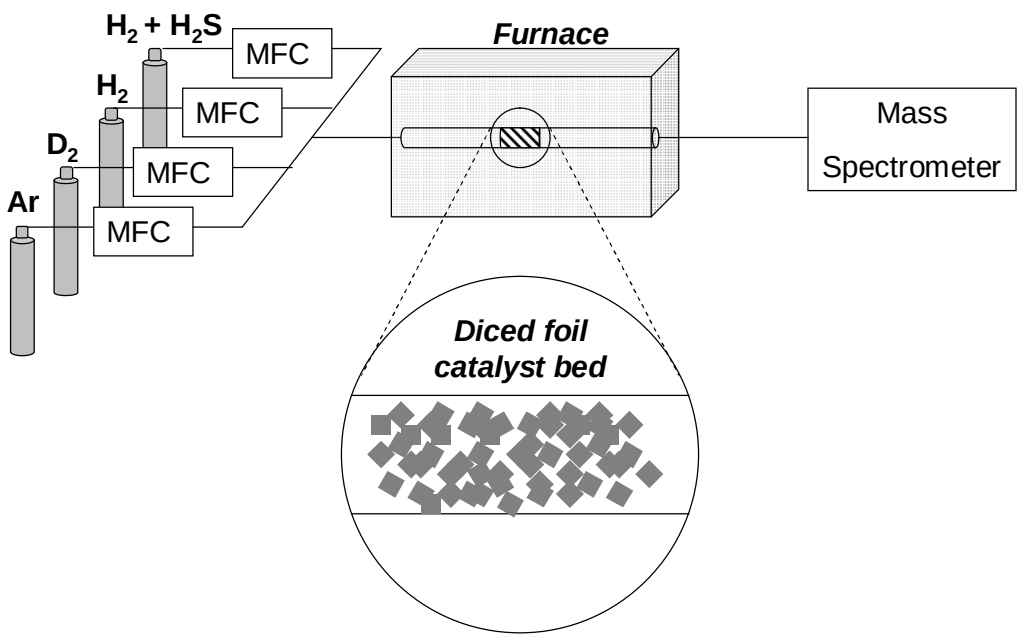

Figure 2.2 Schematic of the H_2-D_2 exchange reactor. Pd, Cu, $Pd_{70}Cu_{30}$, and $Pd_{47}Cu_{53}$ foil was diced into ~1 mm^2 pieces and packed into a quartz tube reactor surrounded by a tube furnace. H_2S+H_2/H_2/D_2/Ar were fed to the reactor while the product gas was analyzed by a mass spectrometer. The flow rates of H_2S+H_2, H_2, D_2, and Ar to the reactor were controlled with mass flow controllers (MFC). The concentration of H_2S in the feed gas was controlled by varying the relative flow rates of a H_2S+H_2 gas mixture and a pure H_2 gas cylinder.

H_2-D_2 exchange experiments were performed by flowing H_2, D_2, Ar and a H_2S/H_2 gas mixture through a 4 mm I.D. quartz tube reactor that was packed with

diced Pd, Cu, $Pd_{70}Cu_{30}$, or $Pd_{47}Cu_{53}$ foil while the product gas composition was analyzed by a mass spectrometer. The total surface area of each catalyst used in the experiments was ~19 cm^2. A metal wired fixed a thermocouple to the outside of the quartz tube reactor near the catalyst. A tube furnace (Barnstead/Thermolyne 211000) was used to heat the reactor. Mass flow controllers (Aalborg GFC 17) regulated the flow rates of H_2 (99.999%, Valley National Gases), D_2 (99.999%, Valley National Gases), Ar (99.999%, Valley National Gases), (1.09±0.02%H_2S)/98.9%H_2 (Matheson Tri-Gas), and (0.107±0.002ppmH_2S)/99.9%H_2 (Matheson Tri-Gas) to the catalyst bed. The H_2S concentration in the feed gas was controlled by diluting the H_2S/H_2 gas mixtures with pure H_2. A ~1 m long, 320 µm I.D. quartz capillary (Polymicro Technologies) was sealed into the outlet of the quartz tube reactor and the product gas was sampled by a ~15 cm long, 20 µm I.D quartz capillary (Polymicro Technologies) that was mounted to a vacuum chamber with a mass spectrometer (Stanford Research Systems, RGA 200).

2.3 Analytical techniques

2.3.1 X-ray diffraction

X-ray diffraction (XRD) was used to identify the bulk crystal structure and elemental composition of membrane foil samples. The basis of the XRD technique is that the atoms in a periodic crystal will scatter an incident beam of x-rays and constructive interference, or diffraction, will occur in definite directions that are related to the periodic arrangement of the atoms in the crystal lattice [35].

Figure 2.3 shows a schematic of the x-ray diffraction process. During XRD analysis of a foil sample, the incident angle of an x-ray beam with respect to the sample is varied continuously while the intensity of the diffracted x-ray beam is measured as a function of the incident angle. Peaks in the x-ray diffraction intensity occur at specific angles that are related to the spacing between crystal planes according to Bragg's Law [35]:

$$n\lambda = 2d_{\mathrm{hkl}} \sin\theta$$

where n is an integer, λ is the wavelength of the incident x-ray beam, d_{hkl} is the distance between the (hkl) crystal planes, and θ is the angle between the incident x-ray beam and the (hkl) crystal plane. A comparison of the x-ray diffraction pattern to a database allows the identification of crystalline compounds and crystalline structure.

X-ray diffraction (XRD) measurements of the foil surfaces were obtained using a PANalytical X'Pert Pro MPD powder diffractometer having a theta-theta configuration, a Cu x-ray source operated at 45 kV and 40 mA and an X'Celerator detector equipped with a monochromator. Patterns were recorded over a 2θ range of 30 to 90° at a step size of 0.02°. Foil samples were mounted on zero background quartz slides for analysis. Sample foils were not perfectly flat resulting in a slight peak shape distortion; however this distortion did not affect data interpretation.

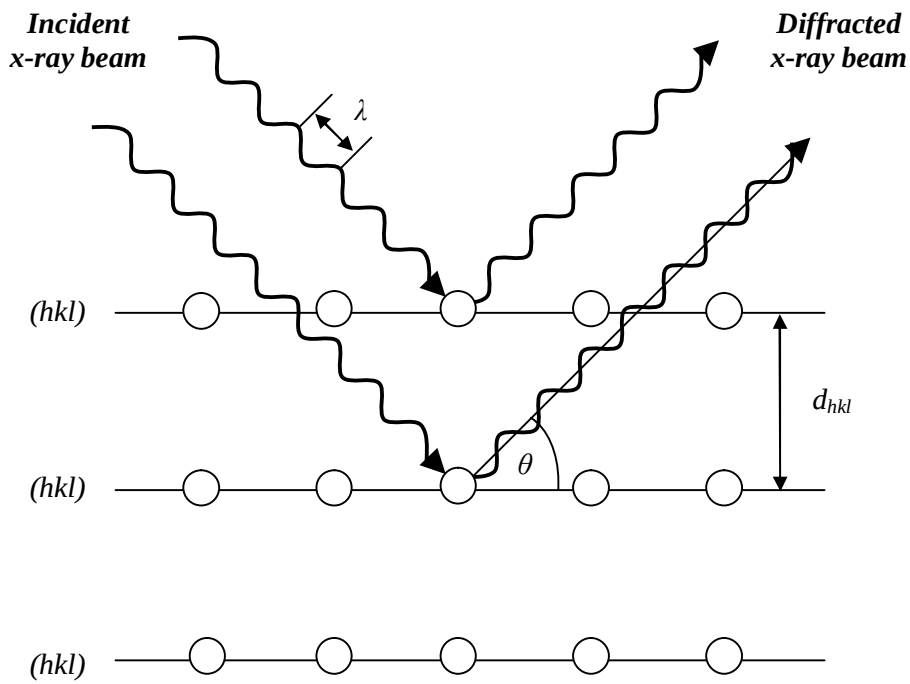

Figure 2.3 Schematic of the x-ray diffraction process. An incident x-ray beam is scattered by the atoms in a crystal and constructive interference, or diffraction, occurs in specific directions that are related to the periodic arrangement of the atoms in the crystal lattice according to Bragg's Law: $n\lambda = 2d_{hkl}\sin\theta$, where n is an integer, λ is the wavelength of the incident x-ray beam, d_{hkl} is the distance between the (hkl) planes in the crystal lattice, and θ is the angle between the incident x-ray beam and the (hkl) plane. Comparison of an x-ray diffraction pattern (scattering intensity versus 2θ) to a database allows for the identification of crystal structure and elemental composition.

2.3.2 X-ray photoelectron spectroscopy

X-ray photoelectron spectroscopy (XPS) was used to characterize the chemical composition in the near-surface region (~1 to 10 nm) of foil samples. XPS depth profiling was used to characterize the chemical composition profile of foil samples as a function of depth into the sample up to ~200 nm. The basis of the XPS technique, which is shown schematically in Figure 2.4, is that an x-ray beam incident on a solid sample ejects core-level electrons (photoelectrons) from the atoms in the sample. Only photoelectrons in the near-surface region (~1 to 10 nm) have enough kinetic energy to escape the sample [36]. The kinetic energy of the photoelectrons, which is measured by an electron energy analyzer, is related to the binding energy of the core-level electrons according to:

$$E_k = E_{h\nu} - E_b - \phi ,$$

where E_k is the kinetic energy of the photoelectron, $E_{h\nu}$ is the energy of the incident x-ray beam, E_b is the binding energy of the electron, and ϕ is the work function of the spectrometer. The binding energy of the core-level electrons is characteristic of the atom from which the photoelectron was generated. Therefore, XPS is a technique for characterizing the chemical composition in the near surface region of solid samples.

XPS measurements were performed on a PHI 5600ci instrument. The XPS instrument employed monochromatic aluminum K_α x-rays and the pass energy of the analyzer was 58.7 eV. Elemental surface concentrations were calculated from Cu $2p_{3/2}$, Pd $3d_{5/2}$, and S $2p_{3/2}$ peak areas and calibrated sensitivity factors. Depth profiles of elemental composition were acquired using

Ar^+ as the sputtering gas and XPS analysis of surface composition. The differentially-pumped ion gun was operated at 1.5 x 10^{-2} Pa and 25 mA, producing a sputtering rate of approximately10 nm/min based on the calibration of the sputter rate of a 10 nm Pt film.

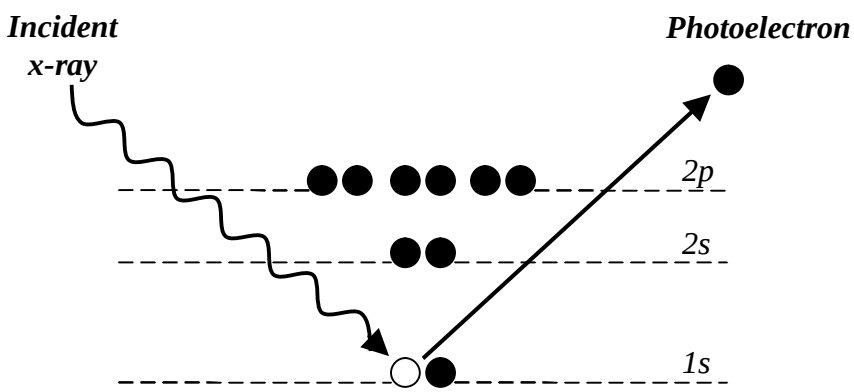

Figure 2.4 Schematic of the x-ray photoemission process. An incident x-ray beam ejects a core level electron (photoelectron) from an atom near the surface of the solid sample. The kinetic energy of the photoelectron is related to the binding energy of the electron, which is characteristic of the atom from which the photoelectron originated. The mean free path of photoelectrons is ~1 to 10 nm, making XPS a surface-sensitive technique for characterizing the chemical composition in the near surface region of solid samples.

2.3.3 Scanning electron microscopy and energy dispersive spectroscopy

Scanning electron microscopy (SEM) and energy dispersive spectroscopy (EDS) were used to determine the thickness of sulfide films grown on the surface of Pd and $Pd_{47}Cu_{53}$ foils from exposure to H_2S. The basis of SEM/EDS is that a high energy (20 keV) electron beam is swept in a raster across the surface of a sample producing backscattered electrons, secondary electrons, Auger electrons

and x-rays that can be analyzed to provide topographical and elemental information about the sample. EDS analysis of the x-rays ejected from the sample provides the elemental information that was used to measure the thickness of sulfide films from cross-sections of the foil membranes that were exposed to H_2S.

A schematic of the x-ray emission process in EDS analysis is shown in Figure 2.5. The interaction of the incident electron beam with core-level electrons in the atoms of the sample can excite the core-level electrons to produce secondary electrons and holes in the core-level orbital from which the secondary electrons originated from. Relaxation of higher-level electrons into the core-level holes is accompanied by two possible processes: Auger electron emission or x-ray emission. The energy of the Auger electrons and of the x-rays is equal to the difference in the energy level of the higher-level and core-level electron and is characteristic of the atom from which the process occurred. By mapping the sulfur x-rays over a two-dimensional area of a cross-section of Pd and $Pd_{47}Cu_{53}$ foils by EDS, the thickness of the sulfide film produced during exposure to H_2S was determined.

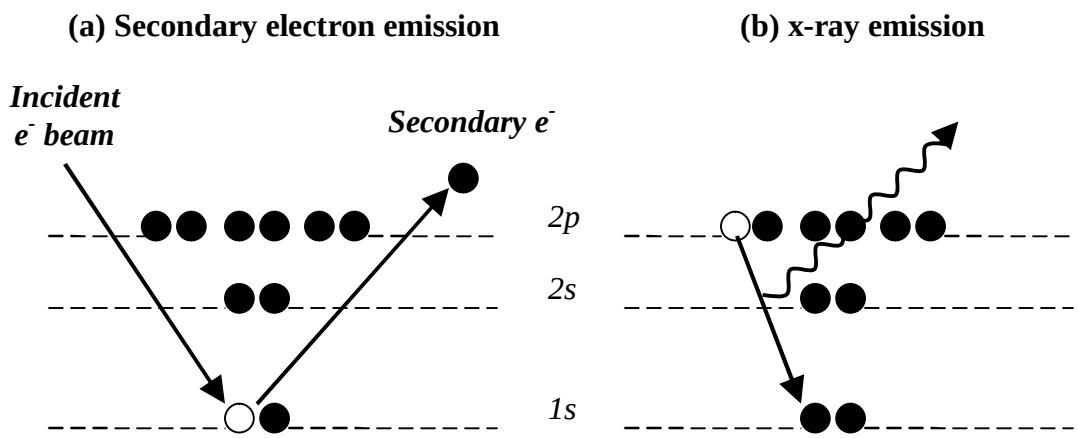

Figure 2.5 Schematic of the x-ray emission process for energy dispersive spectroscopic analysis. (a) An incident electron beam ejects a secondary electron from the sample and creates a hole in the core level (open circle). (b) The core level hole is filled by a higher level electron which is accompanied by x-ray emission from the sample. The energy of the x-ray is characteristic of the atom from which the x-ray was emitted and, therefore, spectroscopic analysis of the x-rays emitted from the sample gives elemental information about the sample.

2.4 Conclusions

A combination of experimental and analytical techniques was used in this thesis to investigate the effect of H_2S on hydrogen transport (H_2 dissociation and H atom permeation) across Pd and $Pd_{47}Cu_{53}$ membranes. Hydrogen permeation through Pd and $Pd_{47}Cu_{53}$ foil membranes was measured both in the absence of H_2S and in the presence of H_2S with a membrane testing apparatus. The effect of H_2S on the rate of H_2 dissociation on Pd, $Pd_{70}Cu_{30}$, and $Pd_{47}Cu_{53}$ was investigated with a H_2-D_2 exchange experiment that was developed in this thesis. Compositional analysis by x-ray diffraction, scanning electron microscopy, and x-

ray photoelectron spectroscopy was done to characterize the effect of H_2S on the bulk and surface compositions of Pd and $Pd_{47}Cu_{53}$ foil membranes.

Chapter 3

The Effect of H_2S on Hydrogen Permeation through Pd and $Pd_{47}Cu_{53}$

3.1 Summary

In this chapter, the effect of H_2S on hydrogen permeation through Pd and $Pd_{47}Cu_{53}$ foils is contrasted. In pure H_2 gas, hydrogen fluxes through pure Pd and $Pd_{47}Cu_{53}$ foils in the 623 K to 723 K temperature range are similar. In the presence of 1000 ppm H_2S in H_2, the hydrogen fluxes through both foils are substantially reduced, but with significantly different decay patterns. Six hours after the start of H_2S exposure, the Pd foil remained permeable to hydrogen, with the flux decreasing slowly over time. Our results show that H_2S slows hydrogen permeation through Pd indirectly by producing a relatively thick (~μm) Pd_4S film on the Pd surface that is about an order-of-magnitude less permeable to hydrogen than pure Pd. H_2S also inhibits hydrogen transport through Pd directly, possibly by blocking H_2 dissociation sites at the Pd_4S surface. In contrast to Pd, the hydrogen flux through the $Pd_{47}Cu_{53}$ foil is undetectable within five minutes of the start of H_2S exposure. XPS depth profiling of the $Pd_{47}Cu_{53}$ foil reveals that sulfur penetrates only ~3 nm into the $Pd_{47}Cu_{53}$ surface. Rapid formation of a Pd-Cu-S terminal layer, which is either inactive for hydrogen dissociation or impermeable to hydrogen atoms, is responsible for the deactivation of the $Pd_{47}Cu_{53}$ alloy membrane in H_2S at 623 K. At higher temperatures, the effect of H_2S on hydrogen permeation through $Pd_{47}Cu_{53}$ diminishes and the alloy is completely sulfur tolerant at temperatures greater than ~900 K.

3.2 Introduction

Coal can be used to produce affordable supplies of H_2 for use as a clean fuel or as a chemical commodity. Such supplies of H_2 must be separated from a coal derived gas stream composed primarily of H_2 and CO_2, with several other constituents such as steam, CO, and H_2S, at temperatures in the ~500 to ~700 K range. Dense metal membranes, which catalyze H_2 dissociation and allow only atomic H to permeate their bulk, are promising candidates for H_2/CO_2 separation due in part to their potential to produce high purity hydrogen and a high pressure CO_2-rich stream that is amenable to sequestration. However, coal gasification also produces H_2S, a highly corrosive gas that can react with Pd to form Pd_4S [9, 25, 29, 37] via the reaction:

$$4Pd + H_2S \leftrightarrow Pd_4S + H_2.$$

The H_2 flux across Pd membranes decreases rapidly during H_2S exposure [9, 25]. Morreale *et al*. [25] correlated the decay in H_2 flux during H_2S exposure to the Pd_4S growth kinetics measured under similar conditions. In doing so, they suggested that the decay in H_2 flux was due to the growth of a Pd_4S film on the Pd surface which has a H_2 permeability more than an order-of-magnitude lower than that of Pd.

To impart resistance to corrosion by H_2S, Pd has been alloyed with other metals [9, 21, 38-40]. Hydrogen transport through Pd-Cu alloys has received significant attention from both experimental and computational researchers [7, 9, 10, 19, 21, 22, 32-34, 38-52]. The $Pd_{47}Cu_{53}$ (mol%) alloy has the highest hydrogen permeability at 623 K among the Pd-Cu alloys [33, 43, 45, 46], and is

comparable in its hydrogen permeability to pure Pd at the same temperature. At higher temperatures (~900 K), hydrogen transport through $Pd_{47}Cu_{53}$ is not significantly inhibited by 1000 ppm H_2S [29]. At 623 K, however, hydrogen transport through $Pd_{47}Cu_{53}$ is severely inhibited by H_2S [7, 9, 19, 38].

In this chapter, we contrast the responses of Pd and $Pd_{47}Cu_{53}$ membranes to exposure to 1000 ppm H_2S in H_2 at 623 K. We analyze the compositions of the S-contaminated membranes by x-ray diffraction and x-ray photoelectron spectroscopy depth profiles to provide a framework for understanding the differences in their H_2S-induced performance degradation. This work shows that H_2S slows hydrogen transport through Pd by forming a relatively thick (~µm) Pd_4S layer that retains some ability to dissociate and transport hydrogen, although its H atom permeability is about an order-of-magnitude lower than that of Pd. The $Pd_{47}Cu_{53}$ alloy, on the other hand, forms a very thin (~nm) Pd-Cu-S layer that is completely impermeable to hydrogen at 623 K. At temperatures above ~900 K, however, H_2S has no effect on the rate of hydrogen permeation through $Pd_{47}Cu_{53}$.

3.3 Experimental

Hydrogen transport measurements were performed using foil membranes of pure Pd and $Pd_{47}Cu_{53}$. Circular membrane foils were cut from 25 µm thick Pd (Alfa Aesar, 99.9% metals purity) and 25 µm thick $Pd_{47}Cu_{53}$ (ATI Wah Chang, 99.0% metals purity) foils. The membranes were washed with acetone and mounted into a Swagelok® VCR tube assembly. The effective membrane surface

area was about 1.8 cm^2. Membranes were leak-tested by pressurizing the retentate (upstream) side of the membranes with 300 kPa of Ar and observing the pressure for 20 minutes. A leak-proof membrane was indicated by less than 1 kPa pressure drop on the upstream side.

Prior to making hydrogen permeation measurements, the membranes were heated to 623 K in He (retentate, upstream) and Ar (permeate, downstream). Then the retentate side of each membrane was exposed to a flowing mixture of 90% H_2/10% He (Butler Gas Products, Inc.) at 310 kPa, with the permeated H_2 collected at ambient pressure (~100 kPa). The temperature was measured using Omega type-K thermocouples positioned ~5 mm from the surface of each side of the membrane; the operating temperature was given by the average of the two temperatures. The H_2 flux through the membrane was measured using a bubble flowmeter (Alltech Digital Flowmeter Model 4074). A 1000 ppm H_2S/10% He/balance H_2 mixture (Butler Gas Products, Inc.) was introduced to the membrane surface following exposure to the 90% H_2/10% He mixture. The permeate gas composition was periodically analyzed by a gas chromatograph (Agilent Technologies Model 6890N) for its He content in order to confirm the absence of pinholes in the membrane. No He was detected in the permeate stream during the entire duration of the membrane tests, before and during H_2S exposure.

Pd_4S films were produced on the surface of Pd foils by exposure to a gas mixture with a composition of 1000 ppm H_2S / 10% He / H_2 (Butler Gas Products, Inc.) at a total pressure of 269 kPa and a temperature of 623 K. The H_2S exposure time varied from ~5 minutes for the thin (1 μm) Pd_4S films to ~24 hours for the

thicker (>15 μm) Pd_4S films. The bi-layered Pd_4S/Pd membranes were then exposed to either pure H_2 (99.99%, Butler Gas Products, Inc.) or the 1000 ppm H_2S in H_2 gas mixture while H_2 permeate flow rates were measured with a bubble flowmeter (Alltech Digital Flowmeter Model 4074) at ambient pressure. H_2 fluxes did not change over the course of the measurements (~30 minutes) and, therefore, the Pd_4S thicknesses were assumed to be constant. Following data collection, the membranes were cooled to room temperature in He and Ar and then dismounted for characterization.

X-ray diffraction (XRD) measurements of the foil surfaces were obtained using a PANalytical X'Pert Pro MPD powder diffractometer having a theta-theta configuration, a Cu x-ray source operated at 45 kV and 40 mA and an X'Celerator detector equipped with a monochromator. Patterns were recorded over a 2θ range of 30 to 90° at a step size of 0.02°. Foil samples were mounted on zero background quartz slides for analysis. Sample foils were not perfectly flat resulting in a slight peak shape distortion; however this distortion did not affect data interpretation.

Scanning electron microscope (SEM) analyses of cross-sections of the foils were performed to determine the nature of the films grown on their surface during exposure to H_2S. Cross-sectioned pieces of the Pd and $Pd_{47}Cu_{53}$ foils were set in epoxy and then polished with Carbimet Paper (Buehler) up to 1200 grit. The polished cross-sections were then analyzed with an Aspex Personal SEM 2000 which was operated with a 20 keV electron beam. Sulfur x-ray maps

of the cross-sections were used to quantify the thickness of the surface sulfide formed on the membrane foils.

X-ray photoelectron spectroscopy (XPS) measurements were used to determine the surface compositions of the foils and for depth profiling of the composition in the near surface region. XPS measurements were performed on a PHI 5600ci instrument. The XPS instrument employed monochromatic aluminum K_α x-rays and the pass energy of the analyzer was 58.7 eV. Elemental surface concentrations were calculated from Cu $2p_{3/2}$, Pd $3d_{5/2}$, and S $2p_{3/2}$ peak areas and calibrated sensitivity factors. Depth profiles of elemental composition were acquired using Ar^+ as the sputtering gas and XPS analysis of surface composition. The differentially-pumped ion gun was operated at 1.5 x 10^{-2} Pa and 25 mA, producing a sputtering rate of approximately 10 nm/min based on the calibration of the sputter rate of a 10 nm Pt film.

3.4 Model for extraction of permeabilities

Fick's first law of diffusion governs H atom transport through dense Pd and PdCu membranes at steady state:

$$J_{\mathrm{H}} = \frac{D \cdot \Delta c_{\mathrm{H}}}{x} \qquad (1)$$

where J_{H} is the steady-state H atom flux, D is the diffusivity of H atoms in the metal, Δc_{H} is the difference in the H atom concentration across the metal, and x is the thickness of the membrane. If the gas-phase H_2 on the high pressure side of

the membrane is in equilibrium with the H atoms dissolved near the high pressure surface of the membrane, and the gas-phase H_2 on the low pressure side of the membrane is in equilibrium with the H atoms dissolved near the low pressure surface of the membrane, then Sievert's law relates the difference in the H atom concentration across the membrane, Δc_H, to the difference in the square root of the H_2 partial pressure across the membrane, $\Delta P_{H2}^{1/2}$:

$$\Delta c_H = S \cdot \Delta P_{H2}^{1/2} \tag{2}$$

where S is the solubility of H atoms in the metal. Substitution of Sievert's Law, equation (2), into Fick's first law of diffusion, equation (1), gives:

$$J_H = \frac{DS \cdot \Delta P_{H2}^{1/2}}{x}. \tag{3}$$

Defining the H atom permeability (2 H atom basis) of the metal membrane, k, as:

$$k = \frac{DS}{2}, \tag{4}$$

and substituting equation (4) into equation (3) gives the steady-state H_2 flux across a metal membrane, J_{H2}:

$$J_{H2} = \frac{k \cdot \Delta P_{H2}^{1/2}}{x}. \tag{5}$$

H_2 transport across composite membranes has been well described in other publications [25, 53-56], and the H_2 flux across a bi-layered Pd_4S/Pd foil can be modeled by equation (6) if H-atom diffusion is rate-limiting [25]:

$$J_{H2} = \frac{\Delta P_{H2}^{1/2}}{\frac{x_{Pd4S}}{k_{Pd4S}} + \frac{x_{Pd}}{k_{Pd}}} \tag{6}$$

where k_{Pd4S} is the H atom permeability (2 H atom basis) of Pd_4S, k_{Pd} is the H atom permeability (2 H atom basis) of Pd, x_{Pd4S} is the thickness of the Pd_4S film, and x_{Pd} is the thickness of Pd substrate. If H atom diffusion through a bi-layered Pd_4S/Pd foil is rate-limiting, then the H_2 flux should be directly proportional to $\Delta P_{H2}^{1/2}$ with a slope that can be used to calculate the permeability of Pd_4S if the permeability of Pd is known and the Pd_4S and Pd thicknesses are known.

3.5 Results and Discussion

3.5.1 The hydrogen permeability of Pd and $Pd_{47}Cu_{53}$

H_2 fluxes across Pd and $Pd_{47}Cu_{53}$ foil were measured in pure H_2 to determine the H atom permeability of Pd and $Pd_{47}Cu_{53}$. Figure 3.1 shows the H_2 fluxes across (a) 25 μm thick Pd foil and (b) 25 μm thick $Pd_{47}Cu_{53}$ foil during exposure to pure H_2 in the 623 to 973 K (1023 K for $Pd_{47}Cu_{53}$) temperature range. As expected, H_2 fluxes across the Pd foil increased with increasing pressure and temperature. H_2 fluxes across the $Pd_{47}Cu_{53}$ foil also increase with increasing pressure; however, the H_2 flux changes non-monotonically with increasing temperature. H_2 fluxes across the $Pd_{47}Cu_{53}$ foil increase from 623 to 723 K, then decrease from 723 to 873 K, and then increase again from 873 K to 1023 K. This non-monotonic change in the H_2 flux with temperature is due to a change in the $Pd_{47}Cu_{53}$ crystal structure from body-centered-cubic (BCC) at temperatures below ~723 K to face-centered-cubic (FCC) at temperatures above ~873 K [7, 9, 10]. In the temperature range ~723 to ~873 K, the BCC and FCC crystal phases of the $Pd_{47}Cu_{53}$ co-exist in a mixed phase structure [7, 9, 10].

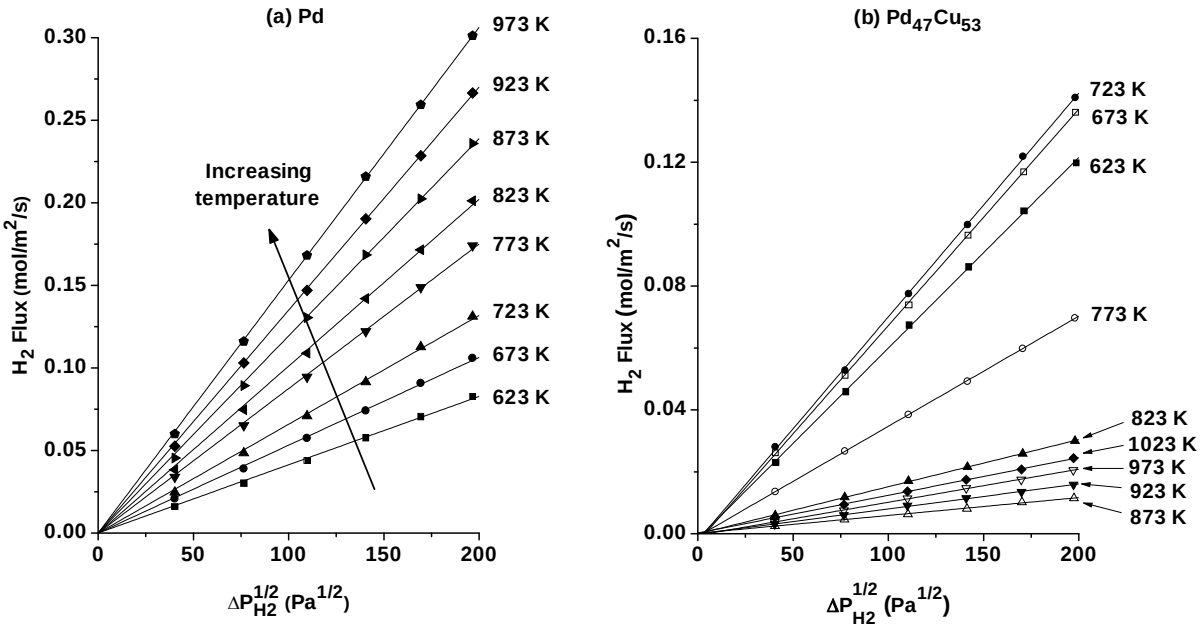

Figure 3.1. H_2 fluxes across 25 µm thick (a) Pd and (b) $Pd_{47}Cu_{53}$ foil versus Sievert's partial pressure driving force, $\Delta P_{H2}^{1/2}$, in the 623 to 973 K (1023 K for $Pd_{47}Cu_{53}$) temperature range during exposure to pure H_2. H_2 fluxes across the Pd foil increase with increasing pressure and temperature. H_2 fluxes across the $Pd_{47}Cu_{53}$ foil increase with increasing pressure, but change non-monotonically with temperature. In the 623 to 723 K temperature range, H_2 fluxes across the $Pd_{47}Cu_{53}$ foil increase with increasing temperature, then H_2 fluxes decrease with increasing temperature from 723 to 873 K, and then H_2 fluxes increase with increasing temperature from 873 to 1023 K. This non-monotonic change in H_2 flux is due to a change in the $Pd_{47}Cu_{53}$ crystal from body-centered-cubic at temperatures less than ~723 K to face-centered-cubic at temperatures greater than ~873 K [7,9,10]. The body-centered-cubic crystal structure of the $Pd_{47}Cu_{53}$ alloy is much more permeable to H atoms than the face-centered-cubic crystal structure of the alloy.

The H_2 fluxes across Pd (Figure 3.1(a)) and $Pd_{47}Cu_{53}$ (Figure 3.1(b)) are directly proportional to the Sievert's partial pressure driving force, $\Delta P_{H2}^{1/2}$, indicating that H atom diffusion through the bulk of the foils is rate limiting. Using equation (5) and the slopes of the fitted solid lines in Figure 3.1(a) and 3.1(b), the H atom permeability of Pd (k_{Pd}) and $Pd_{47}Cu_{53}$ (k_{Pd47Cu53}) were calculated at each temperature. The H atom permeability (2 H atom basis) of Pd was fit to an Arrhenius expression:

$$k_{\mathrm{Pd}} = 10^{-6.33\pm0.03} exp\left(\frac{(-0.199 \pm 0.004)\mathrm{eV}}{k_{\mathrm{B}}\mathrm{T}}\right)\frac{\mathrm{molH_2}}{\mathrm{m \cdot s \cdot Pa^{1/2}}} \qquad (7)$$

where T (K) is the temperature and k_{B} is the Boltzmann constant. Figure 3.2(a) illustrates that our results for the H atom permeability of Pd are consistent with previous literature reports [8, 57, 58]. Figure 3.2(b) shows that our result for the H atom permeability of $Pd_{47}Cu_{53}$ are also consistent with previous literature reports [9, 31].

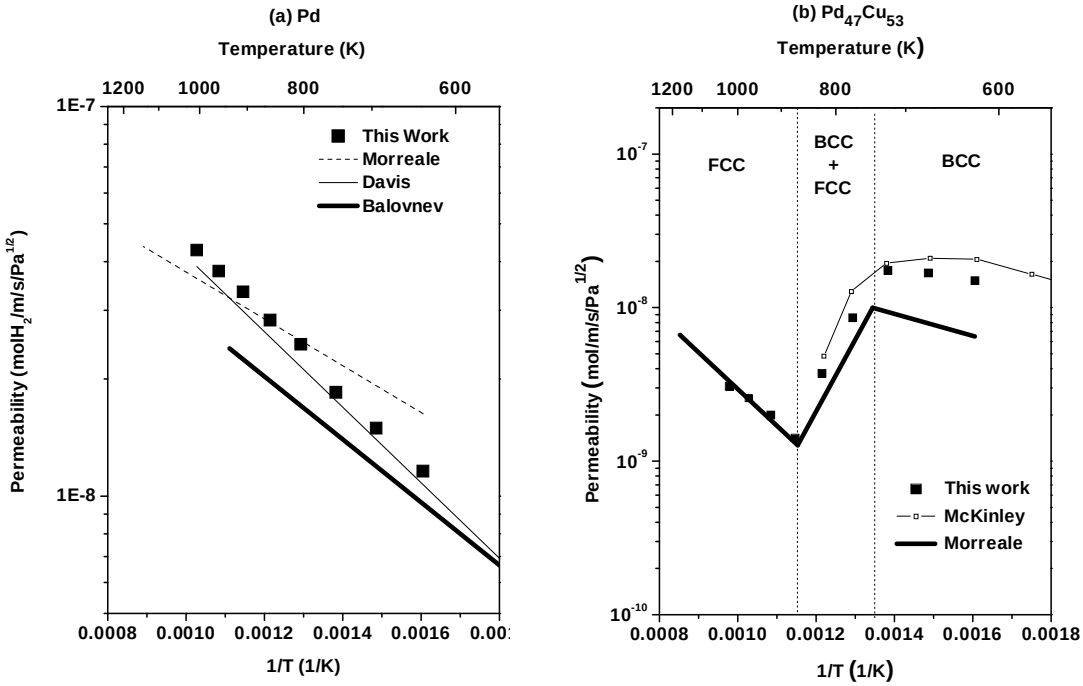

Figure 3.2 Arrhenius plots of the H atom permeability of (a) Pd and (b) $Pd_{47}Cu_{53}$ calculated with equation (5) and the H_2 fluxes in Figure 3.1(a) and 3.1(b), respectively. Our measurements for the H atom permeability of Pd are in good agreement with those of Morreale [8], Davis [57], and Balovnev [58]. Our measurements for the H atom permeability of $Pd_{47}Cu_{53}$ are in good agreement with those of McKinley [31] and Morreale [9]. The H atom permeability of the face-centered-cubic crystal structure of the $Pd_{47}Cu_{53}$ alloy is about an order-of-magnitude lower than that of the body-centered-cubic crystal structure of the alloy. Figure 3.2(a) is adapted from [2].

A comparison of the H atom permeability of Pd and $Pd_{47}Cu_{53}$ measured in this work, and the H atom permeability of Cu [59] and $Pd_{70}Cu_{30}$ [9] from literature, is shown in Figure 3.3. The H atom permeability of Cu is about three to five orders-of-magnitude lower than that of pure Pd in the 623 to 973 K temperature range. The H atom permeability of BCC $Pd_{47}Cu_{53}$ (~623 to 723 K) is similar to that of pure Pd but the permeability of FCC $Pd_{47}Cu_{53}$ (~873 to 1023 K)

is about an order-of-magnitude lower than that of Pd. The H atom permeability of $Pd_{70}Cu_{30}$, which has only a FCC crystal structure, is about one-fifth that of pure Pd.

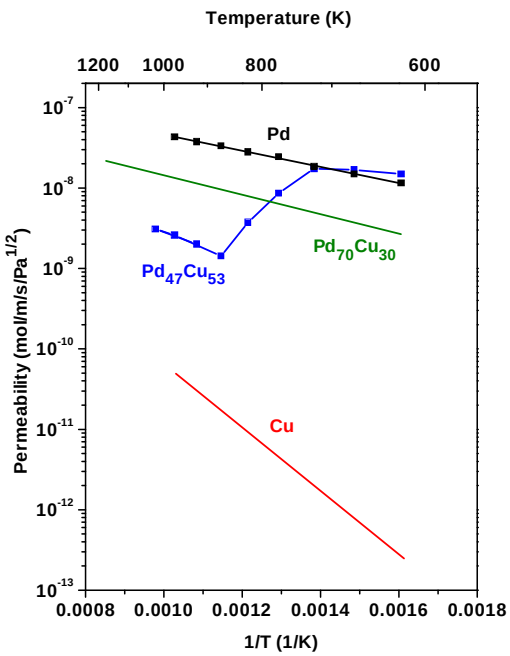

Figure 3.3 Comparison of the H atom permeability of Pd and $Pd_{47}Cu_{53}$ measured in this work, and the H atom permeability of Cu [59] and $Pd_{70}Cu_{30}$ [9] from literature. The H atom permeability of Cu is about three to five orders-of-magnitude lower than that of Pd. The H atom permeability of BCC $Pd_{47}Cu_{53}$ (~623 to 723 K) is similar to that of Pd, but the H atom permeability of FCC $Pd_{47}Cu_{53}$ (~873 to 1023 K) is about an order-of-magnitude lower than that of Pd. The H atom permeability of $Pd_{70}Cu_{30}$, which only has a FCC crystal structure, is about one-fifth that of Pd.

3.5.2 Inhibition of H_2 transport through Pd and $Pd_{47}Cu_{53}$ by H_2S at 623 K

In the previous section, it was shown that the H atom permeabilities of Pd and $Pd_{47}Cu_{53}$ are similar in the 623 to 723 K temperature range. In this section, the effect of H_2S on hydrogen permeation through Pd and $Pd_{47}Cu_{53}$ foils is contrasted. We analyze the sulfur-exposed Pd and $Pd_{47}Cu_{53}$ foils by x-ray diffraction, scanning electron microscopy, and x-ray photoelectron spectroscopy to provide a framework for understanding the mechanisms by which H_2S slows hydrogen transport.

The transient effect of H_2S on hydrogen permeation through Pd and $Pd_{47}Cu_{53}$ was investigated by measuring hydrogen fluxes through Pd and $Pd_{47}Cu_{53}$ foil membranes, first in the absence of H_2S to establish a baseline, and then in the presence of 1000 ppm H_2S. Results of the membrane test are presented in Figure 3.4. Baseline hydrogen fluxes through the two foils were ~0.1 mol/m^2/s for both Pd and $Pd_{47}Cu_{53}$. Assuming that Sievert's Law is obeyed, the calculated H atom permeabilities (2 H atom basis) from the baseline H_2 fluxes were ~1.3x10^{-8} mol/m/s/Pa$^{1/2}$ for $Pd_{47}Cu_{53}$ and ~1.2x10^{-8} mol/m/s/Pa$^{1/2}$ for Pd; both are in good agreement with our permeabilities measured in section 3.5.1 (see Figure 3.3). Both membranes displayed significant decreases in hydrogen flux upon exposure to 1000 ppm H_2S. The hydrogen flux through the $Pd_{47}Cu_{53}$ foil was below the detection limit of the bubble flowmeter (< ~4x10^{-4} mol/m^2/s) within five minutes of exposure to H_2S. In contrast, after an initially rapid decline, the hydrogen flux decay through the Pd foil slowed significantly. After

six hours of H_2S exposure, the hydrogen flux through the Pd membrane was still 10% of its baseline value.

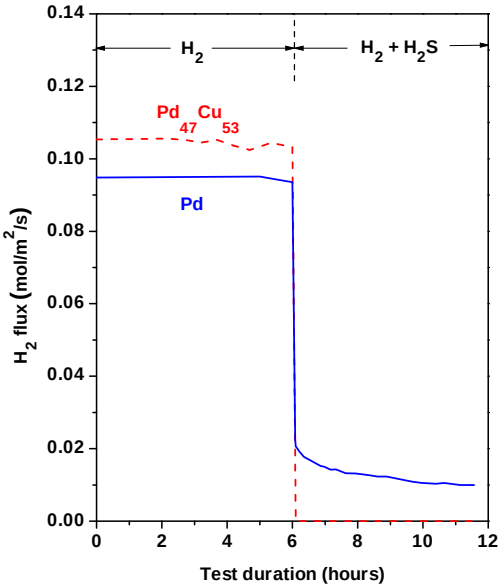

Figure 3.4 Hydrogen flux through 25 µm Pd (blue solid line) and $Pd_{47}Cu_{53}$ (red dashed line) membranes versus test duration at 623 K, total feed gas pressure of 310 kPa and total permeate pressure of ~100 kPa (ambient pressure). A 90% H_2/10% He mixture was exposed to the membrane surface during the first portion of the test and then 1000 ppm H_2S/10% He/balance H_2 was fed to the membrane surface at 6 hours. The Pd membrane was still permeable to H_2 after 6 hours of exposure to 1000 ppm H_2S whereas, the $Pd_{47}Cu_{53}$ membrane was impermeable to H_2 after less than 5 minutes of exposure to H_2S. Figure 3.4 is adapted from [1] with permission.

To determine whether any thick metal-sulfide compounds (corrosion layers) formed as a result of H_2S exposure, the Pd and $Pd_{47}Cu_{53}$ foils were analyzed by x-ray diffraction (XRD) following membrane testing. Figures 3.5(a) and 3.5(b) display the XRD patterns for the Pd and $Pd_{47}Cu_{53}$ foils, respectively,

including diffraction patterns of the clean Pd and $Pd_{47}Cu_{53}$ foils for reference. As expected, the diffraction pattern of the clean Pd foil exhibits features that are assignable to the face-centered-cubic Pd structure. The XRD pattern of the Pd foil that was exposed to H_2S is dominated by features that can be assigned to crystalline palladium sulfide (Pd_4S), with only very small peaks from metallic Pd. These results illustrate that H_2S exposure causes the Pd membrane to form a specific palladium sulfide reaction product, Pd_4S. In contrast to the XRD results from the Pd foil, the XRD patterns of the clean $Pd_{47}Cu_{53}$ foil and the $Pd_{47}Cu_{53}$ foil after 6 hours of H_2S exposure (Figure 3.5(b)) are nearly identical and are both assignable to the body-centered-cubic structure of $Pd_{47}Cu_{53}$. The diffraction peak intensities of the clean and H_2S-exposed $Pd_{47}Cu_{53}$ foils are not identical and vary from the intensities expected for an ideal body-centered-cubic $Pd_{47}Cu_{53}$ powdered sample. The peak intensities observed for the clean Pd foil also vary from the intensities expected for an ideal face-centered-cubic Pd powdered sample. These variations are probably due to the fact that non-ideal solid metal foil samples were analyzed. The discrepancies in peak intensity probably reflect a preferred orientation of the metal crystallites comprising the membrane foils.

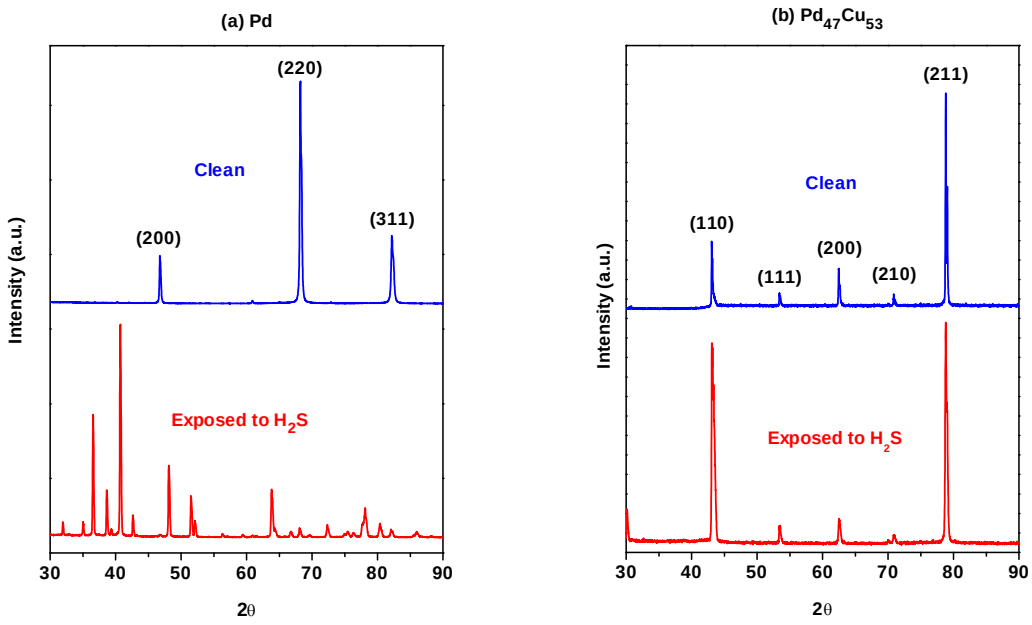

Figure 3.5 X-ray diffraction patterns of (a) 25 µm Pd foil before (Clean) and after exposure to 1000 ppm H_2S for 6 hours (Exposed to H_2S) and (b) 25 µm $Pd_{47}Cu_{53}$ foil before (Clean) and after exposure to 1000 ppm H_2S for 6 hours (Exposed to H_2S). The peaks in the diffraction pattern of the clean Pd foil are assignable to the face-centered-cubic crystal structure. The peaks in the diffraction pattern of the Pd foil exposed to H_2S are associated with a palladium sulfide compound, Pd_4S. The diffraction patterns of the clean $Pd_{47}Cu_{53}$ foil and the $Pd_{47}Cu_{53}$ foil exposed to H_2S are nearly identical and are associated with the body-centered cubic crystal structure of the alloy. Figure 3.5 is adapted from [1] with permission.

Cross-sections of the Pd and $Pd_{47}Cu_{53}$ foils were imaged by SEM to determine the thickness of sulfur corrosion layers on the surface of the foils. The sulfur concentration was mapped over the SEM images by EDS. SEM analysis of the Pd and $Pd_{47}Cu_{53}$ foils after H_2S exposure are presented in Figures 3.6(a) and 3.6(b), respectively; EDS mapping of sulfur concentration in the SEM images of the Pd and $Pd_{47}Cu_{53}$ foils are presented in Figures 3.6(c) and 3.6(d), respectively.

A noticeable difference in the roughness of the Pd and $Pd_{47}Cu_{53}$ foil surfaces exposed to H_2S is evident from the SEM images in Figure 3.6; the surface of the Pd foil (Figure 3.6(a)) is significantly rougher than that of the $Pd_{47}Cu_{53}$ foil (Figure 3.6(b)). Sulfidation of the Pd foil surface to Pd_4S is probably responsible for the fact that the Pd foil surface is rougher than that of the $Pd_{47}Cu_{53}$ foil, which did not form any sulfur compounds that could be detected by XRD. EDS reveals a sulfur-rich layer on the surface of the Pd foil (Figure 3.6(c)), which XRD identified as a Pd_4S film, that is ~6.6 ± 0.9 μm thick (average of 75 different thickness measurements across the entire length of the Pd foil cross-section). In contrast to the sulfur film observed on the Pd foil, EDS (Figure 3.6(d)) did not detect a significant amount of sulfur on the $Pd_{47}Cu_{53}$ foil after H_2S exposure. EDS analyzes x-rays from a relatively large volume within the sample, however, and thus, it is not able to detect sulfur contamination in a very thin layer near the surface of the $Pd_{47}Cu_{53}$ membrane.

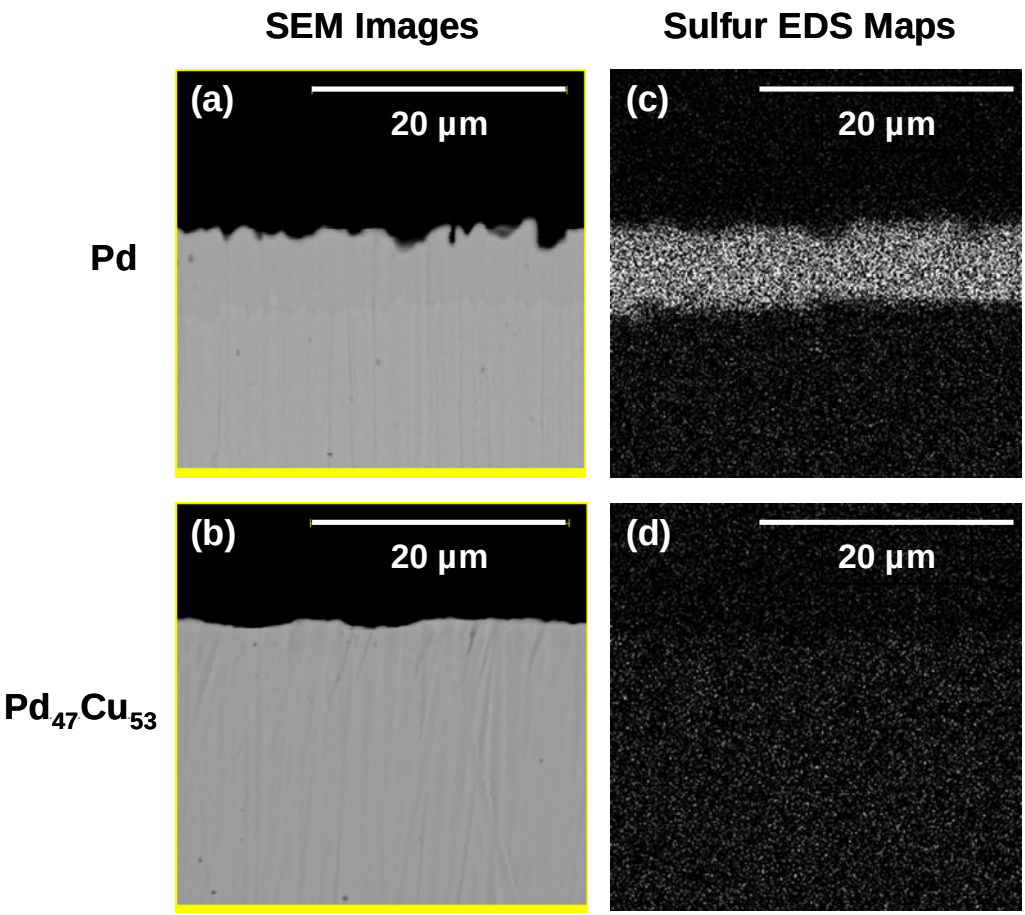

Figure 3.6 Scanning electron micrographs of cross-sections of the (a) Pd and (b) $Pd_{47}Cu_{53}$ foils that were exposed to H_2S for 6 hours. Sulfur x-ray mapping in the SEM images of the (c) Pd and (d) $Pd_{47}Cu_{53}$ cross-sections highlight the S-rich regions in white. After 6 hours of H_2S exposure, the thickness of the Pd_4S film produced on the surface of the Pd foil ((a) and (c)) was ~6.6 µm thick. In contrast to Pd, there was no sulfur detected in the cross-section of the $Pd_{47}Cu_{53}$ foil by SEM/EDS. Figure 3.6 is adapted with permission from [1].

XPS depth profiles of the Pd and $Pd_{47}Cu_{53}$ foils were collected to detect sulfur contamination near the membrane surfaces that may be undetectable by XRD and EDS analysis. XPS composition depth profiles of the Pd and $Pd_{47}Cu_{53}$ foils after six hours of H_2S exposure are presented in Figures 3.7(a) and 3.7(b), respectively. The Pd foil (Figure 3.7(a)) has a stoichiometry in the near-surface

region (~200 nm) that is approximately constant at Pd:S ≈ 4:1, which is consistent with the presence of Pd_4S as indicated by the XRD results. In contrast, S appears only very near the top-surface of the $Pd_{47}Cu_{53}$ alloy membrane (Figure 3.7(b)); its signal decayed to zero after Ar^+ sputtering only ~3 nm into the bulk of the $Pd_{47}Cu_{53}$ membrane.

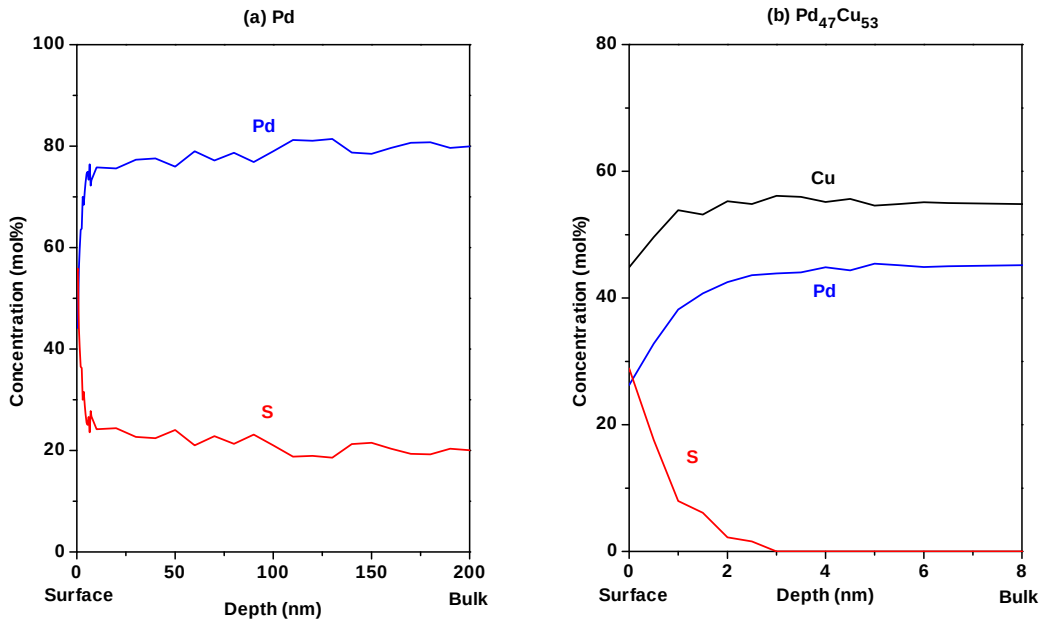

Figure 3.7 X-ray photoelectron spectroscopy depth profiles of the (a) 25 µm Pd and (b) 25 µm $Pd_{47}Cu_{53}$ membranes exposed to 1000 ppm H_2S for 6 hours. Elemental concentrations are shown for Pd, S, and Cu. The sputtering rate is ~10 nm/min as measured using a pure Pt film. The Pd:S ratio in the near-surface region (~200 nm) of the Pd foil is roughly constant at 4:1, which is consistent with Pd_4S stoichiometry. Sulfur was detected only a few nm into the bulk of the $Pd_{47}Cu_{53}$ foil exposed to H_2S. Figure 3.7 is adapted with permission from [1].

Pd and $Pd_{47}Cu_{53}$ membranes clearly respond differently to H_2S exposure at 623 K. We believe that the different responses of the hydrogen flux to H_2S exposure exhibited by the two membranes are related to the evolution of their

surface compositions during H_2S exposure. Furthermore, two different mechanisms may be responsible for the inhibition of hydrogen transport through the two membranes: poisoning of the catalytic dissociation of H_2 at the surface and reduced permeability of hydrogen through the bulk of the membrane.

The observation of non-zero flux through the Pd foil during H_2S exposure indicates that the membrane surface retained H_2 dissociation activity. The continuous slow decline of the hydrogen flux through the Pd membrane is indicative of an increasing resistance to hydrogen transport, which is consistent with hydrogen atom diffusion being retarded by a slowly thickening, dense, low-permeability Pd_4S corrosion layer on the surface. This mechanism has been suggested by Morreale, *et al.* who estimated the hydrogen permeability of Pd_4S at 623 K to be ~1/20th that of Pd by correlating Pd_4S growth kinetics to the decline in hydrogen flux through a Pd membrane during H_2S exposure [9, 25]. The steep initial decline in hydrogen flux through the Pd membrane immediately following H_2S exposure may be due to a rapid initial corrosion rate that slows as diffusion of Pd and/or S ions through the Pd_4S scale becomes slower. Another possible explanation for the rapid initial decline in hydrogen flux through the Pd membrane following H_2S exposure is that the catalytic activity of the Pd_4S surface may be significantly lower than that of Pd. As the thickness of the low-permeability Pd_4S film grows beyond a critical value, hydrogen atom diffusion through the bulk becomes rate limiting. A third explanation for the evolution of the hydrogen flux is that there may be a significant barrier to hydrogen atom

transport across the Pd_4S/Pd interface that dominates transport initially but becomes insignificant as the Pd_4S thickness grows beyond a critical value.

The immediate decline in hydrogen flux through the $Pd_{47}Cu_{53}$ membrane at the start of H_2S exposure must be related to the properties of its thin Pd-Cu-S terminal layer. Neither XRD nor XPS depth profiling could identify this thin Pd-Cu-S terminal layer as a specific compound and, therefore, the mechanism of its formation is not clear. Presumably this layer is either inactive for hydrogen dissociation or it displays near-zero hydrogen atom permeability.

3.5.3 The hydrogen permeability of Pd_4S

In the previous section, it was shown that exposure of Pd to H_2S resulted in the formation of a relatively thick (~µm) Pd_4S film on the surface of the Pd foil. In this section, the influence of Pd_4S film formation on slowing hydrogen transport through Pd is investigated in more detail. The effect of Pd_4S film thickness on the H_2 flux across Pd_4S/Pd foils was investigated by measuring H_2 fluxes across Pd_4S/Pd foils with various Pd_4S film thicknesses. Pd_4S films were produced by exposing the upstream surface of pure Pd foils to a 1000 ppm H_2S / 10% He / H_2 gas mixture at a total pressure of 269 kPa and a temperature of 623 K in the membrane testing apparatus. H_2 fluxes were measured using pure H_2 to prevent Pd_4S growth during measurements and to eliminate the effects of H_2S on H_2 transport; H_2 fluxes did not vary over the course of the measurements (~30 minutes) and, therefore, the Pd_4S thicknesses can be assumed to be constant throughout the experiment. Following membrane testing, the Pd_4S film thicknesses were measured by cross-sectional optical microscopy of the Pd_4S/Pd foils. Figure 3.8 shows the H_2 fluxes across Pd_4S/Pd foils with Pd_4S thicknesses of 0 (pure Pd), 1, 2, 6, and 14 µm at 623 K. Due to the low permeability of Pd_4S relative to Pd, the H_2 fluxes decrease as the Pd_4S thickness increases.

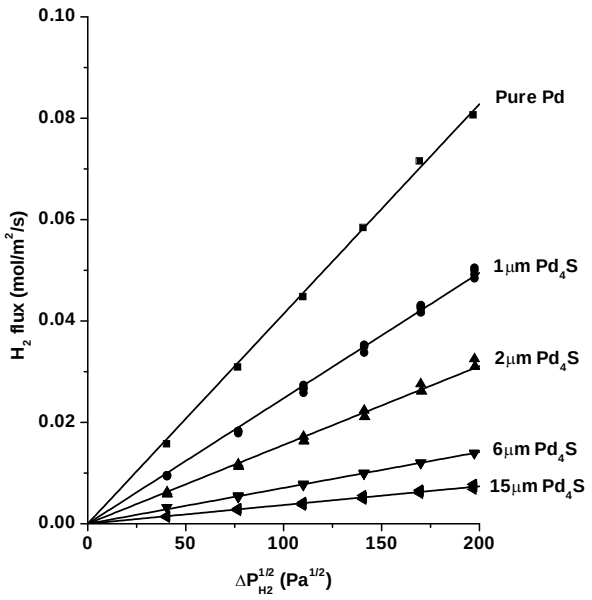

Figure 3.8 H_2 fluxes across bi-layered Pd_4S/Pd foils with Pd_4S thicknesses of 0 (pure Pd), 1, 2, 6, and 14 µm during exposure to pure H_2 at 623 K. Pd_4S films were produced on the surface of Pd by exposure to 1000 ppm H_2S / 10% He/ H_2 at 623 K and a total pressure of 269 kPa. H_2S exposure times varied from ~5 minutes for the 1 µm Pd_4S film to ~24 hours for the 14 µm Pd_4S film. The H_2 partial pressure in the feed gas was varied from 128 to 266 kPa while the permeated H_2 was collected at ambient (101 kPa) pressure. H_2 fluxes decrease as the Pd_4S thickness increases due to the low permeability of Pd_4S relative to Pd. Figure 3.8 is taken with permission from [2].

To determine whether H_2S inhibits H_2 transport across Pd_4S/Pd by factors in addition to the presence of the Pd_4S film, H_2 fluxes across Pd_4S/Pd foils were measured during exposure to a 1000 ppm H_2S / 10% He / H_2 gas mixture. Figure 5 shows the H_2 fluxes across a 14 µm Pd_4S/Pd foil during exposure to both pure H_2 and a 1000 ppm H_2S / 10% He / H_2 feed gas mixture at 623 K. In both pure H_2 and in the H_2S/H_2 gas mixture, H_2 fluxes did not change significantly over the course of the measurements (~30 minutes); therefore, the Pd_4S thickness can be assumed to be constant throughout the experiment. At all H_2 pressures, the H_2 fluxes across the 14 µm Pd_4S/Pd foil were significantly lower in the 1000 ppm H_2S in H_2 gas mixture than in pure H_2. H_2 fluxes across bi-layered Pd_4S/Pd foils were also measured at 673 K with a ~14 µm Pd_4S film, 723 K with a ~19 µm Pd_4S film, and 773 K with a ~22 µm Pd_4S film, both in pure H_2 and in the 1000 ppm H_2S / 10% He / H_2 feed gas mixture. At all temperatures and Pd_4S film thicknesses, the H_2 fluxes across the bi-layered Pd_4S/Pd foils were lower in the H_2S/H_2 gas mixture than in pure H_2. Given the relatively low H_2 fluxes, the low He concentration, and the low H_2S concentration, gas-phase hydrogen transport near the surface of the membranes (i.e. concentration polarization) is probably not the cause of the reduced H_2 flux in the 1000 ppm H_2S / 10% He / H_2 feed gas relative to that in the pure H_2 feed gas. Therefore, H_2S probably inhibits one or more molecular processes at the Pd_4S surface. H_2S may inhibit the H_2 dissociation reaction by blocking H_2 adsorption sites or by increasing the barrier to H_2 dissociation. The effect of H_2S on H_2 dissociative adsorption on Pd_4S will

be discussed in more detail in Chapter 5. Alternatively, H_2S may inhibit H-atom transport from the surface to the sub-surface of Pd_4S.

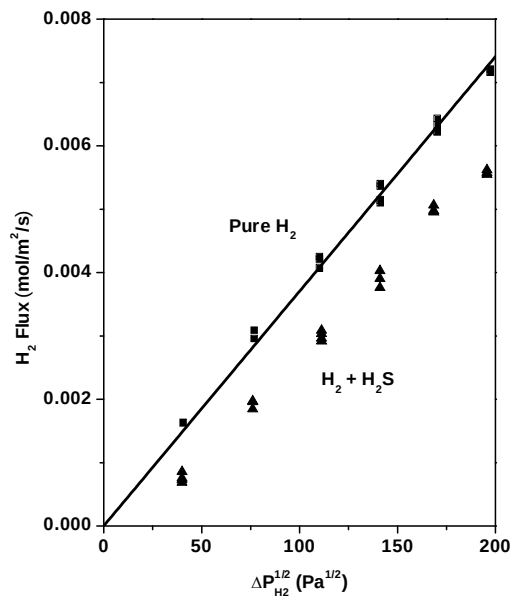

Figure 3.9 H_2 fluxes across a 14 µmPd_4S / Pd foil at 623 K during exposure to pure H_2 and a 1000 ppm H_2S / 10% He / H_2 gas mixture (H_2 + H_2S). The H_2 partial pressure in the feed gas was varied from 128 to 266 kPa while the permeated H_2 was collected at ambient (101 kPa) pressure. H_2 fluxes across the 14 µmPd_4S / Pd foil are significantly lower in the H_2 + H_2S gas mixture than in the pure H_2 feed gas which could be due to H_2S blocking of H_2 dissociation sites. Figure 3.9 is taken with permission from [2].

During exposure to pure H_2 at varying pressure in the 623 to 773 K temperature range, the H_2 fluxes are directly proportional to $\Delta P_{H2}^{1/2}$ and intersect the origin, which indicates that H atom diffusion through the bulk of the foil is rate-limiting and that the Pd_4S layer is essentially dense. Therefore, the H atom

permeability of Pd_4S can be calculated using equation (6). The temperature dependence of the H atom permeability (2 H atom basis) of Pd_4S (k_{Pd4S}) is given by an Arrhenius expression:

$$k_{\mathrm{Pd4S}} = 10^{-7.5\pm0.2} exp\left(\frac{(-0.22 \pm 0.03)\mathrm{eV}}{k_{\mathrm{B}}\mathrm{T}}\right)\frac{\mathrm{molH}_2}{\mathrm{m}\cdot\mathrm{s}\cdot\mathrm{Pa}^{1/2}} \qquad (8)$$

where T (K) is the temperature and k_B is the Boltzmann constant. Figure 3.10 is an Arrhenius plot that compares the H atom permeability (2 H atom basis) of Pd and Pd_4S measured in this work and the H atom permeability of Pd_4S determined by Morreale by correlation of Pd_4S growth kinetics to H_2 permeability decay in the presence of H_2S [25]. Except for the measurement made at 623 K, our results for the H atom permeability of Pd_4S are in very good agreement with the experimental results reported by Morreale; the H atom permeability of Pd_4S is about an order-of-magnitude lower than that of Pd. The small difference between our results and those of Morreale at 623 K may be due to the fact that the latter were determined from measurements made in the presence of H_2S. As described earlier, in addition to reacting with Pd to form Pd_4S, H_2S may also block H_2 dissociation sites on the Pd_4S surface. In this work, the H atom permeability of Pd_4S was determined from measurements of H_2 transport across bi-layered Pd_4S/Pd foils during exposure to pure H_2. For all of the bi-layered Pd_4S/Pd foils from which the H atom permeability of Pd_4S was measured, more than 90% of the total resistance to hydrogen transport was attributable to the Pd_4S film and, therefore, our method for calculating the H atom permeability of Pd_4S should be

reasonably accurate. The good agreement between our results and the results from Morreale [25] illustrates that the decay in H_2 flux through a Pd foil during H_2S exposure is mainly due to the growth of a low permeability Pd_4S film on the Pd surface.

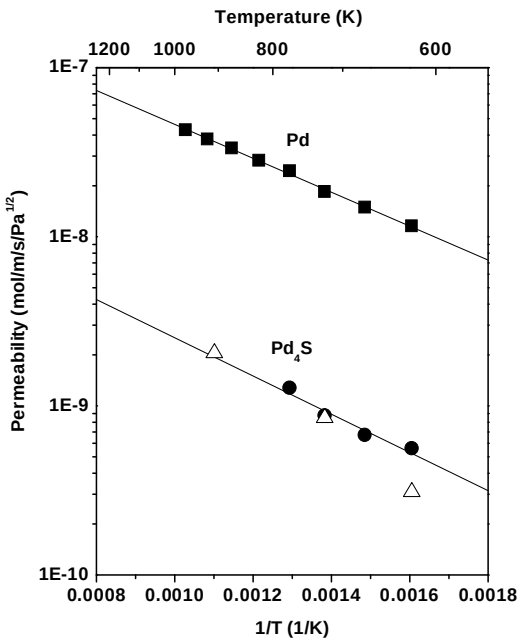

Figure 3.10 Comparison of the H atom permeability of Pd (closed squares) and the H atom permeability of Pd_4S measured in this work (closed circles) and in the work of Morreale (open triangles) [25]. The H atom permeability of Pd_4S was measured using bi-layered Pd_4S foils with Pd_4S thicknesses of ~14 µm at 623 K, ~14 µm at 673 K, ~19 µm at 723 K, and ~22 µm at 773 K. The solid fitted lines for the H atom permeability of Pd and Pd_4S are described by equations (7) and (8), respectively.

3.5.4 High temperature sulfur tolerance by $Pd_{47}Cu_{53}$

At 623 K, the $Pd_{47}Cu_{53}$ alloy is impermeable to H_2 in the presence of 1000 ppm H_2S (see Figure 3.4). A thin (~nm) Pd-Cu-S layer forms on the surface of the $Pd_{47}Cu_{53}$ alloy that blocks all hydrogen transport through the alloy. At higher temperatures, however, the influence of H_2S on hydrogen permeation through $Pd_{47}Cu_{53}$ becomes weaker. Figure 3.11 shows the H_2 fluxes through $Pd_{47}Cu_{53}$ versus Sievert's partial pressure driving force during exposure to pure H_2 and 1000 ppm H_2S at (a) 673 K, (b) 773 K, (c) 873 K, and (d) 973 K. H_2S completely blocks hydrogen transport through $Pd_{47}Cu_{53}$ at 673 K. At 773 K, the H_2 flux through $Pd_{47}Cu_{53}$ in the presence of H_2S is non-zero but is still much lower than the H_2 flux in pure H_2. At 873 K, the difference between the H_2 flux measured in pure H_2 and the H_2 flux measured in 1000 ppm H_2S becomes smaller. At 973 K, there is not a significant difference in the H_2 flux measured in pure H_2 and that measured in 1000 ppm H_2S. At 973 K, the H_2 fluxes vary linearly with the Sievert's partial pressure driving force and intersect the origin, indicating that H atom diffusion is rate-limiting. At 773 and 873 K, however, the H_2 fluxes do not intersect the origin. This indicates that Sievert's law is violated and H atom diffusion through the bulk of $Pd_{47}Cu_{53}$ is not rate-limiting at 773 and 873 K. It is possible that, in the presence of 1000 ppm H_2S at temperatures less than ~900 K, the surface H_2 dissociation reaction is not faster than the rate of H atom diffusion through the bulk of $Pd_{47}Cu_{53}$.

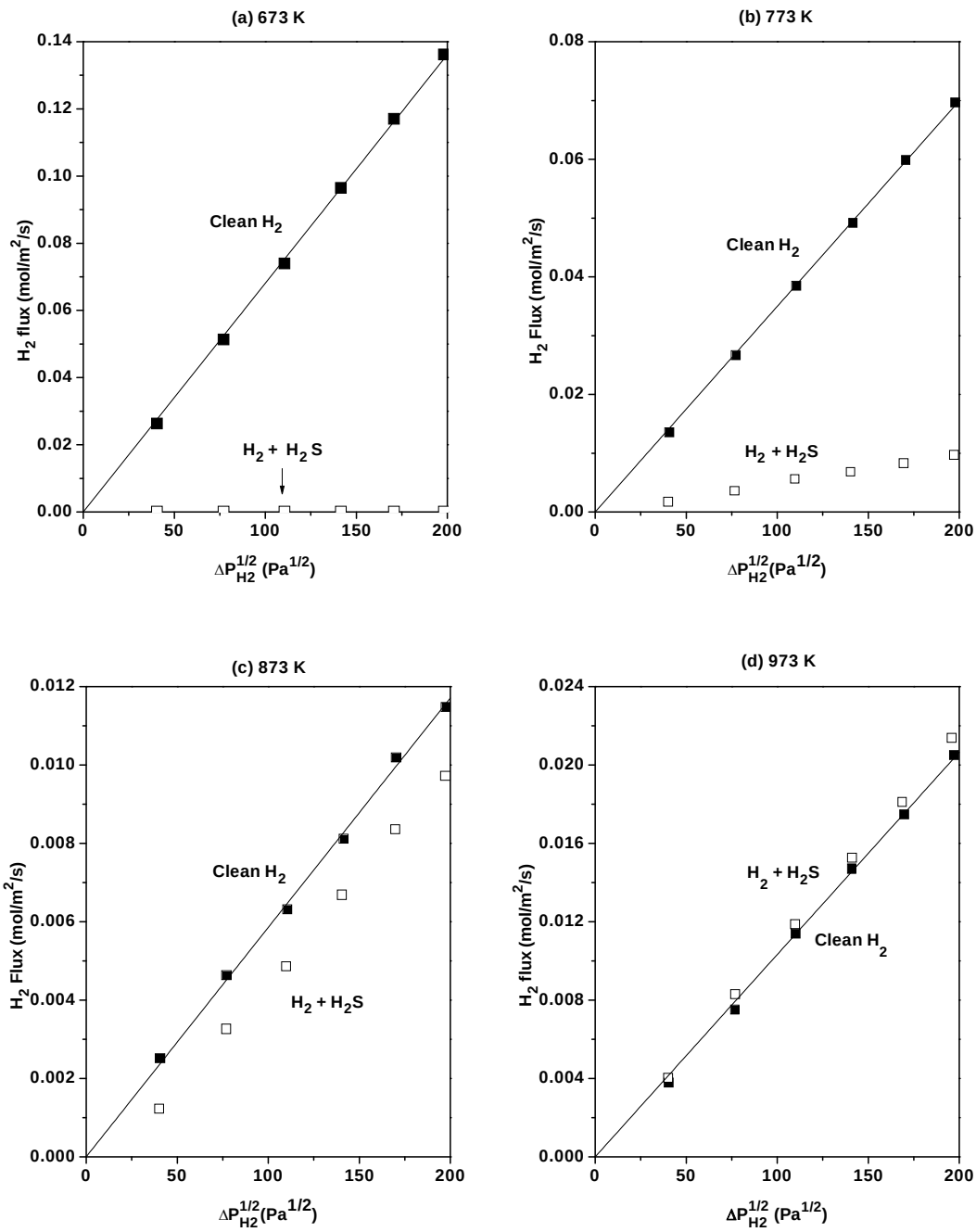

Figure 3.11 H_2 fluxes through $Pd_{47}Cu_{53}$ versus Sievert's partial pressure driving force during exposure to pure H_2 (clean H_2) and in the presence of 1000 ppm H_2S (H_2 + H_2S) at (a) 673 K, (b) 773 K, (c) 873 K, and (d) 973 K. The effect of H_2S on the H_2 flux through $Pd_{47}Cu_{53}$ diminishes with increasing temperature. At 973 K, hydrogen transport through $Pd_{47}Cu_{53}$ is not significantly affected by 1000 ppm H_2S.

If we arbitrarily define sulfur tolerance as the ratio of the H_2 flux in the presence of 1000 ppm H_2S to the H_2 flux in pure H_2,

$$\text{Sulfur Tolerance} = \frac{\text{H}_2 \text{ flux in 1000 ppm H}_2\text{S}}{\text{H}_2 \text{ flux in pure H}_2},$$

then the sulfur tolerance of $Pd_{47}Cu_{53}$ at 623 K is zero. Figure 3.12 shows the sulfur tolerance of $Pd_{47}Cu_{53}$ in the 623 to 1023 K temperature range. The sulfur tolerance of $Pd_{47}Cu_{53}$ increases smoothly from zero at 623 K to one at ~900 K, at which point exposure to 1000 ppm H_2S has no effect on the rate of H_2 permeation through $Pd_{47}Cu_{53}$. There are several possible explanations for both the low sulfur tolerance at low temperatures and the high sulfur tolerance at high temperatures. At low temperature, the Pd-Cu-S surface is either inactive for H_2 dissociation or is impermeable to H atoms. The sulfur tolerance observed at high temperatures could be due to a lower stability of the thin Pd-Cu-S terminal layer at high temperature or simply due to higher H_2 dissociation rates or higher rates of H atom transport from the surface to the bulk at high temperature. The effect of H_2S on H_2 dissociation over $Pd_{47}Cu_{53}$ will be discussed further in Chapter 5.

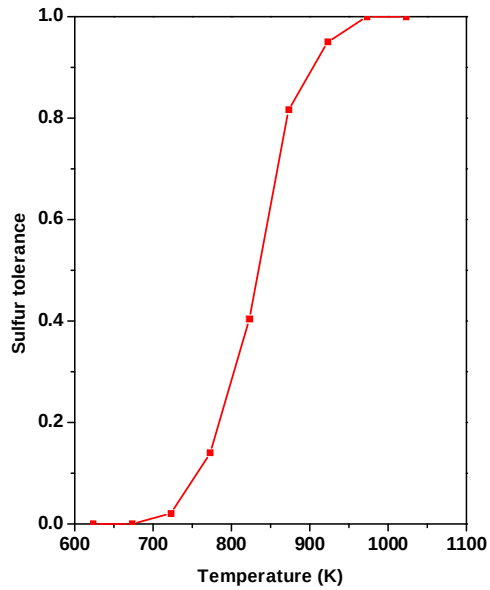

Figure 3.12 Sulfur tolerance, which is defined as the ratio of the H_2 flux measured in the presence of 1000 ppm H_2S to the H_2 flux measured in pure H_2, of the $Pd_{47}Cu_{53}$ alloy versus temperature. The sulfur tolerance of the $Pd_{47}Cu_{53}$ alloy increases smoothly from zero at 623 K to one at ~900 K, at which point exposure to 1000 ppm H_2S has no effect on hydrogen permeation through the alloy.

3.6 Conclusions

In the 623 to 723 K temperature range, the intrinsic H atom permeabilities of Pd and $Pd_{47}Cu_{53}$ are similar; however, their responses to 1000 ppm H_2S at 623 K are significantly different. The Pd membrane is still permeable to H_2 after 6 hours of H_2S exposure with a H_2 flux that decreases slowly over time. In contrast, the $Pd_{47}Cu_{53}$ alloy is impermeable to H_2 after less than 5 minutes of H_2S exposure. Analysis of the Pd and $Pd_{47}Cu_{53}$ foils by x-ray diffraction, scanning electron microscopy, and x-ray photoelectron spectroscopy shows that H_2S reacts with Pd to form a relatively thick (~µm) palladium sulfide (Pd_4S) film, whereas sulfur penetrates only a few nm into the bulk of $Pd_{47}Cu_{53}$. The very low H atom permeability of Pd_4S, which is about an order-of-magnitude lower than that of Pd, is partially responsible for retarding hydrogen permeation through Pd; however, H_2S also inhibits hydrogen transport across Pd directly, possibly by blocking H_2 dissociation sites. The thin Pd-Cu-S layer that forms on the surface of the $Pd_{47}Cu_{53}$ alloy during H_2S exposure is either inactive for H_2 dissociation or is impermeable to H atoms at 623 K. At higher temperatures, the influence of H_2S on hydrogen permeation through $Pd_{47}Cu_{53}$ decreases until exposure at ~900 K to 1000 ppm H_2S has no effect on the rate of H_2 permeation.

Chapter 4

The Kinetics of H_2-D_2 Exchange over Pd, Cu, and PdCu Surfaces

4.1 Summary

PdCu alloy membranes are promising candidates for hydrogen separation from sulfur-containing gas mixtures. H_2 adsorption and desorption are important steps in hydrogen transport across PdCu membranes, but the kinetics of H_2 adsorption and desorption on PdCu surfaces is not well understood. In this chapter, the energetics of H_2 adsorption and desorption on Pd, Cu, and PdCu surfaces is investigated by microkinetic analysis of the H_2-D_2 exchange reaction ($H_2 + D_2 \rightarrow 2HD$) over fixed beds of Pd, Cu, $Pd_{70}Cu_{30}$, and $Pd_{47}Cu_{53}$ foil at near-ambient pressure. The rate of H_2-D_2 exchange over Cu, which is the least active H_2-D_2 exchange catalyst in this study, is limited by the rate of H_2 and D_2 adsorption due to the large activation barrier to H_2 adsorption on Cu (0.54 ± 0.06 eV). The crystal structures of Pd (β-Pd-hydride and α-Pd-hydride) and of $Pd_{47}Cu_{53}$ (body-centered-cubic (BCC) and face-centered-cubic (FCC)) have a significant impact on the kinetics of H_2-D_2 exchange. The activation barriers to H_2 adsorption on β-Pd-hydride (0.3 ± 0.1 eV), α-Pd-hydride (0.12 ± 0.04 eV), $Pd_{70}Cu_{30}$ (0.09 ± 0.02 eV), BCC $Pd_{47}Cu_{53}$ (0.15 ± 0.02 eV), and FCC $Pd_{47}Cu_{53}$ (0.00 ± 0.02 eV) are relatively small compared to that on Cu. The rate of H_2-D_2 exchange over these catalysts (other than Cu) is determined mostly by the rate of H_2 desorption (desorption-limited). As expected, the order of decreasing H_2-D_2 exchange activity in the desorption-limited catalysts (FCC $Pd_{47}Cu_{53}$ > $Pd_{70}Cu_{30}$ > BCC

$Pd_{47}Cu_{53}$ > β-Pd-hydride > α-Pd-hydride) follows closely the order of increasing barrier to H_2 desorption: FCC $Pd_{47}Cu_{53}$ (0.46 ± 0.03 eV) < $Pd_{70}Cu_{30}$ (0.52 ± 0.02 eV) < β-Pd-hydride (0.63 ± 0.03 eV) < BCC $Pd_{47}Cu_{53}$ (0.67 ± 0.03 eV) < α-Pd-hydride (0.68 ± 0.06 eV). These results are significant because they show that, although the rate of H_2 adsorption on Cu is very low, Pd can be alloyed with as much as ~50 mol% Cu without significantly reducing H_2 adsorption rates.

4.2 Introduction

Pd membranes are attractive options for hydrogen separation and purification applications because of their near-infinite selectivity to H_2 separation and their high permeability to H_2 [10, 17]. However, pure Pd is susceptible to hydrogen embrittlement from the expansion of the Pd lattice during β-Pd-hydride formation [60, 61]. Furthermore, H_2S, a coal gasification byproduct, severely inhibits hydrogen permeation through pure Pd [1, 7, 9, 22, 24, 25]. PdCu alloys have exhibited resistance to hydrogen embrittlement [62] and improved sulfur tolerance relative to Pd [9, 19, 22, 29, 33, 34]. $Pd_{70}Cu_{30}$ and $Pd_{47}Cu_{53}$ (mol%) are two particularly attractive PdCu alloy compositions because of their sulfur tolerance and because of their relatively high permeability to H_2 [7, 9, 10, 19, 21]. Unlike the $Pd_{70}Cu_{30}$ alloy, which has only a FCC crystal structure in the temperature range of ~500 K to ~1200 K [9, 10], the $Pd_{47}Cu_{53}$ crystal structure is body-centered-cubic (BCC) at temperatures below ~700 K, and face-centered-cubic (FCC) at temperatures above ~800 K [10, 22, 43]. The H_2 permeability of the BCC crystal structure of $Pd_{47}Cu_{53}$ is about an order-of-magnitude greater than that of the FCC crystal structure of $Pd_{47}Cu_{53}$ [7, 9, 10].

In order to separate H_2 from mixed gas streams, Pd-based membranes must dissociatively adsorb H_2 on the upstream surface of the membrane and recombinatively desorb H_2 from the downstream surface. The energetics of H_2 dissociation over pure Pd and pure Cu have been well characterized; H_2 dissociates on Pd without significant activation barriers [12-16], whereas H_2 dissociation over Cu is hindered by a very large activation barrier (~0.5-0.7 eV)

[63-73]. However, the effect of alloying Pd with Cu on the energetics of the H_2 dissociation reaction is not well understood.

In this chapter, the energetics of H_2 dissociative adsorption and recombinative desorption on Pd, Cu, $Pd_{70}Cu_{30}$, and $Pd_{47}Cu_{53}$ foil surfaces is investigated by microkinetic analysis of the H_2-D_2 exchange reaction ($H_2 + D_2 \rightarrow 2HD$) over these metals at near ambient pressure. We will show that there is a large activation barrier (~0.54 eV) to dissociative adsorption of H_2 on the Cu surface. In contrast, barriers to H_2 dissociation over Pd, $Pd_{70}Cu_{30}$, and $Pd_{47}Cu_{53}$ are relatively small. We will also show that the crystal structures of Pd (β-Pd-hydride and α-Pd-hydride) and of $Pd_{47}Cu_{53}$ (BCC and FCC) have a significant impact on the kinetics of H_2-D_2 exchange. Our results indicate that, although Cu has a very low H_2 dissociation activity, Pd can be alloyed with as much as ~50 mol% Cu without significantly reducing H_2 dissociation rates.

4.3 Experimental

H_2-D_2 exchange experiments were performed by flowing H_2, D_2, and Ar through a 4 mm I.D. quartz tube reactor that was packed with diced Pd, Cu, $Pd_{70}Cu_{30}$, or $Pd_{47}Cu_{53}$ foil while the product gas composition was analyzed by a mass spectrometer. A schematic of the H_2-D_2 exchange reactor is shown in Chapter 2 (Figure 2.2). The Pd (Alfa Aesar, 25 μm thick, 99.9% metals purity), Cu (Alfa Aesar, 100 μm thick, 99.95% metals purity), $Pd_{70}Cu_{30}$ (ACI Alloys, Inc., 100 μm thick, 99.0% metals purity), and $Pd_{47}Cu_{53}$ (ATI Wah Chang, 25 μm thick, 99.0% metals purity) foil was diced into ~1 mm^2 pieces. The total surface

area of each catalyst used was ~19 cm^2. A thermocouple was fixed with a metal wire to the outside of the quartz tube reactor near the catalyst. A tube furnace (Barnstead/Thermolyne 211000) was used to heat the reactor. Mass flow controllers (Aalborg GFC 17) regulated the flow rates of H_2 (99.999%, Valley National Gases), D_2 (99.999 %, Valley National Gases), and Ar (99.999%, Valley National Gases) to the catalyst bed. A ~1 m long, 320 µm I.D. quartz capillary (Polymicro Technologies) was sealed into the outlet of the quartz tube reactor and the product gas was sampled by a ~15 cm long, 20 µm I.D quartz capillary (Polymicro Technologies) that was mounted to a vacuum chamber with a mass spectrometer (Stanford Research Systems, RGA 200).

The $Pd_{47}Cu_{53}$ alloy has a BCC crystal structure at temperatures below ~700 K and a FCC crystal structure at temperatures above ~800 K [10, 22, 43]. H_2-D_2 exchange experiments were performed over both the BCC and FCC phases of the $Pd_{47}Cu_{53}$ alloy. Over the temperature range that the experiments with the $Pd_{47}Cu_{53}$ alloy were conducted (200-500 K), only the BCC crystal structure was stable. To produce the FCC crystal structure, the alloy was first annealed at ~1000 K for ~24 and then cooled quickly (~15 minutes) to ~400 K to quench the FCC crystal structure. To produce the BCC structure, the $Pd_{47}Cu_{53}$ alloy was annealed in H_2 at ~700 K for ~48 hours. The crystal structures of the BCC and FCC alloy were verified by x-ray diffraction (XRD) *following* H_2-D_2 exchange experiments. The crystal structures of BCC $Pd_{47}Cu_{53}$ and of FCC $Pd_{47}Cu_{53}$ did not change during the H_2-D_2 exchange experiments.

Each catalyst was initially heated in H_2 to ~700 K (~1000 K for Cu and FCC $Pd_{47}Cu_{53}$) and held at that temperature for ~24 hours. We found that this heat treatment was necessary because a hysteresis in the HD production rate was observed when the experiments began at low temperature without an initial heat treatment. Figure 4.1 shows the HD flow rate exiting a Cu foil catalyst bed (a) without the initial heat treatment and (b) with the initial heat treatment. Without the initial heat treatment, H_2-D_2 exchange rates were measured over the Cu foil catalyst bed during heating of the Cu foil catalyst and then during the cooling of the catalyst. The HD flow rate exiting the Cu foil catalyst bed was lower during the initial heating of the catalyst than it was during the subsequent cooling of the catalyst. With the initial heat treatment to 1000 K, the experiment was done during cooling from high temperature and then during heating. The HD flow rate exiting the Cu foil catalyst bed was nearly identical during the cooling and heating branches after the initial heat treatment to 1000 K. It is possible that this initial heat treatment in H_2 is necessary to remove contaminants from the catalyst surface.

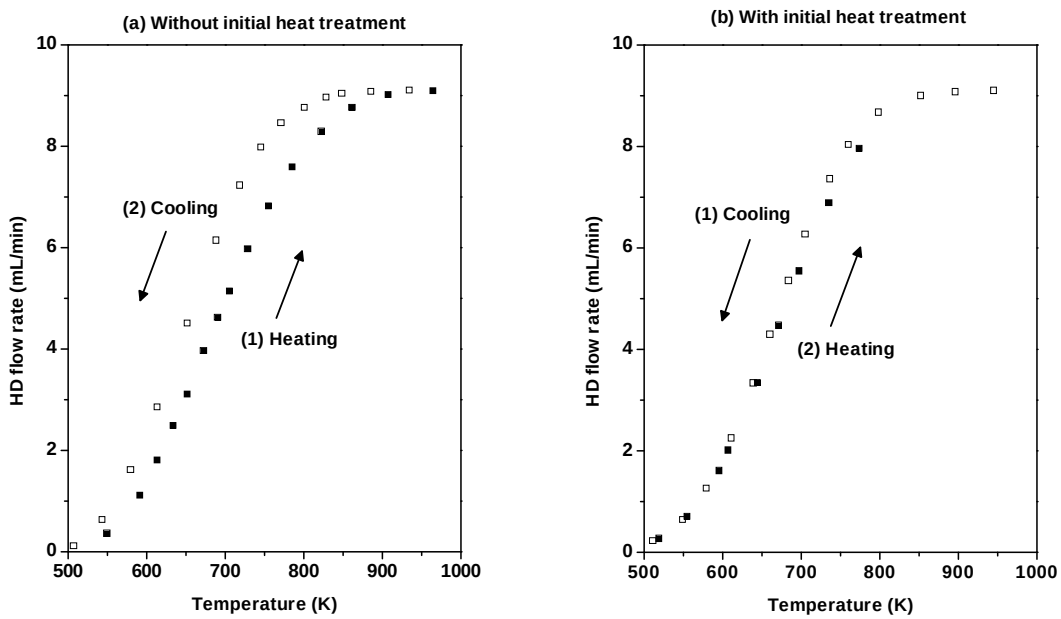

Figure 4.1 HD flow rates exiting a Cu foil catalyst bed (a) without an initial heat treatment and (b) with an initial heat treatment of the Cu catalyst in H_2 at 1000 K. Without the initial heat treatment, the HD flow rate exiting the Cu foil catalyst bed during the initial heating stage of the experiment (filled squares) is lower than the HD flow rate during the subsequent cooling stage (open squares). With the initial heat treatment, the HD flow rate during the initial cooling stage is nearly identical to the HD flow rate in the subsequent heating stage. The initial heat treatment to 1000 K, which may remove contaminants from the catalyst surface, was necessary to eliminate the hysteresis in the HD production rate.

After the initial heat treatment, the $H_2/D_2/Ar$ feed gas mixture was introduced to the reactor. Three different feed gas conditions were used, which are summarized in Table 4.1, to exercise the kinetic model over a range of flow rates and partial pressures of H_2 and D_2. The total pressure in the reactor was measured with a Baratron pressure gauge. Starting from the temperature of the heat treatment, the catalyst was cooled in a step-wise fashion. Steady-state H_2, D_2, and HD mass spectrometer signals were collected at constant temperature to minimize

the effect of H (or D) evolution from, or absorption into, the bulk of the catalyst on the kinetics of the reaction.

Table 4.1 Flow rates of H_2 ($F_{H2,feed}$), D_2 ($F_{D2,feed}$), and Ar ($F_{Ar,feed}$) in the three different feed gas conditions used during H_2-D_2 exchange experiments. Also listed is the total pressure (P_{total}) in the reactor with the three feed gas conditions.

Feed Gas Condition	$F_{H2,feed}$ (mL/min)	$F_{D2,feed}$ (mL/min)	$F_{Ar,feed}$ (mL/min)	P_{total} (kPa)
$9H_2$ / $9D_2$	9	9	0	121
$4.5H_2$ / $4.5D_2$	4.5	4.5	0	113
9Ar / $4.5H_2$ / $4.5D_2$	4.5	4.5	9	135

Mass spectrometer signals were calibrated assuming that the H_2, D_2, and HD mass spectrometer signals sampled from the product gas were proportional to the H_2, D_2, and HD partial pressures exiting the catalyst bed in between the baseline (0% conversion) and equilibrium conversion. Baseline H_2, D_2, and HD mass spectrometer signals were collected by sampling the feed gas directly without passing them through the catalyst bed. At equilibrium the H_2/D_2/HD composition in the product gas is given by:

$$\frac{P_{HD}^2}{P_{H2}P_{D2}} = 4.16\exp\left(\frac{-77.7}{T}\right).$$

where P_{H2}, P_{D2}, and P_{HD} are the partial pressures of H_2, D_2, and HD at equilibrium [74]. H_2, D_2, and HD partial pressures were then converted into H_2, D_2, and HD flow rates:

$$F_i = \frac{F_{total} \cdot P_i}{P_{total}}.$$

where F_i is the flow rate of each species, F_{total} is the total flow rate, P_i is the partial pressure of each species, and P_{total} is the total pressure. The HD flow rates exiting the catalyst bed during H_2-D_2 exchange experiments were used for microkinetic analysis of the H_2-D_2 exchange reaction.

4.4 Kinetic model

We made three basic assumptions in deriving the microkinetic model of the H_2-D_2 exchange reaction:

1) The H_2-D_2 exchange reaction can be modeled by considering only dissociative adsorption and recombinative desorption of H_2, D_2, and HD.
2) Isotopic effects can be ignored (i.e. the adsorption rate constants are the same for H_2, D_2, and HD; and the desorption rate constants are the same for H_2, D_2, and HD).
3) The activation barriers and pre-exponents in the rate constants for adsorption and desorption are independent of coverage and temperature.

With these three simplifying assumptions, derivation of the H_2-D_2 exchange kinetic model requires substitution of the microkinetic expression for the rate of

HD production into the integral mole balance on HD. A detailed derivation of the microkinetic model is given in the Appendix. The flow rate of HD exiting the foil catalyst bed ($F_{\mathrm{HD,out}}$) is given by:

$$F_{\mathrm{HD,out}} = F_{\mathrm{H2,feed}}\left[1-\exp\left(\frac{-k_{\mathrm{ads}}P_{\mathrm{total}}A}{F_{\mathrm{total}}\left(1+\sqrt{2\frac{k_{\mathrm{ads}}}{k_{\mathrm{des}}}P_{\mathrm{H2,feed}}}\right)^{2}}\right)\right] \quad (4.1)$$

where $F_{\mathrm{H2,feed}}$ is the flow rate of H_2 in the feed gas, k_{ads} is the adsorption rate constant, P_{total} is the total pressure in the reactor, A is the catalyst surface area, F_{total} is the total gas flow rate through the reactor, k_{des} is the desorption rate constant, and $P_{\mathrm{H2,feed}}$ is the partial pressure of H_2 in the feed gas. The adsorption rate constant, k_{ads}, and the desorption rate constant, k_{des}, have Arrhenius forms:

$$k_{\mathrm{ads}} = \nu_{\mathrm{ads}}\exp\left(\frac{-E_{\mathrm{ads}}^{\ddagger}}{k_B T}\right)$$

$$k_{\mathrm{des}} = \nu_{\mathrm{des}}\exp\left(\frac{-E_{\mathrm{des}}^{\ddagger}}{k_B T}\right)$$

where ν_{ads} is the adsorption pre-exponent, $E_{\mathrm{ads}}^{\ddagger}$ is the adsorption activation barrier, ν_{des} is the desorption pre-exponent, $E_{\mathrm{des}}^{\ddagger}$ is the desorption activation barrier, k_{B} is the Boltzmann constant, and T is the temperature. The total coverage of H and D atoms during H_2-D_2 exchange is given by:

$$\theta = \frac{\sqrt{2\frac{k_{\mathrm{ads}}}{k_{\mathrm{des}}}P_{\mathrm{H2,feed}}}}{1+\sqrt{2\frac{k_{\mathrm{ads}}}{k_{\mathrm{des}}}P_{\mathrm{H2,feed}}}}. \quad (4.2)$$

The partial pressures of H_2 and D_2 were the same in all experiments so that the coverages of H and D could be assumed to be the same. Equation (4.2) implies that the coverage of H and D atoms is constant along the length of the catalyst bed. To determine the values of ν_{ads}, $E^{\ddagger}_{\text{ads}}$, ν_{des}, and $E^{\ddagger}_{\text{des}}$ that describe H_2 adsorption and desorption on each catalyst, the experimental and modeled HD flow rates exiting the reactor ($F_{\text{HD,out}}$) were first normalized by the flow rate of HD exiting the reactor at equilibrium conversion (F^{eq}_{HD}):

$$X_{\text{HD}} = \frac{F_{\text{HD,out}}}{F^{eq}_{\text{HD}}},$$

where X_{HD} is the conversion of HD. A numerical solver was then used to minimize the error between the model-predicted and experimental HD conversion by adjusting $ln(\nu_{\text{ads}})$, $E^{\ddagger}_{\text{ads}}$, $ln(\nu_{\text{des}})$, and $E^{\ddagger}_{\text{des}}$. The uncertainty in these solver-optimized parameters was estimated with a "SolverAid" program [75].

4.5 Results and discussion

4.5.1 H_2-D_2 exchange over Pd

H_2-D_2 exchange over Pd was carried out by feeding H_2, D_2, and Ar to a Pd foil catalyst bed while the product gas composition was analyzed by a mass spectrometer. Mass spectrometer signals were then converted into flow rates and HD conversion. Figure 4.2(a) shows the HD flow rates exiting the Pd catalyst bed with the three different feed gas conditions: 9 mL/min each of H_2 and D_2, 4.5 mL/min each of H_2 and D_2, and 4.5 mL/min each of H_2 and D_2 diluted with 9 mL/min of Ar.

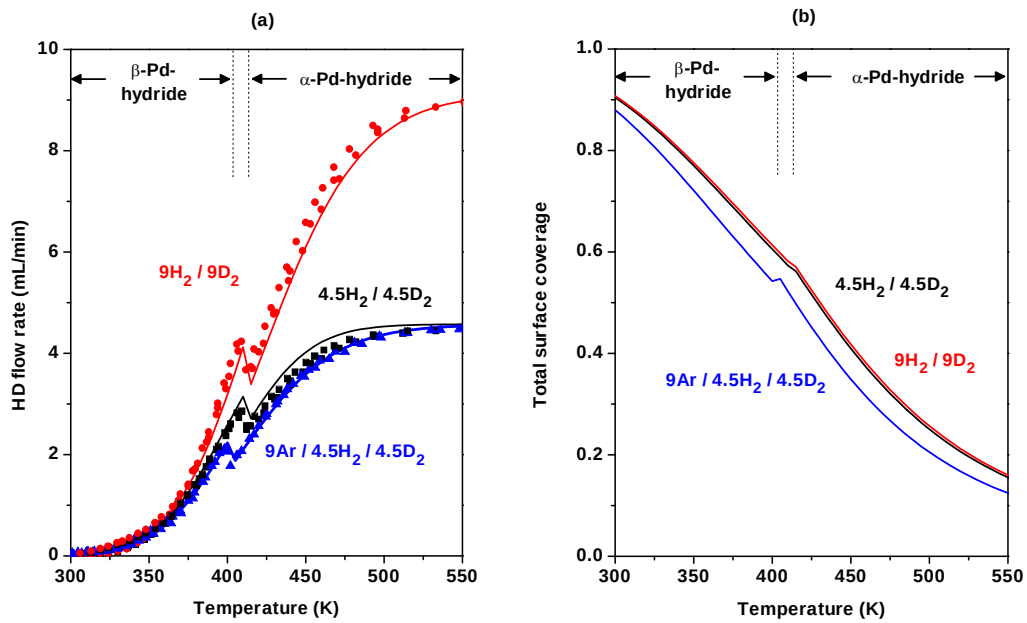

Figure 4.2 (a) Experimental (points) and modeled (lines) HD flow rates versus temperature exiting a ~19 cm^2 Pd foil catalyst bed with three different feed gas conditions: 4.5 mL/min each of H_2 and D_2 ($4.5H_2$ / $4.5D_2$), 9 mL/min each of H_2 and D_2 ($9H_2$ / $9D_2$), and 4.5 mL/min each of H_2 and D_2 diluted with 9 mL/min of Ar (9Ar / $4.5H_2$ / $4.5D_2$). The discontinuity in the HD flow rate is due to a change in the Pd crystal structure from β-Pd-hydride to α-Pd-hydride with increasing temperature. Modeled HD flow rates were calculated using the H_2-D_2 exchange model, equation (4.1), and the solver-optimized values for ν_{ads}, $E^{\ddagger}_{ads}$, ν_{des}, $E^{\ddagger}_{des}$. (b) Total coverage of H and D atoms during H_2-D_2 exchange over the Pd foil catalyst bed. The coverage was calculated using equation (4.2) and the solver-optimized values for ν_{ads}, $E^{\ddagger}_{ads}$, ν_{des}, $E^{\ddagger}_{des}$.

There is a discontinuity in the HD flow rate exiting the Pd foil catalyst bed at ~410 K for both of the pure H_2/D_2 feed gases and at ~400 K for the $Ar/H_2/D_2$ feed gas. The discontinuity in the HD flow occurs at a temperature that is close to the temperature of the β-Pd-hydride to α-Pd-hydride phase transition at a H_2 partial pressure of ~1 atm (see Figure 4.3) [76-78]. The temperature of the β-Pd-

hydride to α-Pd-hydride phase transition decreases with decreasing H_2 partial pressure, which is consistent with the observation that the discontinuity in the HD flow rate in Figure 4.2 (a) occurs at a lower temperature for the $Ar/H_2/D_2$ feed gas than that for the H_2/D_2 feed gases. Therefore, the discontinuity in the HD flow rate exiting the Pd foil catalyst bed is likely due to the β-Pd-hydride to α-Pd-hydride phase transition with increasing temperature; the α-Pd-hydride phase exhibits a lower H_2-D_2 exchange activity than the β-Pd-hydride phase.

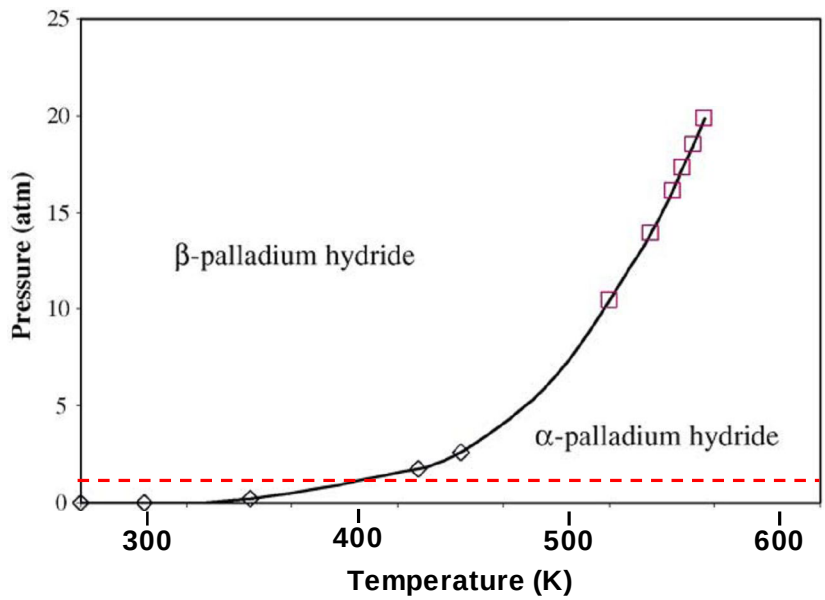

Figure 4.3 Pressure-temperature diagram of the palladium-hydrogen system adapted from [78]. At a hydrogen pressure of ~1 atm, the temperature of the β-Pd-hydride to α-Pd-hydride phase transition is ~400 K, which is similar to the temperature of the discontinuity in the HD flow rate exiting the Pd foil catalyst bed (Figure 4.2(a)). The temperature of the β-Pd-hydride to α-Pd-hydride phase transition decreases with decreasing hydrogen pressure, which could explain why the temperature of the discontinuity in the HD flow rate exiting the Pd foil catalyst bed (Figure 4.2(a)) occurs at a lower temperature when the H_2 pressure in the feed gas is reduced by diluting the H_2/D_2 feed gas with Ar.

It is worth noting that each data point used to generate Figure 4.2(a) was collected at constant temperature; a much different result is obtained by performing the H_2-D_2 exchange experiment over Pd while increasing the temperature of the catalyst at a constant rate. Figure 4.4 shows the partial pressures of H_2, D_2, HD, and Ar in the product gas during H_2-D_2 exchange over the Pd foil catalyst bed while the catalyst temperature was increased at a constant rate of 10 K/min and with feed gas flow rates of 9 mL/min of Ar and 4.5 mL/min each of H_2 and D_2. Because Ar is an inert gas, one would expect that the Ar partial pressure in the product gas would remain constant over the course of the reaction. Instead, there is a dip in the Ar partial pressure in the temperature range ~420 and ~460 K. In that same temperature range, there is a spike in the H_2 and HD partial pressures, and a dip in the D_2 partial pressure. We believe that H_2 evolution from the Pd bulk during the β-Pd-hydride to α-Pd-hydride phase transition is responsible for the spike in the H_2 partial pressure and the dip in the Ar partial pressure. The β-Pd-hydride phase has a much higher concentration of H atoms in its bulk (H:Pd ≈ 0.6) than the α-Pd-hydride phase (H:Pd ≈ 0.03) [79] and, therefore, a large amount of hydrogen must evolve from the Pd bulk during the β-Pd-hydride to α-Pd-hydride phase transition. The solubility of H in Pd is much higher than the solubility of D in Pd [80], which could explain why no spike was observed in the D_2 partial pressure. The temperature of the discontinuity in the steady-state HD flow rate exiting the Pd foil catalyst bed (~400 K) is not exactly the same as the temperature of the spike in the H_2 partial pressure while

the Pd catalyst temperature was increased at a constant rate (~420 to ~460 K). This is probably because the β-Pd-hydride to α-Pd-hydride phase transition does not occur instantaneously.

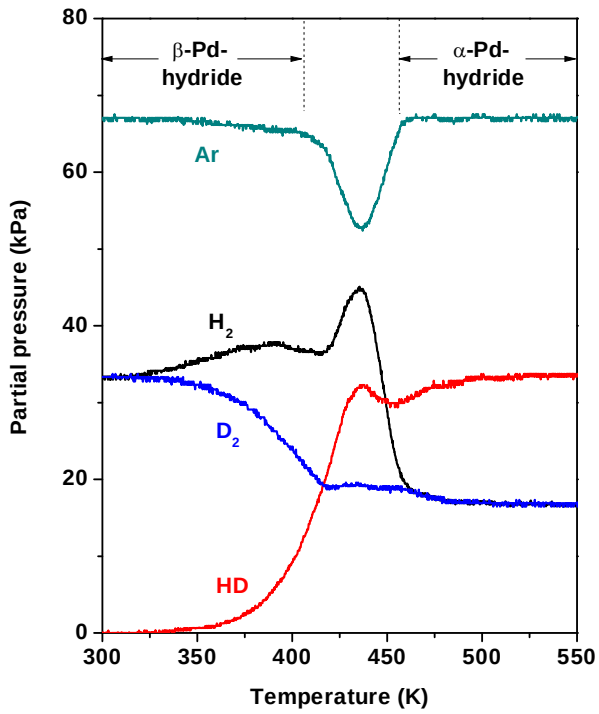

Figure 4.4 Partial pressures of H_2, D_2, HD, and Ar in the product gas during H_2-D_2 exchange over a Pd foil catalyst bed during heating ot the catalyst at 10 K/min and with feed gas flow rates of 9 mL/min of Ar and 4.5 mL/min each of H_2 and D_2. The spike in the H_2 partial pressure in the temperature range ~420 and ~460 K, and the dip in the Ar partial pressure in the same temperature range, is likely due to hydrogen evolution from the bulk of Pd during the β-Pd-hydride to α-Pd-hydride phase transition. The higher solubility of H in Pd than that of D in Pd could explain why no spike was observed in the D_2 partial pressure.

To determine the parameters that describe H_2 adsorption (ν_{ads} and $E^{\ddagger}_{ads}$) and H_2 desorption (ν_{des} and $E^{\ddagger}_{des}$) on β-Pd-hydride and α-Pd-hydride, a numerical solver was used to minimize the error between the modeled and the experimental HD conversion (HD flow rate divided by the HD flow rate at equilibrium) by adjusting $ln(\nu_{ads})$, $E^{\ddagger}_{ads}$, $ln(\nu_{des})$, and $E^{\ddagger}_{des}$. We modeled H_2-D_2 exchange over β-Pd-hydride and α-Pd-hydride separately. The solver-optimized values for the parameters associated with the β-Pd-hydride phase are summarized in Table 4.2.

Table 4.2 Summary of the adsorption pre-exponents (ν_{ads}), adsorption barriers ($E^{\ddagger}_{ads}$), desorption pre-exponents (ν_{des}), desorption barriers ($E^{\ddagger}_{des}$), and heats of adsorption of H_2 (ΔE_{ads}) on β-Pd-hydride and α-Pd-hydride.

	ν_{ads} (mol/m^2/s/Pa)	$E^{\ddagger}_{ads}$ (eV)	ν_{des} (mol/m^2/s)	$E^{\ddagger}_{des}$ (eV)	ΔE_{ads} (eV)
β-Pd-hydride	$10^{-3.7 \pm 0.7}$	0.3 ± 0.1	$10^{5.8 \pm 0.4}$	0.63 ± 0.03	-0.3 ± 0.1
α-Pd-hydride	$10^{-5.4 \pm 0.4}$	0.12 ± 0.04	$10^{6.3 \pm 0.8}$	0.68 ± 0.06	-0.56 ± 0.07

Using the solver-optimized values for ν_{ads}, $E^{\ddagger}_{ads}$, ν_{des}, and $E^{\ddagger}_{des}$ associated with the β-Pd-hydride phase, HD flow rates were calculated with the H_2-D_2 exchange model, equation (4.1), at temperatures less than 410 K (400 K for the 9Ar / 4.5H_2 / 4.5D_2 feed gas). At temperatures greater than 410 K (400 K for the 9Ar / 4.5H_2 / 4.5D_2 feed gas), the solver-optimized parameters associated with the α-Pd-hydride phase were used to calculate HD flow rates. Figure 4.2(a) shows that the modeled HD flow rates fit the experimental HD flow rates reasonably well for both the β-Pd-hydride and α-Pd-hydride phases.

The total coverage of H and D atoms during H_2-D_2 exchange over Pd was calculated with equation (4.2) and the solver-optimized values for v_{ads}, $E^{\ddagger}_{ads}$, v_{des}, and $E^{\ddagger}_{des}$. The values of v_{ads}, $E^{\ddagger}_{ads}$, v_{des}, and $E^{\ddagger}_{des}$ associated with the β-Pd-hydride phase were used to calculate the total coverage at temperatures less than 410 K (400 K for the 9Ar / 4.5H_2 / 4.5D_2 feed gas); and the values of v_{ads}, $E^{\ddagger}_{ads}$, v_{des}, and $E^{\ddagger}_{des}$ associated with α-Pd-hydride were used to calculate the coverage at temperatures greater than 410 K (400 K for the 9Ar / 4.5H_2 / 4.5D_2). Figure 4.2(b) shows the total coverage of H and D atoms during H_2-D_2 exchange over Pd with the three different feed gas conditions. At low temperature (~300 K), the β-Pd-hydride surface is nearly saturated with H and D atoms. As the temperature increases, the total coverage decreases for all three feed gas conditions. Diluting the H_2/D_2 feed gas with Ar (9Ar / 4.5H_2 / 4.5D_2), which reduces the rate of H_2 and D_2 adsorption by lowering the H_2 and D_2 partial pressures, reduces the total coverage of H and D atoms. At ~410 K (400 K for the 9Ar / 4.5H_2 / 4.5D_2), there is a discontinuity in the total coverage due to the β-Pd-hydride to α-Pd-hydride phase transition. As the temperature increases further in the α-Pd-hydride region, the total coverage continues to decrease.

The discontinuity in the HD flow rate exiting the Pd foil catalyst bed (Figure 4.2(a)) clearly indicates that there is a difference in the energetics of H_2 adsorption/desorption on the β-Pd-hydride and α-Pd-hydride surfaces. A comparison of the potential energy of H_2 adsorption on β-Pd-hydride and α-Pd-hydride is shown in Figure 4.5. There is a significantly larger barrier to H_2 adsorption on the β-Pd-hydride (0.3 ± 0.1 eV) surface than on the α-Pd-hydride

(0.12 ± 0.04 eV) surface. The heat of adsorption ($\Delta E_{ads} = E^{\ddagger}_{ads} - E^{\ddagger}_{des}$) of H_2 on the β-Pd-hydride surface (-0.3 ± 0.1 eV) is significantly less negative than that on the α-Pd-hydride surface (-0.56 ± 0.07 eV), indicating that H atoms are less stable on the β-Pd-hydride surface than on the α-Pd-hydride surface. The activation barrier to H_2 desorption from β-Pd-hydride (0.63 ± 0.03 eV) is not significantly different than that from α-Pd-hydride (0.68 ± 0.06).

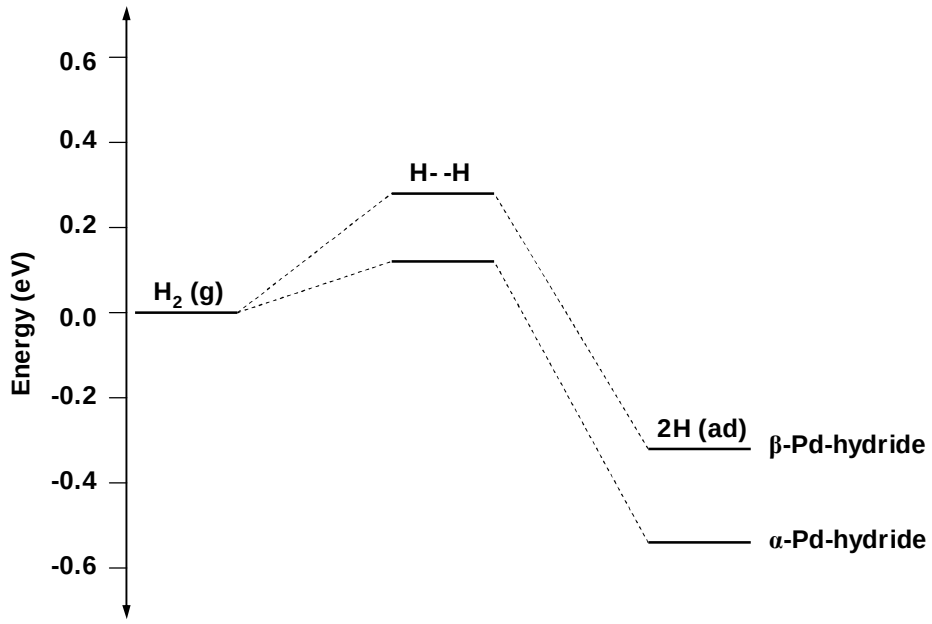

Figure 4.5 Potential energy diagram for H_2 adsorption on β-Pd-hydride and α-Pd-hydride.

There are two main differences in the β-Pd-hydride and α-Pd-hydride phases that might explain the apparent differences in the H_2 adsorption activation barrier and the heat of adsorption of H_2 on the two phases. First, the lattice constant of β-Pd-hydride (~4.02 Å) is significantly larger than the lattice constant

of α-Pd-hydride (~3.89 Å) [81]. Expansion of the Pd lattice has been shown to *increase* the stability of hydrogen adsorption [82], however, which is not consistent with our observation that H atoms are more stable on the surface that has a smaller lattice constant (α-Pd-hydride). Increasing the lattice constant of other metals (e.g. Ru [83]) has also been shown to decrease barriers to adsorption, which is also not consistent with our observations that the barrier to H_2 adsorption is larger on the surface with a larger lattice constant (β-Pd-hydride). Second, there is a much higher concentration of H atoms in the bulk of β-Pd-hydride (H:Pd ≈ 0.6) than in the bulk of α-Pd-hydride (H:Pd ≈ 0.03) [78]. There may also be a higher concentration of H atoms in the sub-surface (the layer just below the surface) of β-Pd-hydride than in the sub-surface of α-Pd-hydride. Sykes *et al.* [84] have shown that H atoms in the Pd(111) sub-surface destabilized H atoms at sites directly above the sub-surface H atoms. Therefore, it is possible that there is a large concentration of H atoms in the sub-surface of β-Pd-hydride that could destabilize H atom adsorption relative to α-Pd-hydride, which may have a much lower concentration of sub-surface H atoms.

There have been many experimental [12, 13, 77, 85-87] and theoretical [27, 28, 77, 88] studies of H_2 adsorption and desorption on Pd surfaces. Most of the experimental studies of H_2 adsorption and desorption on Pd were done with Pd single crystals in ultra-high vacuum. A comparison of our results to many of those in literature is not straightforward because, in this work, polycrystalline Pd foil was used and there was evidence of bulk Pd-hydride formation from exposure to near-ambient pressures of hydrogen. There have been few studies of H_2

adsorption and desorption on polycrystalline Pd-hydride surfaces at near-ambient pressure [77, 85, 87]. In one study [77], the activation barriers to H_2 desorption from β-Pd-hydride and α-Pd-hydride were determined from kinetic analysis of H_2-D_2 exchange over a thin Pd film at near-ambient pressures. The authors reported activation barriers for H_2 desorption from β-Pd-hydride (~0.33 eV) and α-Pd-hydride (~0.27 eV) that were much lower than the values obtained in this work (0.63 ± 0.03 eV on β-Pd-hydride and 0.68 ± 0.06 on and α-Pd-hydride). In their calculation of the desorption barrier, they assumed that the surface was saturated with H atoms and it is possible that an erroneous assumption about the coverage may have influenced their calculation of the H_2 desorption barrier. For example, if we assume that the β-Pd-hydride and α-Pd-hydride surfaces are saturated with H and D atoms in our calculation of the H_2 desorption activation barrier, we obtain activation barriers to H_2 desorption (0.54 eV for β-Pd-hydride and 0.38 eV for α-Pd-hydride) that are significantly lower than if we account for the changing coverage over the temperature range of the H_2-D_2 exchange reaction.

In the same study [77], the energetics of H_2 adsorption on a model Pd-hydride (H:Pd = 0.75) was investigated by density functional theory (DFT) calculations. The authors' results for the adsorption barrier, the desorption barrier, and the heat of adsorption of H_2 on the model Pd-hydride were all in good agreement with those values obtained on β-Pd-hydride in this work. The authors calculated a H_2 adsorption barrier on the model Pd-hydride of ~0.28 eV at high coverage of H [77]: our results indicate that the barrier to H_2 adsorption on β-Pd-hydride is 0.3 ± 0.1 eV at coverages in the range 0.5 to 1. The DFT calculated

heat of adsorption of H_2 on the model Pd-hydride at high coverage [77] was -0.40 eV, which is close to the heat of adsorption of H_2 on β-Pd-hydride obtained in this work (-0.3 ± 0.1 eV). The calculated activation barrier to H_2 desorption on the model Pd-hydride was about 0.68 eV at high coverage [77], which is also close to the activation barrier to H_2 desorption on β-Pd-hydride obtained in this work (0.63 ± 0.03 eV). Although there is a shortage of experimental data on the energetics of H_2 dissociation on Pd-hydride surfaces, our results are in good agreement with DFT calculations.

In summary, there is a discontinuity in the rate of H_2-D_2 exchange over the Pd foil catalyst bed at ~400 K that is related to the β-Pd-hydride to α-Pd-hydride phase transition. Microkinetic analysis of the H_2-D_2 exchange reaction indicates that the energetics of H_2 adsorption on β-Pd-hydride are significantly different than those on α-Pd-hydride. The activation barrier to H_2 adsorption on the β-Pd-hydride surface (0.3 ± 0.1 eV) is significantly higher than that on the α-Pd-hydride surface (0.12 ± 0.04 eV); and the heat of adsorption of H_2 on the β-Pd-hydride surface (-0.3 ± 0.1 eV) is significantly less negative than that on the α-Pd-hydride surface (-0.56 ± 0.07 eV). These differences may be related to differences in sub-surface H atom concentrations in the two phases or due to the differences in the lattice constants of β-Pd-hydride (4.02 Å) and α-Pd-hydride (3.89 Å).

4.5.2 H_2-D_2 exchange over Cu

H_2-D_2 exchange over Cu was carried out using a methodology similar to that used for Pd. Figure 4.6(a) shows the HD flow rates exiting the Cu foil catalyst bed with the three different feed gas conditions: 9 mL/min each of H_2 and D_2, 4.5 mL/min each of H_2 and D_2, and 4.5 mL/min each of H_2 and D_2 diluted with 9 mL/min of Ar. In contrast to Pd, there are no discontinuities in the HD flow rate exiting the Cu foil catalyst bed and there was no evidence of Cu-hydride formation.

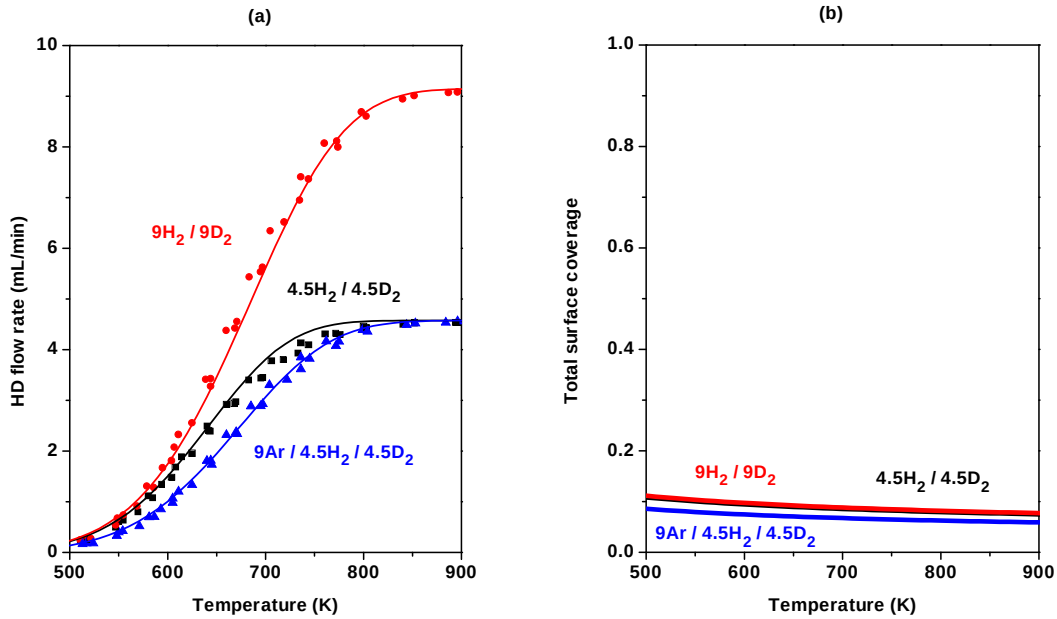

Figure 4.6 (a) Experimental (points) and modeled (lines) HD flow rates versus temperature exiting a Cu foil catalyst bed with three different feed gas conditions: 4.5 mL/min each of H_2 and D_2 ($4.5H_2$ / $4.5D_2$), 9 mL/min each of H_2 and D_2 ($9H_2$ / $9D_2$), and 4.5 mL/min each of H_2 and D_2 diluted with 9 mL/min of Ar (9Ar / $4.5H_2$ / $4.5D_2$). Modeled HD flow rates were calculated with equation (4.1) and the solver-optimized values for ν_{ads}, $E^{\ddagger}_{ads}$, ν_{des}, $E^{\ddagger}_{des}$. (b) Total coverage of H and D atoms during H_2-D_2 exchange over the Cu foil catalyst bed. The total coverage was calculated using equation (4.2) and the solver-optimized values for ν_{ads}, $E^{\ddagger}_{ads}$, ν_{des}, $E^{\ddagger}_{des}$.

The values of ν_{ads}, $E^{\ddagger}_{ads}$, ν_{des}, $E^{\ddagger}_{des}$ that describe H_2 adsorption and desorption on Cu were determined by using a numerical solver to minimize the error between the modeled and the experimental HD conversion by adjusting $ln(\nu_{ads})$, $E^{\ddagger}_{ads}$, $ln(\nu_{des})$, and $E^{\ddagger}_{des}$. The solver-optimized parameters for H_2-D_2 exchange over Cu were as follows: $\nu_{ads} = 10^{-3.4 \pm 0.5}$ mol/m^2/s/Pa, $E^{\ddagger}_{ads} = 0.54 \pm 0.06$ eV, $\nu_{des} = 10^{4 \pm 5}$ mol/m^2/s, and $E^{\ddagger}_{des} = 0.6 \pm 0.7$ eV. The large uncertainty in the desorption pre-exponent ($10^{4 \pm 5}$ mol/m^2/s) and desorption barrier (0.6 ± 0.7 eV) indicates that the rate of H_2-D_2 exchange is insensitive to the parameters associated with H_2 desorption and, therefore, that the rate of H_2-D_2 exchange over Cu is limited by the rate of H_2 adsorption. HD flow rates exiting the Cu foil catalyst were calculated with the H_2-D_2 exchange model, equation (4.1), and the solver-optimized values for ν_{ads}, $E^{\ddagger}_{ads}$, ν_{des}, and $E^{\ddagger}_{des}$; Figure 4.6(a) shows that the model fits the experimental data very well. Because the rate of H_2-D_2 exchange over Cu is limited by the rate of H_2 and D_2 adsorption, which depends on the H_2 and D_2 partial pressures, diluting the $4.5H_2$ / $4.5D_2$ feed gas with Ar (9Ar / $4.5H_2$ / $4.5D_2$) significantly reduces the HD flow rate exiting the Cu foil catalyst bed. This was observed experimentally and was accurately predicted by the model.

Using the solver-optimized values for ν_{ads}, $E^{\ddagger}_{ads}$, ν_{des}, and $E^{\ddagger}_{des}$, the total coverage of H and D atoms during H_2-D_2 exchange over Cu was calculated with equation (4.2) and is plotted in Figure 4.6(b). In contrast to the total coverage of H and D atoms on Pd during H_2-D_2 exchange (Figure 4.2(b)), the total coverage of H and D atoms on the Cu surface is nearly constant throughout the temperature

range of the H_2-D_2 exchange reaction, and is about one-tenth the saturation coverage. The coverage of H and D atoms is low because the activation barrier to H_2 adsorption on Cu is high (0.54 ± 0.06 eV) and, as a result, the rate of adsorption is low.

The energetics of H_2 adsorption and desorption on Cu has been well characterized experimentally [65, 66, 68-70] and theoretically [63, 64, 67, 71, 73] in the literature. Most of the reported values for the H_2 adsorption barrier on Cu single crystals are within the 0.5 to 0.7 eV range [64-73]. Our analysis indicates that the activation barrier to H_2 adsorption on polycrystalline Cu foil is 0.54 ± 0.06 eV, which is in good agreement with the literature. Although the value for the H_2 desorption barrier on Cu (0.6 ± 0.7 eV) obtained from this work has a large uncertainty, Campbell and Campbell [68] reported a barrier to H_2 desorption on Cu(110) of ~0.57 eV, which is similar to our mean value.

4.5.3 H_2-D_2 exchange over $Pd_{70}Cu_{30}$

In this section, the energetics of H_2 dissociation over $Pd_{70}Cu_{30}$ is investigated by microkinetic analysis of the H_2-D_2 exchange reaction over a $Pd_{70}Cu_{30}$ foil catalyst bed. Figure 4.7(a) shows the HD flow rates exiting a $Pd_{70}Cu_{30}$ foil catalyst bed with the three different feed gas conditions.

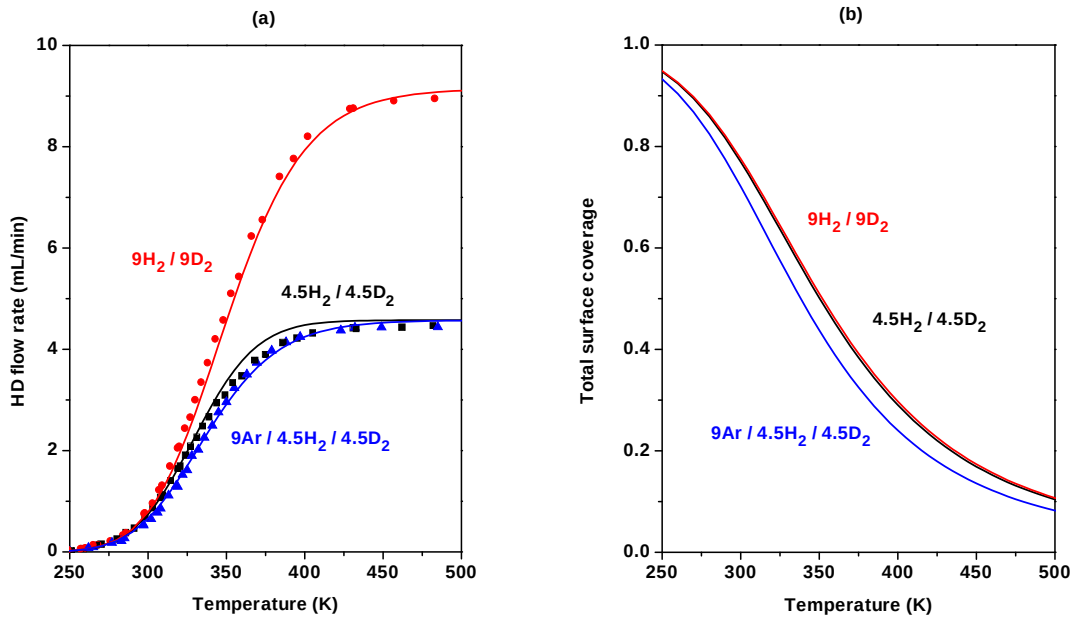

Figure 4.7 (a) Experimental (points) and modeled (lines) HD flow rates versus temperature exiting a $Pd_{70}Cu_{30}$ foil catalyst bed with three different feed gas conditions: 4.5 mL/min each of H_2 and D_2 ($4.5H_2$ / $4.5D_2$), 9 mL/min each of H_2 and D_2 ($9H_2$ / $9D_2$), and 4.5 mL/min each of H_2 and D_2 diluted with 9 mL/min of Ar ($9Ar$ / $4.5H_2$ / $4.5D_2$). Modeled HD flow rates were calculated using the H_2-D_2 exchange model, equation (4.1), and the solver-optimized values for ν_{ads}, $E^{\ddagger}_{ads}$, ν_{des}, $E^{\ddagger}_{des}$. (b) Total coverage of H and D atoms during H_2-D_2 exchange over the $Pd_{70}Cu_{30}$ foil catalyst bed, calculated using equation (4.2) and the solver-optimized values for ν_{ads}, $E^{\ddagger}_{ads}$, ν_{des}, $E^{\ddagger}_{des}$.

Microkinetic analysis of H_2-D_2 exchange over $Pd_{70}Cu_{30}$ was done by minimizing the error between the modeled and the experimental HD conversion. The solver-optimized values of these parameters are as follows: $\nu_{ads} = 10^{-5.6 \pm 0.2}$ mol/m^2/s/Pa, $E^{\ddagger}_{ads} = 0.09 \pm 0.02$ eV, $\nu_{des} = 10^{5.7 \pm 0.3}$ mol/m^2/s, $E^{\ddagger}_{des} = 0.52 \pm 0.02$ eV. These are the first reported experimental measurements of the activation

barriers to H_2 adsorption or desorption on the $Pd_{70}Cu_{30}$ surface, to the best of our knowledge. Using the mean values of these solver-optimized parameters, the predicted HD flow rates were calculated with the H_2-D_2 exchange model, equation (4.1). A comparison of the modeled and experimental HD flow rates is shown in Figure 4.7(a); the model fits the experimental data very well.

The total coverage of H and D atoms during H_2-D_2 exchange over $Pd_{70}Cu_{30}$ was calculated using equation (4.2) and the solver-optimized values for ν_{ads}, $E^{\ddagger}_{\mathrm{des}}$, ν_{des}, and $E^{\ddagger}_{\mathrm{ads}}$. Figure 4.7(b) shows the total coverage of H and D atoms during H_2-D_2 exchange over $Pd_{70}Cu_{30}$ with the three different feed gas conditions. The evolution of the total coverage on the $Pd_{70}Cu_{30}$ surface with increasing temperature is similar to that on Pd and dissimilar to that on Cu. At low temperature (~250 K), the $Pd_{70}Cu_{30}$ surface is nearly saturated with H and D atoms. As the temperature increases, the total coverage decreases. Diluting the feed gas with Ar reduces the rate of adsorption and reduces the total coverage of H and D atoms.

Diluting the H_2/D_2 feed gas with Ar did not significantly reduce the rate of HD production over the $Pd_{70}Cu_{30}$ foil catalyst bed (Figure 4.7(a)). This indicates that the rate of H_2-D_2 exchange over the $Pd_{70}Cu_{30}$ foil catalyst was controlled by the rate of H_2 desorption, which is independent of the H_2 and D_2 partial pressures, rather than by the rate of H_2 adsorption. As a result, there was a relatively high coverage of H and D atoms during H_2-D_2 exchange over $Pd_{70}Cu_{30}$ (Figure 4.7(b)). Microkinetic analysis of H_2-D_2 exchange over $Pd_{70}Cu_{30}$ also indicates that the

barrier to H_2 adsorption on $Pd_{70}Cu_{30}$ (0.09 ± 0.02 eV) is small relative to the barrier to H_2 desorption on $Pd_{70}Cu_{30}$ (0.52 ± 0.02 eV).

4.5.4 H_2-D_2 exchange over $Pd_{47}Cu_{53}$

The $Pd_{47}Cu_{53}$ alloy has a body-centered-cubic crystal (BCC) crystal structure at temperatures less than ~700 K and a face-centered-cubic (FCC) crystal structure at temperatures above ~850 K [9, 32, 43, 62, 89]. H_2-D_2 exchange was performed over both the BCC and FCC phases of the $Pd_{47}Cu_{53}$ alloy. We will show that the crystal structure of $Pd_{47}Cu_{53}$ has a significant impact on the kinetics of H_2-D_2 exchange.

H_2-D_2 exchange over BCC $Pd_{47}Cu_{53}$ and FCC $Pd_{47}Cu_{53}$ was performed by flowing H_2, D_2, and Ar through BCC and FCC $Pd_{47}Cu_{53}$ foil catalyst beds while the product gas was analyzed by a mass spectrometer. The procedure for preparing the BCC and FCC phases is given in Section 4.2. Figure 4.8(a) shows the HD flow rates exiting the BCC and FCC $Pd_{47}Cu_{53}$ foil catalyst beds with three different feed gas conditions. The FCC crystal structure of the $Pd_{47}Cu_{53}$ alloy is significantly more active for H_2-D_2 exchange than the BCC crystal structure.

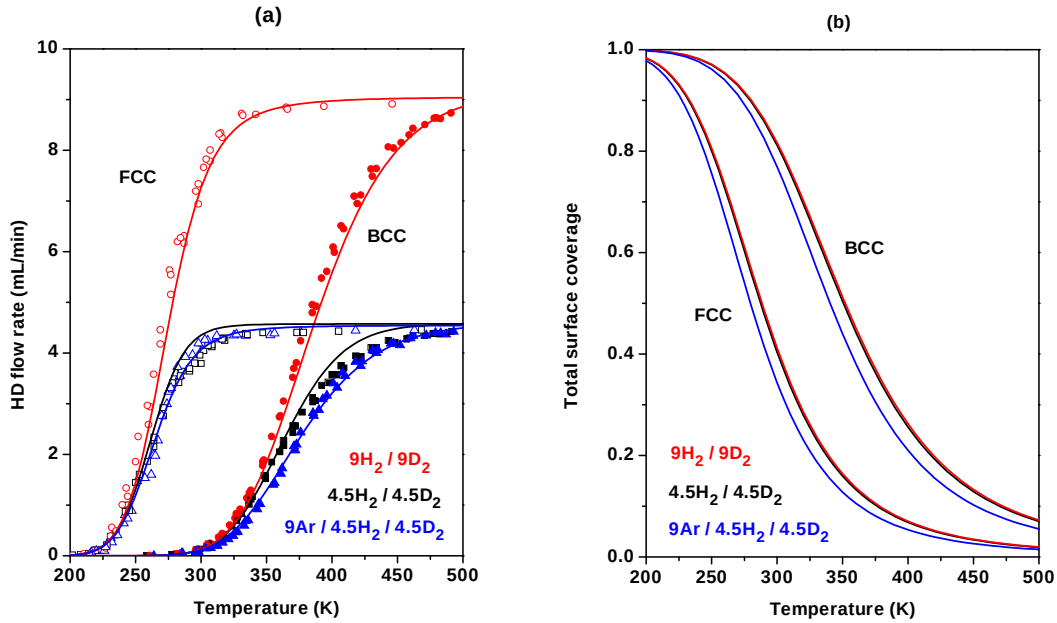

Figure 4.8 (a) Experimental (points) and modeled (lines) HD flow rates versus temperature exiting a $Pd_{47}Cu_{53}$ foil catalyst bed with a body-centered-cubic (BCC) crystal structure and with a face-centered-cubic (FCC) crystal structure. Modeled HD flow rates were calculated using the H_2-D_2 exchange model, equation (4.1), and the solver-optimized values for ν_{ads}, $E^{\ddagger}_{ads}$, ν_{des}, $E^{\ddagger}_{des}$. (b) Total coverage of H and D atoms during H_2-D_2 exchange over the BCC and FCC $Pd_{47}Cu_{53}$ foil catalyst beds. The coverage was calculated using equation (4.2) and the solver-optimized values for ν_{ads}, $E^{\ddagger}_{ads}$, ν_{des}, $E^{\ddagger}_{des}$.

Microkinetic analysis of the H_2-D_2 exchange reaction over the BCC and FCC phases of $Pd_{47}Cu_{53}$ was done by minimizing the error between the modeled and experimental HD conversions by adjusting $ln(\nu_{ads})$, $E^{\ddagger}_{ads}$, $ln(\nu_{des})$, and $E^{\ddagger}_{des}$. The solver-optimized values of these parameters associated with the BCC and FCC phases of $Pd_{47}Cu_{53}$ are summarized in table 4.2. To our knowledge, these are the first reported measurements of the barriers to H_2 adsorption and desorption

on BCC or FCC $Pd_{47}Cu_{53}$ surfaces. Using the solver-optimized parameters, HD flow rates were calculated for the BCC and FCC phases of $Pd_{47}Cu_{53}$ with the three different feed gas conditions. Figure 4.8(a) shows that the model fits the experimental data reasonably well.

Table 4.3 Summary of the adsorption pre-exponents (ν_{ads}), adsorption barriers ($E^{\ddagger}_{ads}$), desorption pre-exponents (ν_{des}), desorption barriers ($E^{\ddagger}_{des}$), and heats of adsorption of H_2 (ΔE_{ads}) on BCC $Pd_{47}Cu_{53}$ and FCC $Pd_{47}Cu_{53}$.

	ν_{ads} (mol/m^2/s/Pa)	$E^{\ddagger}_{ads}$ (eV)	ν_{des} (mol/m^2/s)	$E^{\ddagger}_{des}$ (eV)	ΔE_{ads} (eV)
BCC $Pd_{47}Cu_{53}$	$10^{-5.2 \pm 0.2}$	0.15 ± 0.02	$10^{7.4 \pm 0.5}$	0.67 ± 0.03	-0.52 ± 0.04
FCC $Pd_{47}Cu_{53}$	$10^{-6.6 \pm 0.2}$	0.00 ± 0.02	$10^{6.5 \pm 0.5}$	0.46 ± 0.03	-0.46 ± 0.03

The total coverages of H and D atoms during H_2-D_2 exchange over BCC and FCC $Pd_{47}Cu_{53}$, which are plotted in Figure 4.8(b), were calculated with equation (4.2) and the solver-optimized values of ν_{ads}, $E^{\ddagger}_{ads}$, ν_{des}, and $E^{\ddagger}_{des}$. At low temperatures (~200 K), both the BCC and FCC $Pd_{47}Cu_{53}$ surfaces are nearly saturated with H and D atoms. As the temperature increases, and desorption rate increases, the total coverage decreases on both surfaces. The coverage decreases more rapidly on the FCC phase of $Pd_{47}Cu_{53}$ due to the smaller activation barrier to H_2 desorption on the FCC surface (0.46 ± 0.03 eV) than on the BCC surface (0.67 ± 0.03 eV).

Clearly, the crystal structure of $Pd_{47}Cu_{53}$ has a significant impact on the kinetics of H_2-D_2 exchange due to the differences in the energetics of H_2 adsorption and desorption on the two phases of $Pd_{47}Cu_{53}$. A potential energy diagram that compares the energetics of H_2 adsorption on BCC and FCC $Pd_{47}Cu_{53}$ is shown in Figure 4.9. The activation barriers to H_2 adsorption on BCC $Pd_{47}Cu_{53}$ (0.15 ± 0.02 eV) and on FCC $Pd_{47}Cu_{53}$ (0.00 ± 0.02 eV) are not large and H_2 adsorption rates on both surfaces were high. As a result, the rate of H_2-D_2 exchange over both the BCC and FCC $Pd_{47}Cu_{53}$ surfaces was influenced more by the rate of H_2 desorption than by the rate of adsorption. The higher H_2-D_2 exchange activity exhibited by the FCC phase of $Pd_{47}Cu_{53}$ is due to a lower activation barrier to H_2 desorption on FCC $Pd_{47}Cu_{53}$ (0.46 ± 0.03 eV) than that on BCC $Pd_{47}Cu_{53}$ (0.67 ± 0.03 eV).

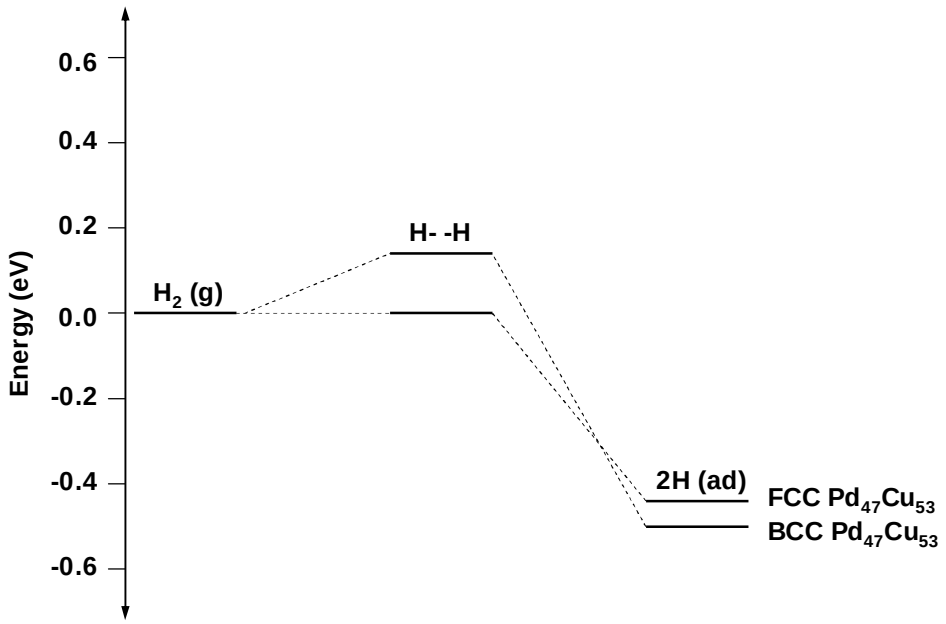

Figure 4.9 Potential energy diagram for H_2 adsorption on BCC $Pd_{47}Cu_{53}$ and FCC $Pd_{47}Cu_{53}$

4.5.5 Comparison of H_2-D_2 exchange over Pd, Cu, $Pd_{70}Cu_{30}$, and $Pd_{47}Cu_{53}$

A comparison of the HD flow rates exiting the Pd, Cu, $Pd_{70}Cu_{30}$, BCC $Pd_{47}Cu_{53}$, and FCC $Pd_{47}Cu_{53}$ catalyst beds, with 9 mL/min each of H_2 and D_2 in the feed gas, is shown in Figure 4.10. The H_2-D_2 exchange activity of Cu is much lower than that of Pd, $Pd_{70}Cu_{30}$, and $Pd_{47}Cu_{53}$ (BCC and FCC); and the PdCu alloys are more active for H_2-D_2 exchange than Pd.

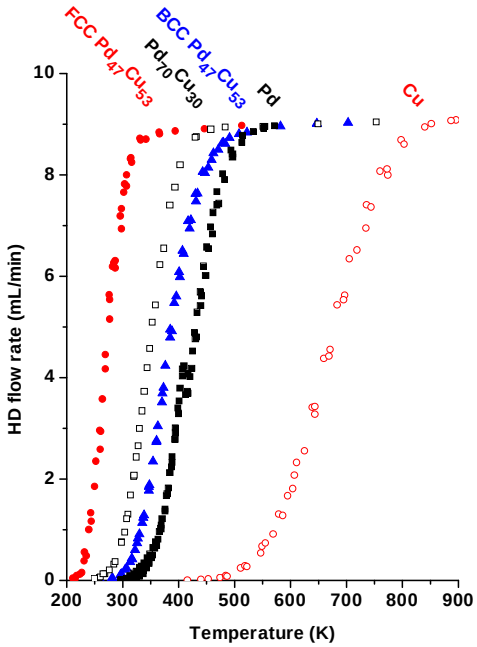

Figure 4.10 Comparison of the HD flow rates exiting Pd, Cu, $Pd_{70}Cu_{30}$, BCC $Pd_{47}Cu_{53}$, and FCC $Pd_{47}Cu_{53}$ foil catalyst beds, each with a catalyst surface area of ~19 cm^2 and 9 mL/min of H_2 and D_2 in the feed gas.

The differences in the H_2-D_2 exchange activity of the catalysts are due to the differences in the energetics of H_2 adsorption and desorption on these catalysts. A comparison of the potential energy of H_2 adsorption on β-Pd-hydride, α-Pd-hydride, Cu, $Pd_{70}Cu_{30}$, BCC $Pd_{47}Cu_{53}$, and FCC $Pd_{47}Cu_{53}$ is shown in Figure 4.11. Table 4.4 lists the parameters that describe H_2 adsorption and desorption (ν_{ads}, $E^{\ddagger}_{ads}$, ν_{des}, $E^{\ddagger}_{des}$, and ΔE_{ads}) on β-Pd-hydride, α-Pd-hydride, Cu, $Pd_{70}Cu_{30}$, BCC $Pd_{47}Cu_{53}$, and FCC $Pd_{47}Cu_{53}$.

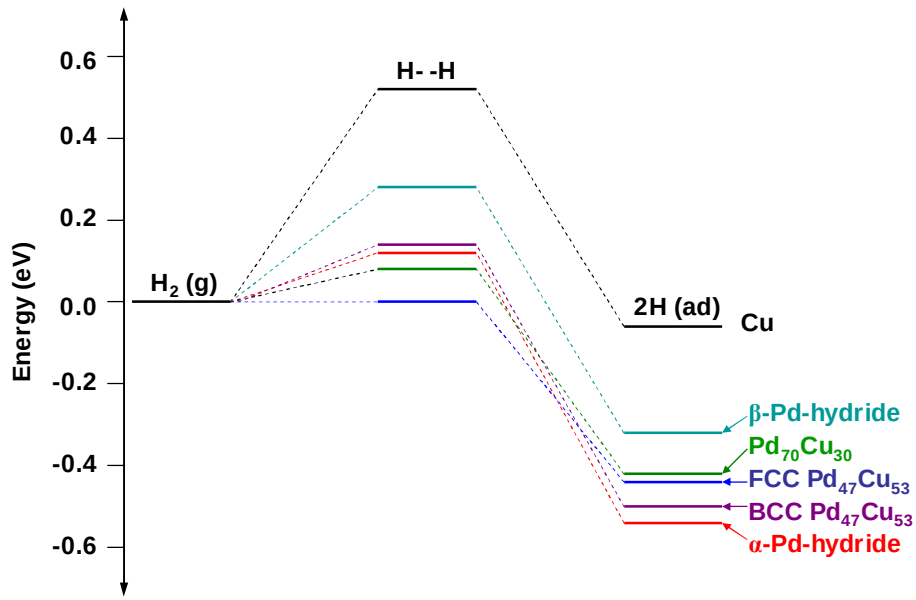

Figure 4.11 Potential energy diagram for H_2 adsorption on Cu, β-Pd-hydride, α-Pd-hydride, $Pd_{70}Cu_{30}$, BCC $Pd_{47}Cu_{53}$, and FCC $Pd_{47}Cu_{53}$.

Table 4.4 Summary of the adsorption pre-exponents (ν_{ads}), adsorption barriers ($E^{\ddagger}_{ads}$), desorption pre-exponents (ν_{des}), desorption barriers ($E^{\ddagger}_{des}$), and heats of adsorption of H_2 (ΔE_{ads}) on β-Pd-hydride, α-Pd-hydride, Cu, $Pd_{70}Cu_{30}$, BCC $Pd_{47}Cu_{53}$, and FCC $Pd_{47}Cu_{53}$ from this work.

	ν_{ads} (mol/m^2/s/Pa)	$E^{\ddagger}_{ads}$ (eV)	ν_{des} (mol/m^2/s)	$E^{\ddagger}_{des}$ (eV)	ΔE_{ads} (eV)
β-Pd-hydride	$10^{-3.7 \pm 0.7}$	0.3 ± 0.1	$10^{5.8 \pm 0.4}$	0.63 ± 0.03	-0.3 ± 0.1
α-Pd-hydride	$10^{-5.4 \pm 0.4}$	0.12 ± 0.04	$10^{6.3 \pm 0.8}$	0.68 ± 0.06	-0.56 ± 0.07
Cu	$10^{-3.4 \pm 0.5}$	0.54 ± 0.06	$10^{4 \pm 5}$	0.6 ± 0.7	0.0 ± 0.7
$Pd_{70}Cu_{30}$	$10^{-5.6 \pm 0.2}$	0.09 ± 0.02	$10^{5.7 \pm 0.3}$	0.52 ± 0.02	-0.43 ± 0.03
BCC $Pd_{47}Cu_{53}$	$10^{-5.2 \pm 0.2}$	0.15 ± 0.02	$10^{7.4 \pm 0.5}$	0.67 ± 0.03	-0.52 ± 0.04
FCC $Pd_{47}Cu_{53}$	$10^{-6.6 \pm 0.2}$	0.00 ± 0.02	$10^{6.5 \pm 0.5}$	0.46 ± 0.03	-0.46 ± 0.03

Cu is the least active H_2-D_2 exchange catalyst in this study due to the large activation barrier to H_2 adsorption on Cu (0.54 ± 0.06 eV). In contrast, barriers to H_2 adsorption on β-Pd-hydride (0.3 ± 0.1 eV), α-Pd-hydride (0.12 ± 0.04 eV), $Pd_{70}Cu_{30}$ (0.09 ± 0.02 eV), BCC $Pd_{47}Cu_{53}$ (0.15 ± 0.02 eV), and FCC $Pd_{47}Cu_{53}$ (0.00 ± 0.02 eV) are relatively small and the rate of H_2-D_2 exchange over these catalysts is determined largely by the rate of H_2 desorption (desorption-limited). FCC $Pd_{47}Cu_{53}$ has the highest H_2-D_2 exchange activity of the desorption-limited catalysts because the activation barrier to H_2 desorption on FCC $Pd_{47}Cu_{53}$ (0.46 ± 0.03 eV) is the smallest. As expected, the order of decreasing H_2-D_2 exchange activity of the desorption-limited catalysts (FCC $Pd_{47}Cu_{53}$ < $Pd_{70}Cu_{30}$ < BCC $Pd_{47}Cu_{53}$ < β-Pd-hydride < α-Pd-hydride) follows closely the order of increasing activation barrier to H_2 desorption: FCC $Pd_{47}Cu_{53}$ (0.46 ± 0.03 eV) < $Pd_{70}Cu_{30}$ (0.52 ± 0.02 eV) < β-Pd-hydride (0.63 ± 0.03 eV) < BCC $Pd_{47}Cu_{53}$ (0.67 ± 0.03 eV) < α-Pd-hydride (0.68 ± 0.06 eV).

The heat of adsorption of H_2 (ΔE_{ads}) on α-Pd-hydride is the lowest (most negative) of the catalysts and, therefore, H atoms are the most stable on α-Pd-hydride. The order of increasing heat of adsorption of H_2 (decreasing stability of H atoms) on the catalysts is as follows: α-Pd-hydride (ΔE_{ads} = -0.56 ± 0.07 eV) < BCC $Pd_{47}Cu_{53}$ (ΔE_{ads} = -0.52 ± 0.04 eV) < FCC $Pd_{47}Cu_{53}$ (ΔE_{ads} = -0.46 ± 0.03 eV) < $Pd_{70}Cu_{30}$ (ΔE_{ads} = -0.43 ± 0.03 eV) < β-Pd-hydride (ΔE_{ads} = -0.3 ± 0.1 eV) < Cu (ΔE_{ads} = 0.0 ± 0.7 eV). The heat of adsorption of H_2 on the PdCu alloys is not much greater (less negative) than that on α-Pd-hydride, indicating that alloying Pd with Cu does not drastically reduce the stability of H atom adsorption.

The pre-exponent for H_2 desorption (ν_{des}) is ~10^6 mol/m^2/s for all of the catalysts used in this study, which is close to the value that would be expected from statistical mechanics (~10^7 mol/m^2/s) if the partition functions of the initial state (adsorbed 2H) and the transition state cancel each other [74]:

$$\nu_{\text{des}} \approx \frac{k_{\text{B}}T}{h} N_{\text{avo}} \sigma_{\text{site}} \approx \left(10^{13}\,\frac{1}{\text{s}}\right)\left(10^{-24}\,\text{mol}\right)\left(10^{18}\,\frac{1}{\text{m}^2}\right) = 10^{7}\,\frac{\text{mol}}{\text{m}^2\text{s}},$$

where k_B is Boltzmann's constant, T is temperature, h is Planck's constant, N_{avo} is Avogadro's number, and σ_{site} is the adsorption site density of a close-packed surface. The pre-exponent for H_2 adsorption (ν_{ads}) is ~10^{-6} mol/m^2/s/Pa for all of the catalysts used in this study. Predicting a pre-exponent for H_2 adsorption from statistical mechanics is more complicated than that for H_2 desorption because the partition functions in the initial state (gas) and the transition state do not cancel each other.

The results of this study are significant because it has been shown that (1) the crystal structures of Pd (β-Pd-hydride and α-Pd-hydride) and of $Pd_{47}Cu_{53}$ (BCC and FCC) have a significant impact on the energetics of H_2 adsorption and desorption; and (2) although the H_2 dissociation activity of Cu is very low, Pd can be alloyed with as much as ~50 mol% Cu without significantly reducing H_2 adsorption rates.

4.6 Conclusions

The energetics of H_2 adsorption on Pd, Cu, $Pd_{70}Cu_{30}$, and $Pd_{47}Cu_{53}$ were investigated in this study by microkinetic analysis of the H_2-D_2 exchange reaction over fixed foil catalyst beds of these catalysts. We found that the crystal structure of Pd (β-Pd-hydride and α-Pd-hydride) and of $Pd_{47}Cu_{53}$ (BCC and FCC) have a significant impact on the kinetics of H_2-D_2 exchange. The H_2-D_2 exchange activity of FCC $Pd_{47}Cu_{53}$ was the highest of all the catalysts in this study and the H_2-D_2 exchange activity of the catalysts decreases in the following order: FCC $Pd_{47}Cu_{53}$ > $Pd_{70}Cu_{30}$ > BCC $Pd_{47}Cu_{53}$ > β-Pd-hydride > α-Pd-hydride >> Cu. The very low H_2-D_2 exchange activity of the Cu catalyst is due to the large activation barrier to H_2 adsorption on Cu (0.54 ± 0.06 eV). Activation barriers to H_2 adsorption on β-Pd-hydride (0.3 ± 0.1 eV), α-Pd-hydride (0.12 ± 0.04 eV), $Pd_{70}Cu_{30}$ (0.09 ± 0.02 eV), BCC $Pd_{47}Cu_{53}$ (0.15 ± 0.02 eV) and FCC $Pd_{47}Cu_{53}$ (0.00 ± 0.02 eV) are small relative to that for Cu and the rate of H_2-D_2 exchange over these catalysts was determined largely by the rate of H_2, D_2, and HD desorption (desorption-limited). These results are significant for H_2 separation membrane applications because it shows that Pd can be alloyed with as much as ~50 mol% Cu without significantly reducing H_2 dissociation rates. The order of decreasing H_2-D_2 exchange activity in the desorption-limited catalysts is nearly the same as the order of increasing activation barrier for H_2 desorption: FCC $Pd_{47}Cu_{53}$ (0.46 ± 0.03 eV) < $Pd_{70}Cu_{30}$ (0.52 ± 0.02 eV) < β-Pd-hydride (0.63 ± 0.03 eV) < BCC $Pd_{47}Cu_{53}$ (0.67 ± 0.03 eV) < α-Pd-hydride (0.68 ± 0.06 eV).

Chapter 5

H_2-D_2 Exchange over Pd_4S, $Pd_{47}Cu_{53}$, and $Pd_{70}Cu_{30}$ in the Presence of H_2S

5.1 Summary

In this chapter, the effect of H_2S on the rate of H_2 dissociative adsorption on Pd_4S, $Pd_{47}Cu_{53}$, and $Pd_{70}Cu_{30}$ foil catalyst beds is investigated by performing H_2-D_2 exchange ($H_2 + D_2 \leftrightarrow 2HD$) over these catalysts in the presence of 50 to 2000 ppm H_2S. Qualitatively, H_2S has the same effect on the rate of H_2-D_2 exchange over Pd_4S, $Pd_{47}Cu_{53}$, and $Pd_{70}Cu_{30}$: increasing the concentration of H_2S in the $H_2/D_2/Ar$ feed gas reduces the rate of HD production by reducing the rate of H_2 adsorption on these catalysts. It is likely that H_2S, or other sulfur species such as SH or S, blocks H_2 adsorption sites on the surfaces of these catalysts and the number of sites blocked for H_2 adsorption increases with increasing H_2S concentration in the feed gas. However, H_2S also causes an irreversible change in the intrinsic H_2-D_2 exchange activity of $Pd_{47}Cu_{53}$, possibly by forming surface sulfides that are difficult to reduce by removing H_2S from the feed gas. In the presence of 50 to 2000 ppm H_2S, the rate of H_2 dissociative adsorption is highest on the Pd_4S catalyst followed by $Pd_{70}Cu_{30}$ and $Pd_{47}Cu_{53}$. Although we have not investigated a wide range of PdCu alloy compositions, our results show that, in the presence of 50 to 2000 ppm H_2S, increasing the Cu content in PdCu alloys reduces the rate of H_2 dissociation on the alloy.

5.2 Introduction

H_2S slows hydrogen transport through Pd membranes indirectly, by producing a Pd_4S film on the Pd surface that is about an order-of-magnitude less permeable to H atoms than Pd, and also slows transport directly, possibly by blocking H_2 dissociation sites on the Pd_4S surface Pd [2, 25]. $Pd_{70}Cu_{30}$ and $Pd_{47}Cu_{53}$ alloys are much more resistant to bulk sulfidation than Pd [1, 9, 29] and hydrogen transport through these alloys is not significantly affected by H_2S at temperatures near 900 K [7, 9, 19]. At lower temperatures (~600 K), however, H_2S blocks hydrogen transport through $Pd_{70}Cu_{30}$ and $Pd_{47}Cu_{53}$ alloys almost completely [9]. Because these alloys do not form thick sulfides, it has been suggested that H_2S poisons the catalytic activity of their surfaces for H_2 dissociation [9]. However, there is very little direct evidence to support this hypothesis. The effect of H_2S on H_2 dissociative adsorption on Pd_4S, $Pd_{47}Cu_{53}$, and $Pd_{70}Cu_{30}$ surfaces has not been investigated to the best of our knowledge.

In this chapter, H_2-D_2 exchange over Pd_4S, $Pd_{47}Cu_{53}$, and $Pd_{70}Cu_{30}$ foil catalyst beds was performed with varying concentrations of H_2S (50 to 2000 ppm) in the feed gas to investigate the effect of H_2S on H_2 dissociative adsorption on these surfaces. We will show that increasing the H_2S concentration in the feed gas reduces the rate of H_2 dissociative adsorption on these catalysts and, as a result, decreases the rate of HD production over these catalysts. We will also show that, in the presence of H_2S, the H_2 dissociation activity of these catalysts decreases with increasing Cu content in the alloy.

5.3 Experimental

H_2-D_2 exchange experiments over Pd alloy foils in the presence of H_2S were performed in a manner similar to the exchange experiments performed in pure H_2 (Chapter 4), except that H_2S was added to the $H_2/D_2/Ar$ feed gas mixture. We used six different H_2S concentrations in the $H_2/D_2/Ar$ feed gas: 50, 100, 200, 500, 1000, and 2000 ppm. The concentration of H_2S in the feed gas mixture was controlled by diluting either a (1.09±0.02%H_2S)/H_2 gas mixture (Matheson Tri-Gas) or a (0.107±0.002%H_2S)/H_2 gas mixture (Matheson Tri-Gas) with pure H_2 (99.999% purity, Valley National Gases). The 0.107%H_2S/H_2 gas mixture was used for H_2S concentrations of 50, 100, and 200 ppm; the 1.09%H_2S/H_2 gas mixture was used for H_2S concentrations of 500, 1000, and 2000 ppm. Three different $H_2/D_2/Ar$ feed gas combinations were used for each H_2S concentration: 9 mL/min of H_2 and D_2 ($9H_2$ / $9D_2$), 4.5 mL/min of H_2 and D_2 ($4.5H_2$ / $4.5D_2$), and 4.5 mL/min of H_2 and D_2 diluted with 9 mL/min of Ar (9Ar / $4.5H_2$ / $4.5D_2$). The total pressure in the reactor was measured with a Baratron pressure gauge and was as follows: 104 kPa for the $4.5H_2$ / $4.5D_2$ feed gases; 107 kPa for the $9H_2$ / $9D_2$ feed gases; and 111 kPa for the 9Ar / $4.5H_2$ / $4.5D_2$ feed gases. Table 5.1 lists the H_2S concentrations and flow rates of the feed gases used in the eighteen different feed gas conditions used for H_2-D_2 exchange experiments in the presence of H_2S.

The total surface area of the foil catalysts used in all experiments was ~19 cm^2. The Pd_4S catalyst was initially prepared in the H_2-D_2 exchange reactor by flowing a 1.09%H_2S/H_2 gas mixture over a pure Pd (Alfa Aesar, 25 μm thick, 99.9% metals purity) foil catalyst bed for ~40 hours at 773 K. Based on the

kinetics of Pd sulfidation [25], this exposure should have been more than sufficient to completely sulfide the Pd foil catalyst bed to Pd_4S.

Prior to the H_2-D_2 exchange experiments, the Pd_4S, $Pd_{70}Cu_{30}$ and $Pd_{47}Cu_{53}$ foil catalyst beds were heated to ~1000 K in a 1000 ppm H_2S in H_2 gas mixture and held at that temperature for ~16 hours. After the initial heat treatment, the $H_2S/H_2/D_2/Ar$ feed gas mixture was introduced to the reactor and the product gas composition was analyzed by a mass spectrometer. Steady-state mass spectrometer signals were collected at constant temperature and the temperature was decreased in a step-wise fashion.

Table 5.1 Feed gas flow rates for the 18 different feed gas conditions used in H_2-D_2 exchange experiments in the presence of H_2S.

Feed Gas Condition	H_2S concentration (ppm)	Feed Gas Flow Rates (mL/min)				
		1%H_2S/ H_2	0.1%H_2S/ H_2	H_2	D_2	Ar
4.5H_2 / 4.5D_2	2000 ± 200	1.65	0	2.86	4.5	0
4.5H_2 / 4.5D_2	1000 ± 200	0.83	0	3.68	4.5	0
4.5H_2 / 4.5D_2	500 ± 200	0.41	0	4.09	4.5	0
4.5H_2 / 4.5D_2	200 ± 20	0	1.68	2.82	4.5	0
4.5H_2 / 4.5D_2	100 ± 20	0	0.84	3.66	4.5	0
4.5H_2 / 4.5D_2	50 ± 20	0	0.42	4.08	4.5	0
9H_2 / 9D_2	2000 ± 100	3.31	0	5.73	9	0
9H_2 / 9D_2	1000 ± 100	1.65	0	7.36	9	0
9H_2 / 9D_2	500 ± 100	0.83	0	8.18	9	0
9H_2 / 9D_2	200 ± 10	0	3.37	5.63	9	0
9H_2 / 9D_2	100 ± 10	0	1.69	7.31	9	0
9H_2 / 9D_2	50 ± 10	0	0.84	8.16	9	0
9Ar / 4.5H_2 / 4.5D_2	2000 ± 100	3.31	0	1.23	4.5	9
9Ar / 4.5H_2 / 4.5D_2	1000 ± 100	1.65	0	2.86	4.5	9
9Ar / 4.5H_2 / 4.5D_2	500 ± 100	0.83	0	3.68	4.5	9
9Ar / 4.5H_2 / 4.5D_2	200 ± 10	0	3.37	1.13	4.5	9
9Ar / 4.5H_2 / 4.5D_2	100 ± 10	0	1.68	2.82	4.5	9
9Ar / 4.5H_2 / 4.5D_2	50 ± 10	0	0.84	3.66	4.5	9

5.4 Results and discussion

5.4.1 H_2-D_2 exchange over Pd_4S in the presence of H_2S

H_2-D_2 exchange over Pd_4S was carried out by feeding a $H_2S/H_2/D_2/Ar$ gas mixture to a Pd_4S foil catalyst bed while the product gas composition was analyzed with a mass spectrometer. Six different concentrations of H_2S (50, 100, 200, 500, 1000, and 2000 ppm) were used in the feed gas, each with three different H_2, D_2, and Ar feed gas flow rates for a total of 18 different feed gas conditions. Figure 5.1 shows the HD flow rates exiting a Pd foil catalyst bed without H_2S in the feed gas compared to the HD flow rates exiting a Pd_4S catalyst bed with 50 ppm H_2S in the feed gas, each with 9 mL/min of H_2 and D_2 in the feed gas. The HD flow rates exiting the Pd_4S catalyst bed *without* H_2S in the feed gas are also shown in Figure 5.1. The rate of HD production over the Pd_4S catalyst bed without H_2S in the feed gas is similar to the rate of HD production over the pure Pd foil catalyst bed. It is likely that the H_2-D_2 exchange activity of Pd_4S in the absence of H_2S is similar to that of Pd because, in the absence of H_2S, the Pd_4S surface is reduced to metallic Pd. In the presence of 50 ppm H_2S, however, the rate of HD production over the Pd_4S catalyst is much lower than that over the Pd catalyst in the absence of H_2S.

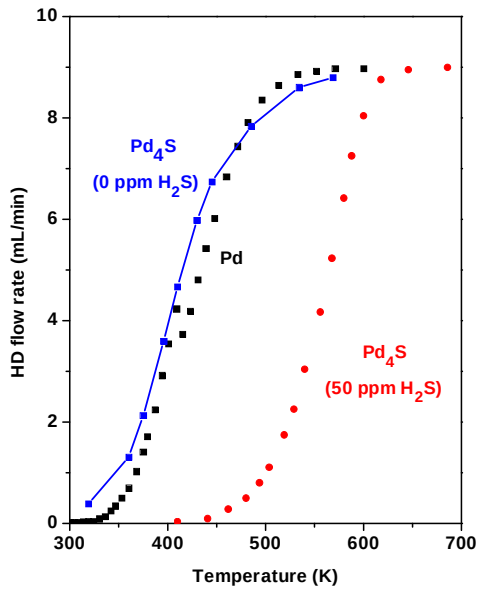

Figure 5.1 Comparison of the HD flow rates exiting a Pd foil catalyst bed without H_2S in the feed gas (Pd), a Pd_4S catalyst bed with 50 ppm H_2S in the feed gas (Pd_4S (50 ppm H_2S)) and a Pd_4S catalyst bed without H_2S in the feed gas (Pd_4S (0 ppm H_2S)), each with 9 mL/min of H_2 and D_2 in the feed gas. The Pd_4S catalyst with 50 ppm H_2S in the feed gas is much less active for H_2-D_2 exchange than the pure Pd catalyst bed without H_2S in the feed gas. The H_2-D_2 exchange activity of the Pd_4S catalyst without H_2S in the feed gas is similar to that of Pd, possibly because the Pd_4S surface is reduced to metallic Pd in the absence of H_2S.

The low rate of HD production over Pd_4S in the presence of 50 ppm H_2S, relative to the HD production rate over the Pd without H_2S in the feed gas, is either due to a low rate of H_2 adsorption or due to a low rate of H_2 desorption. To determine which of these steps (adsorption or desorption) is rate-limiting, we observed the effect of diluting the feed gas with Ar on the HD production rate. Figure 5.2 shows the HD flow rates exiting the (a) Pd foil catalyst bed without H_2S in the feed gas and the (b) Pd_4S catalyst bed with 50 ppm H_2S in the feed gas, each with three different $H_2/D_2/Ar$ feed gas combinations: 9 mL/min of H_2 and D_2, 4.5 mL/min of H_2 and D_2, and 4.5 mL/min of H_2 and D_2 diluted with 9 mL/min of Ar. Diluting the $4.5H_2$ / $4.5D_2$ feed gas with Ar (9Ar / $4.5H_2$ / $4.5D_2$) does not significantly reduce the HD flow rate exiting the Pd foil catalyst bed (Figure 5.1(a)). This observation indicates that the rate of HD desorption, which is independent of the H_2 and D_2 partial pressure, is rate-limiting and the rate of H_2 adsorption is relatively high. In contrast to Pd, diluting the $4.5H_2$ / $4.5D_2$ feed gas with Ar (9Ar / $4.5H_2$ / $4.5D_2$) significantly reduces the HD flow rate exiting the Pd_4S catalyst bed in the presence of 50 ppm H_2S (Figure 5.2(b)), which indicates that H_2 adsorption is rate-limiting. Therefore, the low rate of H_2 adsorption on the Pd_4S surface in the presence of 50 ppm H_2S is responsible for its much lower H_2-D_2 exchange activity than that of Pd without H_2S in the feed gas.

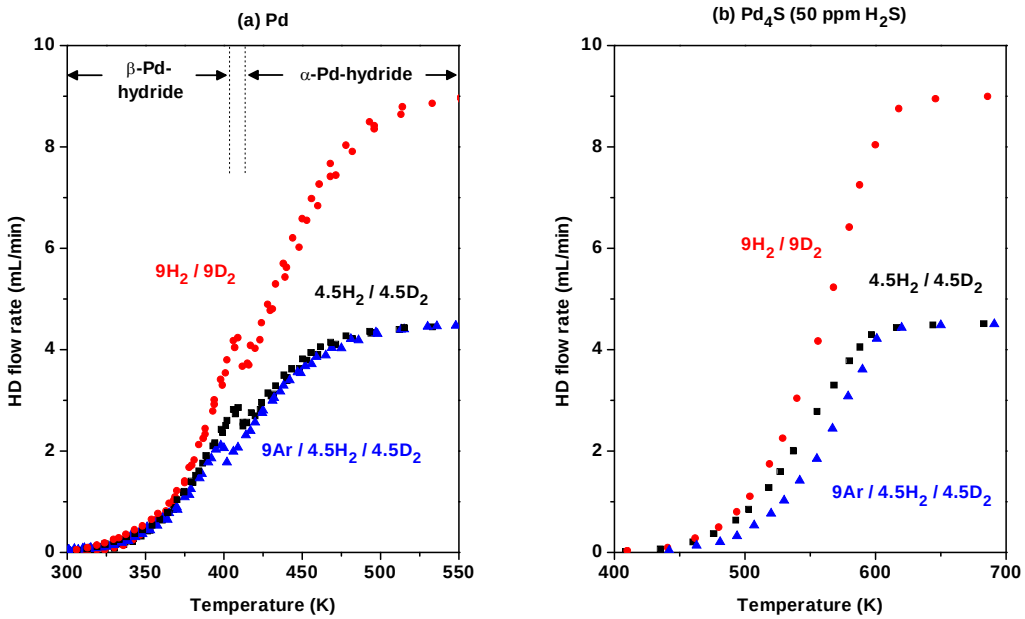

Figure 5.2 HD flow rates exiting the (a) Pd foil catalyst bed and the (b) Pd_4S catalyst bed with 50 ppm H_2S in the feed gas, each with three different $H_2/D_2/Ar$ feed gas combinations: 9 mL/min each of H_2 and D_2 ($9H_2$ / $9D_2$), 4.5 mL/min each of H_2 and D_2 ($4.5H_2$ / $4.5D_2$), and 4.5 mL/min each of H_2 and D_2 diluted with 9 mL/min of Ar (9Ar / $4.5H_2$ / $4.5D_2$). Diluting the $4.5H_2$ / $4.5D_2$ feed gas with Ar (9Ar / $4.5H_2$ / $4.5D_2$) does not significantly reduce the HD flow rate exiting the pure Pd foil catalyst bed, indicating desorption-limited H_2-D_2 exchange. In contrast to Pd, the HD flow rate exiting the Pd_4S catalyst bed in the presence of H_2S is significantly reduced by diluting the H_2/D_2 feed gas with Ar, indicating that the rate of H_2 adsorption on Pd_4S is rate-limiting.

Figure 5.2 suggests that the low H_2-D_2 exchange activity of Pd_4S in the presence of H_2S (relative to Pd in the absence of H_2S) is due to a much lower rate of H_2 adsorption on Pd_4S than on Pd. It is not clear from Figure 5.2(b) whether the Pd_4S surface has an intrinsically low H_2 dissociation activity, or if H_2S reduces the rate of H_2 adsorption directly, or both. To determine whether H_2S reduces the rate of H_2 adsorption on Pd_4S directly, H_2-D_2 exchange over the Pd_4S catalyst was performed with H_2S concentration varying from 50 to 2000 ppm. Figure 5.3 shows the HD flow rates exiting the Pd_4S catalyst bed with 50, 100, 200, 500, 1000, and 2000 ppm H_2S in the feed gas and with three different $H_2/D_2/Ar$ feed gas combinations: (a) 4.5 mL/min each of H_2 and D_2 ($4.5H_2$ / $4.5D_2$), (b) 9 mL/min each of H_2 and D_2 ($9H_2$ / $9D_2$), and (c) 4.5 mL/min of H_2 and D_2 diluted with 9 mL/min of Ar ($9Ar$ / $4.5H_2$ / $4.5D_2$). For all three $H_2/D_2/Ar$ feed gas combinations, increasing the H_2S concentration in the feed gas decreases the rate of H_2-D_2 exchange over the Pd_4S catalyst monotonically. These results indicate that H_2S is directly involved in reducing the rate of H_2 adsorption on Pd_4S, possibly by blocking H_2 dissociation sites.

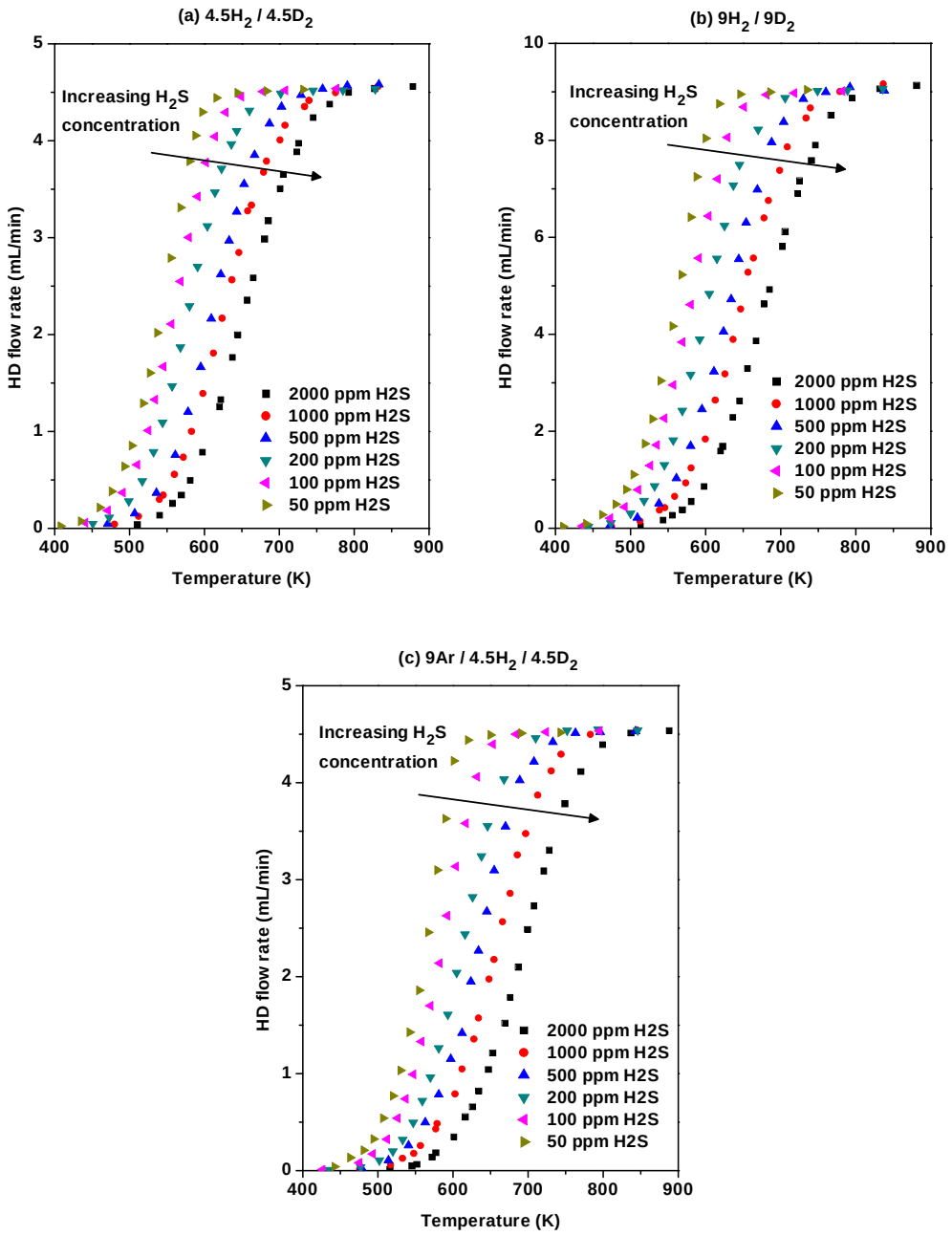

Figure 5.3 HD flow rates exiting a Pd_4S catalyst bed with (a) 4.5 mL/min each of H_2 and D_2 in the feed gas, (b) 9 mL/min each of H_2 and D_2 in the feed gas, and (c) 9 mL/min of Ar with 4.5 mL/min each of H_2 and D_2 in the feed gas, each with H_2S concentrations in the feed gas of 2000, 1000, 500, 200, 100, and 50 ppm. Increasing the H_2S concentration in the feed gas decreases the rate of H_2-D_2 exchange over Pd_4S with all three $H_2/D_2/Ar$ feed gas combinations.

It is not clear from Figure 5.3 whether H_2S blocks H_2 dissociation sites, or if H_2S dissociates on the Pd_4S surface to SH and/or S which could also block H_2 dissociation sites. However, there was evidence that H_2S dissociated on the surface to SH and S. Figure 5.4(a) shows the ratio of the HDS-to-H_2S mass spectrometer signals sampled from the product gas during H_2-D_2 exchange over Pd_4S in the presence of 2000 ppm H_2S and with the three different $H_2/D_2/Ar$ feed gas combinations. Figure 5.4(b) shows the ratio of the D_2S-to-H_2S mass spectrometer signals. The baseline HDS-to-H_2S and D_2S-to-H_2S ratios were determined by sampling the feed gas directly without passing through the Pd_4S catalyst bed.

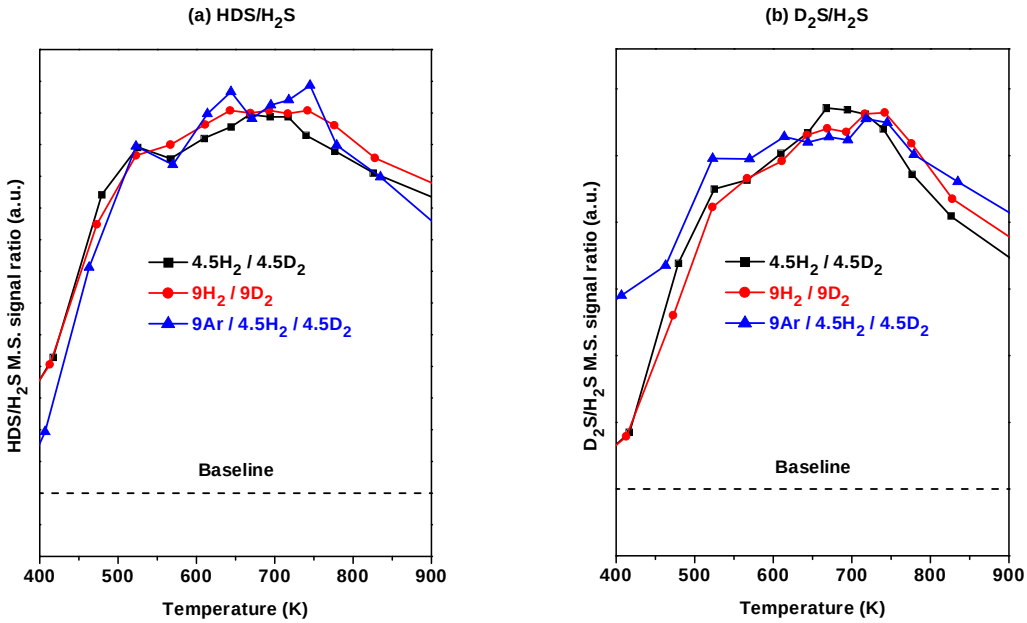

Figure 5.4 Ratio of the (a) HDS-to-H_2S and the (b) D_2S-to-H_2S mass spectrometer signals collected from the product gas during H_2-D_2 exchange over Pd_4S in the presence of 2000 ppm H_2S and with the three different feed gas conditions: 4.5 mL/min of H_2 and D_2 ($4.5H_2$ / $4.5D_2$), 9 mL/min of H_2 and D_2 ($9H_2$ / $9D_2$), and 4.5 mL/min of H_2 and D_2 diluted with 9 mL/min of Ar (9Ar / $4.5H_2$ / $4.5D_2$). The ratio of the HDS-to-H_2S and the D_2S-to-H_2S mass spectrometer signals is greater than the baseline values indicating that H_2S dissociated to SH and S on the Pd_4S surface. These ratios decrease towards the baseline at temperatures less than ~500 K, which is probably due to the very low rate of D_2 adsorption, and the low surface coverage of D atoms, at temperatures less than ~500 K (see Figure 5.3).

The ratio of the HDS-to-H_2S mass spectrometer signals (Figure 5.4(a)) is significantly greater than the baseline value in the 400 K to 900 K temperature range, which indicates that H_2S dissociated to SH on the Pd_4S surface, and D atoms reacted with SH on the Pd_4S surface to produce HDS. The D_2S-to-H_2S mass spectrometer ratios (Figure 5.4(b)) are also significantly greater than the

baseline values. In the 500 K and 800 K temperature range, the HDS-to-H_2S and the D_2S-to-H_2S ratios are roughly constant and it appears that the H_2S/HDS/D_2S gas mixture is equilibrated in this temperature range. At temperatures less than ~500 K, the HDS-to-H_2S and the D_2S-to-H_2S ratios decrease sharply and approach the baseline ratios. This is probably due to the very low rate of D_2 dissociative adsorption on the Pd_4S surface at temperatures less than ~500 K and in the presence of 2000 ppm H_2S (see Figure 5.3). At temperatures less than ~500 K, the HDS-to-H_2S ratio (Figure 5.4(a)) decreases slightly faster for the feed gas diluted with Ar (9Ar / 4.5H_2 / 4.5D_2), than with the other two feed gases. This could be due to the lower rate of D_2 adsorption, and the lower coverage of D atoms, when the H_2/D_2 feed gas is diluted with Ar. Diluting the feed gas with Ar does not result in a sharper decline in the D_2S-to-H_2S ratio (Figure 5.4(b)) at temperatures less than ~500 K. This may be an artifact of the Ar isotope at mass 36 that interferes with the D_2S signal at the same mass.

In conclusion, the H_2-D_2 exchange activity of Pd_4S in the presence of H_2S is much lower than that of Pd in the absence of H_2S due to the much lower rate of H_2 adsorption on Pd_4S relative to Pd. Increasing the H_2S concentration in the feed gas decreases the rate of H_2-D_2 exchange over Pd_4S, which indicates that H_2S is actively involved in reducing the rate of H_2 adsorption on Pd_4S. It is likely that H_2S, SH, or S blocks H_2 dissociative adsorption sites on the Pd_4S surface, although it is not clear which of these species (H_2S, SH, or S) is primarily responsible for reducing the rate of H_2 adsorption on Pd_4S.

5.4.2 H_2-D_2 exchange over $Pd_{47}Cu_{53}$ in the presence of H_2S

In Chapter 4, it was shown that the rate of H_2-D_2 exchange over a $Pd_{47}Cu_{53}$ alloy was dependent on the crystal structure of the alloy, which is body-centered-cubic (BCC) at temperatures less than ~700 K and face-centered-cubic (FCC) at temperatures greater than ~800 K (see Figure 5.5) [32]. H_2 adsorption on both BCC and FCC $Pd_{47}Cu_{53}$ was not hindered by large activation barriers and the rate of H_2-D_2 exchange over both phases was limited by the rate of HD desorption. In this section, the effect of H_2S on the rate of H_2-D_2 exchange over $Pd_{47}Cu_{53}$ is investigated.

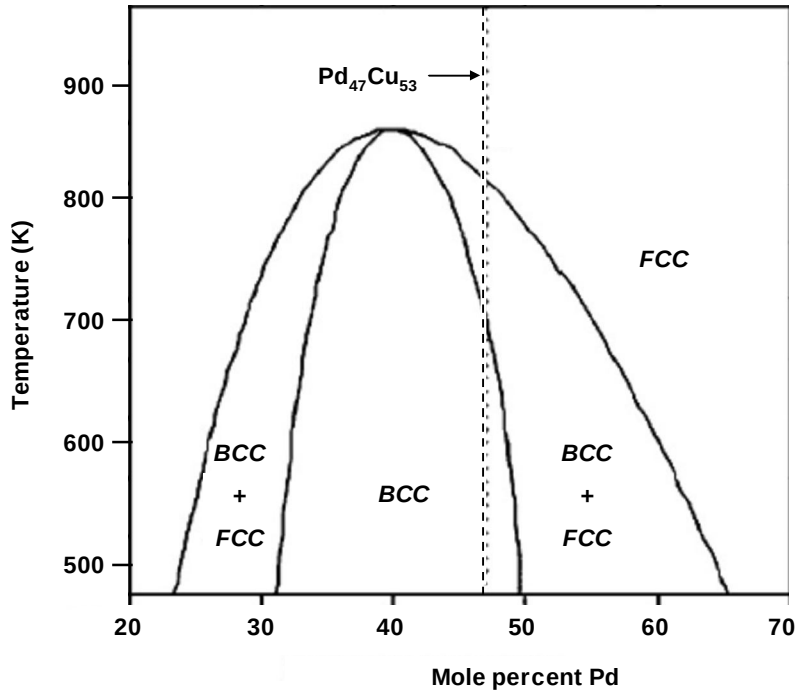

Figure 5.5 Pd-Cu phase diagram adapted from [32]. The $Pd_{47}Cu_{53}$ alloy has a body-centered-cubic (BCC) crystal structure at temperatures less than ~700 K and a face-centered-cubic (FCC) crystal structure at temperatures greater than ~800 K. In between ~700 K and ~800 K, the BCC and FCC phases co-exist in a two-phase structure.

H_2-D_2 exchange over $Pd_{47}Cu_{53}$ was carried out by feeding a $H_2S/H_2/D_2/Ar$ gas mixture to a $Pd_{47}Cu_{53}$ foil catalyst bed while the product gas composition was analyzed by a mass spectrometer. Figure 5.6 shows the HD flow rates exiting a BCC $Pd_{47}Cu_{53}$ foil catalyst bed without H_2S in the feed gas compared to the HD flow rates exiting a $Pd_{47}Cu_{53}$ foil catalyst bed with 50 ppm H_2S in the feed gas, each with 9 mL/min of H_2 and D_2 in the feed gas. Adding 50 ppm H_2S to the feed

gas significantly reduces the rate of HD production over the $Pd_{47}Cu_{53}$ alloy; the onset of H_2-D_2 exchange over $Pd_{47}Cu_{53}$ without H_2S in the feed gas begins at a temperature that is ~200 K lower than that over $Pd_{47}Cu_{53}$ in the presence of 50 ppm H_2S.

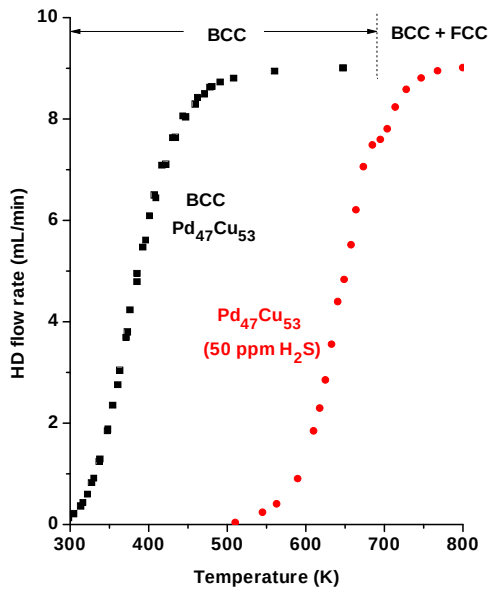

Figure 5.6 Comparison of the HD flow rates exiting a BCC $Pd_{47}Cu_{53}$ foil catalyst bed without H_2S in the feed gas to the HD flow rates exiting a $Pd_{47}Cu_{53}$ foil catalyst bed with 50 ppm H_2S in the feed gas, each with 9 mL/min of H_2 and D_2 in the feed gas. Adding 50 ppm H_2S to the H_2/D_2 feed gas reduces the rate of HD production over the $Pd_{47}Cu_{53}$ catalyst. At ~680 K, there is a break in the HD flow rate exiting the $Pd_{47}Cu_{53}$ catalyst with 50 ppm H_2S in the feed gas, which we believe is due to a change in the $Pd_{47}Cu_{53}$ crystal structure from a mixed BCC/FCC structure at temperatures above ~680 K to a BCC structure at temperatures below ~680 K.

At ~680 K, there is a break in the HD flow rate exiting the $Pd_{47}Cu_{53}$ catalyst bed in the presence of 50 ppm H_2S (see Figure 5.6). The temperature of this break is similar to the temperature of the phase boundary between the BCC phase and the mixed BCC/FCC two-phase region of $Pd_{47}Cu_{53}$ (see Figure 5.5). Therefore, we believe that the break in the HD flow rate exiting the $Pd_{47}Cu_{53}$ foil catalyst bed at ~680 K is due to a change in the crystal structure of $Pd_{47}Cu_{53}$ from a mixed BCC/FCC two-phase structure at temperatures above ~680 K to a BCC structure at temperatures below ~680 K; and the H_2-D_2 exchange activity of $Pd_{47}Cu_{53}$ is different in these two different regions.

The HD production rate over $Pd_{47}Cu_{53}$ is limited by either the rate of H_2 adsorption or by the rate of HD desorption. It is relatively straightforward to identify the rate-limiting step by observing the effect of diluting the feed gas with Ar on the rate of HD production. Figure 5.7 shows the HD flow rates exiting the (a) BCC $Pd_{47}Cu_{53}$ foil catalyst bed without H_2S in the feed gas and (b) the $Pd_{47}Cu_{53}$ foil catalyst bed with 50 ppm H_2S in the feed gas, each with three different $H_2/D_2/Ar$ feed gas combinations. In the absence of H_2S (Figure 5.7(a)), diluting the feed gas with Ar does not significantly reduce the rate of HD production over $Pd_{47}Cu_{53}$ catalyst. This indicates that the rate of HD desorption, which is independent of the H_2 and D_2 partial pressure, limits the rate of HD production over $Pd_{47}Cu_{53}$ in the absence of H_2S. In the presence of 50 ppm H_2S (Figure 5.7(b)), the HD flow rate exiting the $Pd_{47}Cu_{53}$ catalyst bed *is* significantly reduced by diluting the feed gas with Ar, indicating that, in the presence of 50 ppm H_2S, the HD production rate over $Pd_{47}Cu_{53}$ is limited by the rate of H_2

adsorption. Therefore, the rate-limiting step in H_2-D_2 exchange over $Pd_{47}Cu_{53}$ is changed from HD desorption to H_2 adsorption by adding 50 ppm H_2S to the feed gas; and the rate of H_2-D_2 exchange over $Pd_{47}Cu_{53}$ is much lower with 50 ppm H_2S in the feed gas than without (see Figure 5.6) due to the much lower rate of H_2 adsorption on $Pd_{47}Cu_{53}$ in the presence of 50 ppm H_2S.

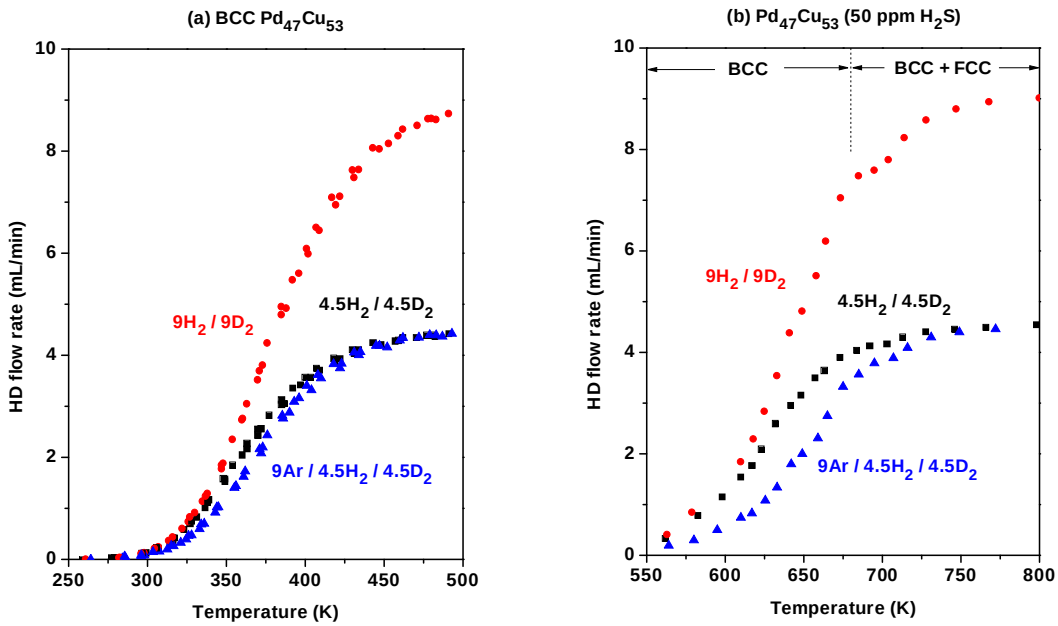

Figure 5.7 HD flow rates exiting (a) the BCC $Pd_{47}Cu_{53}$ foil catalyst bed without H_2S in the feed gas and (b) the $Pd_{47}Cu_{53}$ catalyst bed with 50 ppm H_2S in the feed gas, each with three different $H_2/D_2/Ar$ feed gas combinations: 9 mL/min of H_2 and D_2 ($9H_2$ / $9D_2$), 4.5 mL/min of H_2 and D_2 ($4.5H_2$ / $4.5D_2$), and 4.5 mL/min of H_2 and D_2 diluted with 9 mL/min of Ar (9Ar / $4.5H_2$ / $4.5D_2$). Diluting the $4.5H_2$ / $4.5D_2$ feed gas with Ar (9Ar / $4.5H_2$ / $4.5D_2$) does not significantly reduce the HD flow rate exiting the $Pd_{47}Cu_{53}$ catalyst bed without H_2S in the feed gas, whereas the HD flow rate exiting the $Pd_{47}Cu_{53}$ catalyst bed with 50 ppm H_2S in the feed gas *is* significantly reduced by diluting the feed gas with Ar. These observations indicate that the rate-limiting step in H_2-D_2 exchange over $Pd_{47}Cu_{53}$ is changed from HD desorption to H_2 adsorption by adding 50 ppm H_2S to the feed gas.

The concentration of H_2S in the feed gas was varied from 50 to 2000 ppm to determine the effect of H_2S concentration on the rate of HD production over $Pd_{47}Cu_{53}$. Figure 5.8 shows the HD flow rates exiting the $Pd_{47}Cu_{53}$ foil catalyst bed with H_2S concentrations of 50, 100, 200, 500, 1000, and 2000 ppm and (a) 4.5 mL/min of H_2 and D_2, (b) 9 mL/min of H_2 and D_2, and (c) 4.5 mL/min of H_2 and D_2 diluted with 9 mL/min of Ar. Increasing the H_2S concentration in the feed gas decreases the HD production rate over $Pd_{47}Cu_{53}$ for all three different $H_2/D_2/Ar$ feed gas combinations. Because the rate of HD production over $Pd_{47}Cu_{53}$ is limited by the rate of H_2 adsorption, it is likely that H_2S decreases the HD production rate over $Pd_{47}Cu_{53}$ by blocking H_2 adsorption sites; and increasing the H_2S concentration in the feed gas increases the number of H_2 adsorption sites that are blocked by sulfur species (H_2S, SH, or S).

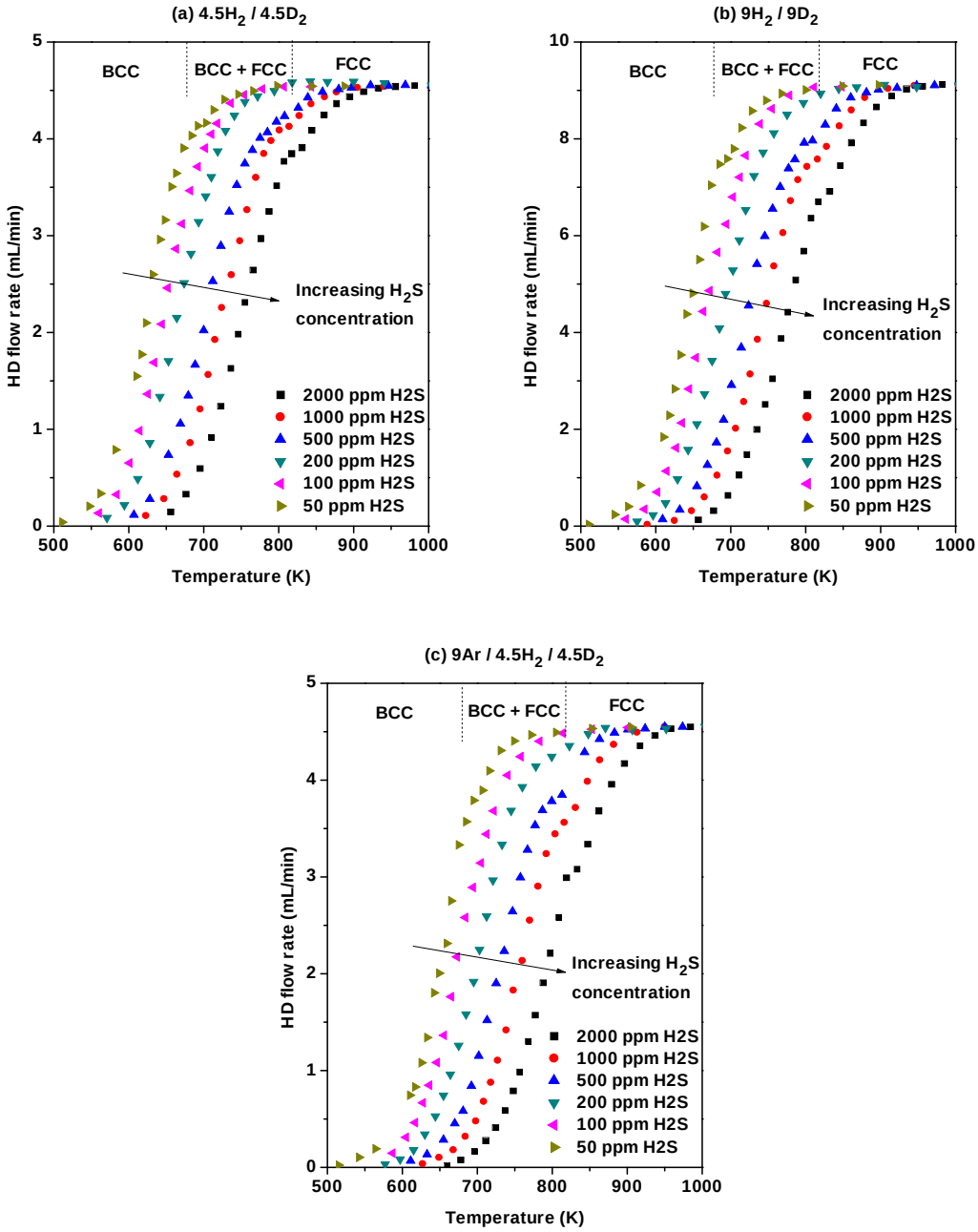

Figure 5.8 HD flow rates exiting a $Pd_{47}Cu_{53}$ foil catalyst bed with H_2S concentrations of 50, 100, 200, 500, 1000, and 2000 ppm in the feed gas and with $H_2/D_2/Ar$ feed gas flow rates of (a) 4.5 mL/min of H_2 and D_2, (b) 9 mL/min of H_2 and D_2, and (c) 4.5 mL/min of H_2 and D_2 diluted with 9 mL/min of Ar. Increasing the H_2S concentration in the feed gas decreases the rate of HD production over $Pd_{47}Cu_{53}$.

In Figure 5.8, there are visible breaks in the HD flow rates at ~680 K and at ~810 K. The temperature of these breaks is similar to the temperature of the phase boundaries in the $Pd_{47}Cu_{53}$ crystal structure (see Figure 5.5). At temperatures above ~810 K, the $Pd_{47}Cu_{53}$ alloy has a FCC crystal structure and at temperatures less than ~680 K the alloy has a BCC crystal structure. In between ~680 K and ~810 K, the BCC and FCC phases co-exist in a mixed structure. The breaks in the HD flow rate exiting the $Pd_{47}Cu_{53}$ foil catalyst bed could be due to changes in the $Pd_{47}Cu_{53}$ crystal structure, and these different phases of $Pd_{47}Cu_{53}$ have different H_2-D_2 exchange activities. This is not an unexpected result, as the H_2-D_2 exchange activities of BCC $Pd_{47}Cu_{53}$ and FCC $Pd_{47}Cu_{53}$ were shown to be significantly different in Chapter 4.

In addition to blocking H_2 adsorption sites, it is also possible that H_2S reacts with the $Pd_{47}Cu_{53}$ surface and alters its intrinsic H_2 dissociation activity. To determine whether H_2S reduces the rate of H_2 adsorption on $Pd_{47}Cu_{53}$ more than by simply blocking H_2 adsorption sites, H_2S was removed from the feed gas during H_2-D_2 exchange over $Pd_{47}Cu_{53}$. Figure 5.9 shows the HD flow rates exiting the $Pd_{47}Cu_{53}$ foil catalyst bed versus time after removing 50 ppm H_2S from the feed gas at 623 K. The HD flow rate exiting a clean $Pd_{47}Cu_{53}$ foil catalyst that had never been exposed to H_2S is marked with a dashed line for comparison. Immediately after removing H_2S from the feed gas, the HD flow rate exiting the $Pd_{47}Cu_{53}$ catalyst bed increases sharply and then gradually approaches a steady-state after ~30 minutes. The steady-state flow rate exiting the sulfur-exposed $Pd_{47}Cu_{53}$ catalyst is still well below that of the clean $Pd_{47}Cu_{53}$ catalyst.

This suggests that H_2S reacts with the $Pd_{47}Cu_{53}$ surface and irreversibly alters its H_2-D_2 exchange activity. The sharp increase in the HD flow rate immediately following removal of H_2S from the feed gas is probably due to an increase in the number of available H_2 adsorption sites as the rate of H_2S adsorption decays to zero. The gradual increase in the HD flow rate over time could be due to the removal of weakly adsorbed sulfur species on the $Pd_{47}Cu_{53}$ surface. Strongly bound surface sulfides may be present on the $P_{d47}Cu_{53}$ surface after 50 minutes of exposure to pure H_2, and these sulfides may be significantly less active for H_2-D_2 than the clean $Pd_{47}Cu_{53}$ surface.

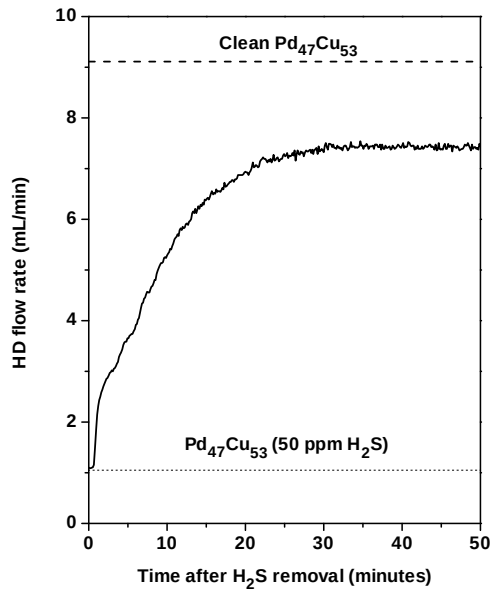

Figure 5.9 HD flow rates exiting a $Pd_{47}Cu_{53}$ foil catalyst bed at 623 K versus time after removing 50 ppm H_2S from a feed gas with 9 mL/min each of H_2 and D_2. The HD flow rate increases sharply immediately following removal of H_2S from the feed gas, and then the flow rate increases more gradually until it reaches a steady-state at ~30 minutes. The steady-state flow rate is still below the HD flow rate exiting a clean $Pd_{47}Cu_{53}$ foil catalyst bed that had never been exposed to H_2S. This result indicates that, in addition to blocking H_2 adsorption sites, H_2S also reacts with the $Pd_{47}Cu_{53}$ surface and irreversibly changes the H_2-D_2 exchange activity of $Pd_{47}Cu_{53}$.

The irreversible decrease in the H_2-D_2 exchange activity of $Pd_{47}Cu_{53}$ from H_2S exposure (Figure 5.9) could be due to the formation of surface sulfides that have an intrinsically lower H_2-D_2 exchange activity than the clean $Pd_{47}Cu_{53}$ surface. Although we do not have proof that surface sulfides are the cause of the irreversible change the H_2-D_2 exchange activity of $Pd_{47}Cu_{53}$, there is evidence that H_2S dissociated on the $Pd_{47}Cu_{53}$ surface to SH and S. Figure 5.10 shows the ratio

of the HDS-to-H_2S and the D_2S-to-H_2S mass spectrometer signals collected from the product gas during H_2-D_2 exchange over $Pd_{47}Cu_{53}$ in the presence of 1000 ppm H_2S. These ratios are significantly greater than the baseline ratios, which were determined by sampling the feed gas directly without passing through the $Pd_{47}Cu_{53}$ catalyst bed. This indicates that H_2S dissociated to SH and S on the surface and these species reacted with D atoms on the $Pd_{47}Cu_{53}$ surface to produce HDS and D_2S. At temperatures below ~600 K, the HDS-to-H_2S and the D_2S-to-H_2S ratios decrease, which is probably due to the low rate of D_2 adsorption on $Pd_{47}Cu_{53}$ at these temperatures (see Figure 5.8) and, as a result, the low coverage of D atoms on the $Pd_{47}Cu_{53}$ surface. These dissociated sulfur species (SH and S) could react with the $Pd_{47}Cu_{53}$ surface to form surface sulfides and irreversibly change the H_2-D_2 exchange activity of $Pd_{47}Cu_{53}$.

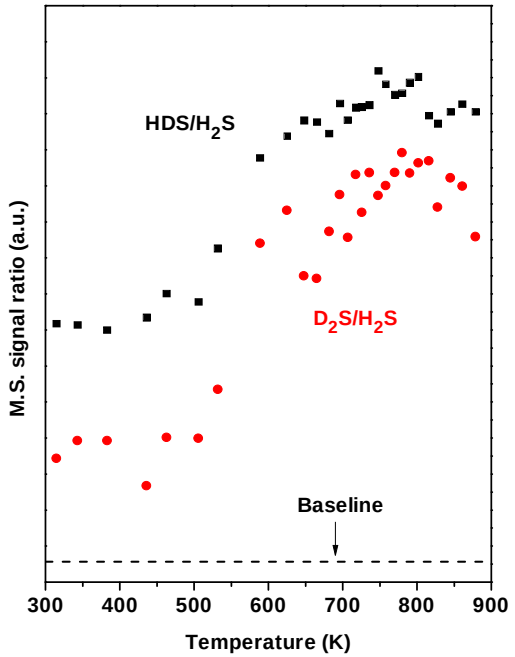

Figure 5.10 HDS-to-H_2S and D_2S-to-H_2S mass spectrometer signal ratios in the product gas during H_2-D_2 exchange over a $Pd_{47}Cu_{53}$ foil catalyst bed in the presence of 1000 ppm H_2S. The HDS-to-H_2S and D_2S-to-H_2S mass spectrometer signal ratios are significantly higher than the baseline, indicating that H_2S dissociates to SH and S on the $Pd_{47}Cu_{53}$ surface.

In summary, the rate of HD production over $Pd_{47}Cu_{53}$ is significantly reduced by adding H_2S to the feed gas due to the much lower rate of H_2 adsorption on $Pd_{47}Cu_{53}$ in the presence of H_2S than without H_2S in the feed gas. Increasing the H_2S concentration in the feed gas decreases the rate of H_2 adsorption on the $Pd_{47}Cu_{53}$ further. This suggests that H_2S blocks H_2 adsorption sites and the number of H_2 adsorption sites blocked by H_2S increases with

increasing H_2S concentration. In addition to blocking H_2 adsorption sites, H_2S also causes in irreversible change in the H_2-D_2 exchange activity of $Pd_{47}Cu_{53}$. It is possible that H_2S causes the formation of surface sulfides that have an intrinsically lower H_2-D_2 exchange activity than the clean $Pd_{47}Cu_{53}$ surface.

5.4.3. H_2-D_2 exchange over $Pd_{70}Cu_{30}$ in the presence of H_2S

H_2-D_2 exchange over $Pd_{70}Cu_{30}$ was carried out similar to that over Pd_4S and $Pd_{47}Cu_{53}$, with H_2S concentrations in the feed gas varying from 50 to 2000 ppm. Unlike the $Pd_{47}Cu_{53}$ alloy, the crystal structure of the $Pd_{70}Cu_{30}$ alloy (see Figure 5.5) is FCC in the entire temperature range of the H_2-D_2 exchange reaction (400 to 1000 K). A comparison of the HD flow rates exiting a $Pd_{70}Cu_{30}$ foil catalyst without H_2S in the feed gas to the HD flow rates exiting a $Pd_{70}Cu_{30}$ foil catalyst bed with 50 ppm H_2S in feed gas, each with 9 mL/min of H_2 and D_2 in the feed gas, is shown in Figure 5.11. Adding 50 ppm H_2S to the feed gas significantly reduces the H_2-D_2 exchange activity of $Pd_{70}Cu_{30}$.

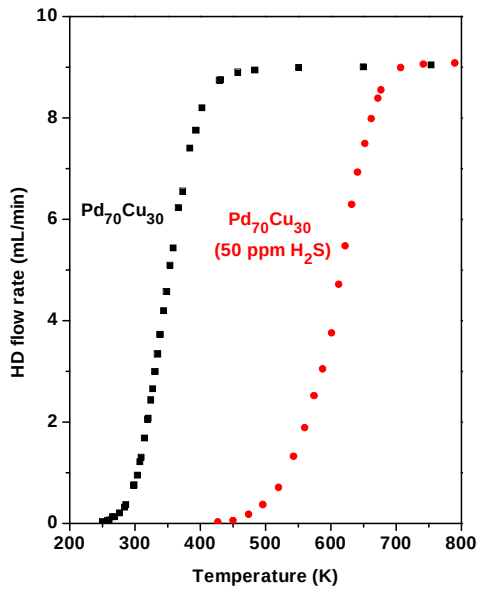

Figure 5.11 Comparison of the HD flow rates exiting the $Pd_{70}Cu_{30}$ catalyst bed without H_2S in the feed gas to the HD flow rates exiting the $Pd_{70}Cu_{30}$ catalyst bed with 50 ppm H_2S in the feed gas, each with 9 mL/min of H_2 and D_2 in the feed gas. The rate of HD production over $Pd_{70}Cu_{30}$ is significantly reduced by adding 50 ppm H_2S to the feed gas.

To determine whether H_2S decreases the rate of HD production over $Pd_{70}Cu_{30}$ by decreasing the rate of H_2 adsorption, we first had to determine whether the rate of H_2-D_2 exchange over $Pd_{70}Cu_{30}$ is limited by the rate of H_2 adsorption. Figure 5.12 shows the HD flow rates exiting the (a) $Pd_{70}Cu_{30}$ foil catalyst bed without H_2S in the feed gas and (b) the $Pd_{70}Cu_{30}$ foil catalyst bed with 50 ppm H_2S in the feed gas, each with three different $H_2/D_2/Ar$ feed gas combinations. The HD flow rate exiting the $Pd_{70}Cu_{30}$ catalyst bed without H_2S in the feed gas is not reduced by diluting the feed gas with Ar and, therefore, HD

desorption is rate-limiting in the absence of H_2S. In the presence of 50 ppm H_2S, the rate of HD production over $Pd_{70}Cu_{30}$ is reduced by diluting the feed gas with Ar, indicating adsorption-limited H_2-D_2 exchange. Therefore, H_2S reduces the H_2-D_2 exchange activity of $Pd_{70}Cu_{30}$ by lowering the rate of H_2 adsorption.

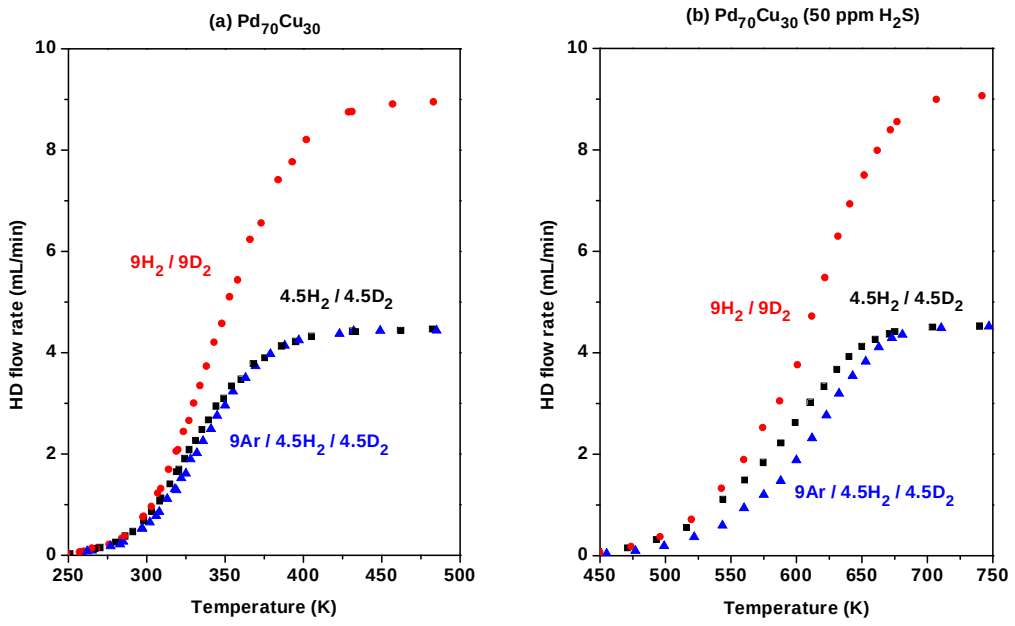

Figure 5.12 HD flow rates exiting the (a) $Pd_{47}Cu_{53}$ foil catalyst bed without H_2S in the feed gas and the (b) $Pd_{47}Cu_{53}$ foil catalyst bed with 50 ppm H_2S in the feed gas, each with 9 mL/min of H_2 and D_2 ($9H_2$ / $9D_2$), 4.5 mL/min of H_2 and D_2 ($4.5H_2$ / $4.5D_2$), and 4.5 mL/min of H_2 and D_2 diluted with 9 mL/min of Ar. Diluting the feed gas with Ar does not reduce the HD flow rate exiting the $Pd_{70}cu_{30}$ catalyst bed in the absence of H_2S, indicating desorption-limited H_2-D_2 exchange. In contrast, the HD flow rate exiting the $Pd_{70}Cu_{30}$ catalyst bed in the presence of 50 ppm H_2S is reduced by diluting the feed gas with Ar, indicating adsorption-limited H_2-D_2 exchange. H_2S reduces the H_2-D_2 exchange activity of $Pd_{70}Cu_{30}$ by reducing the rate of H_2 adsorption.

H_2-D_2 exchange over $Pd_{70}Cu_{30}$ was performed with H_2S concentrations in the feed gas varying from 50 to 2000 ppm to determine whether increasing the H_2S concentration would decrease the rate of H_2 adsorption on $Pd_{70}Cu_{30}$. Figure 5.13 shows the HD flow rates exiting the $Pd_{70}Cu_{30}$ foil catalyst bed with H_2S concentrations of 50, 100, 200, 500, 1000, and 2000 ppm and with (a) 4.5 mL/min of H_2 and D_2, (b) 9 mL/min of H_2 and D_2, and (c) 4.5 mL/min of H_2 and D_2 diluted with 9 mL/min of Ar. Increasing the H_2S concentration in the feed gas decreases the rate of HD production over $Pd_{70}Cu_{30}$. It is likely that H_2S decreases the rate of H_2 adsorption on $Pd_{70}Cu_{30}$ by blocking H_2 adsorption sites and the number of sites blocked increases with H_2S concentration in the feed gas.

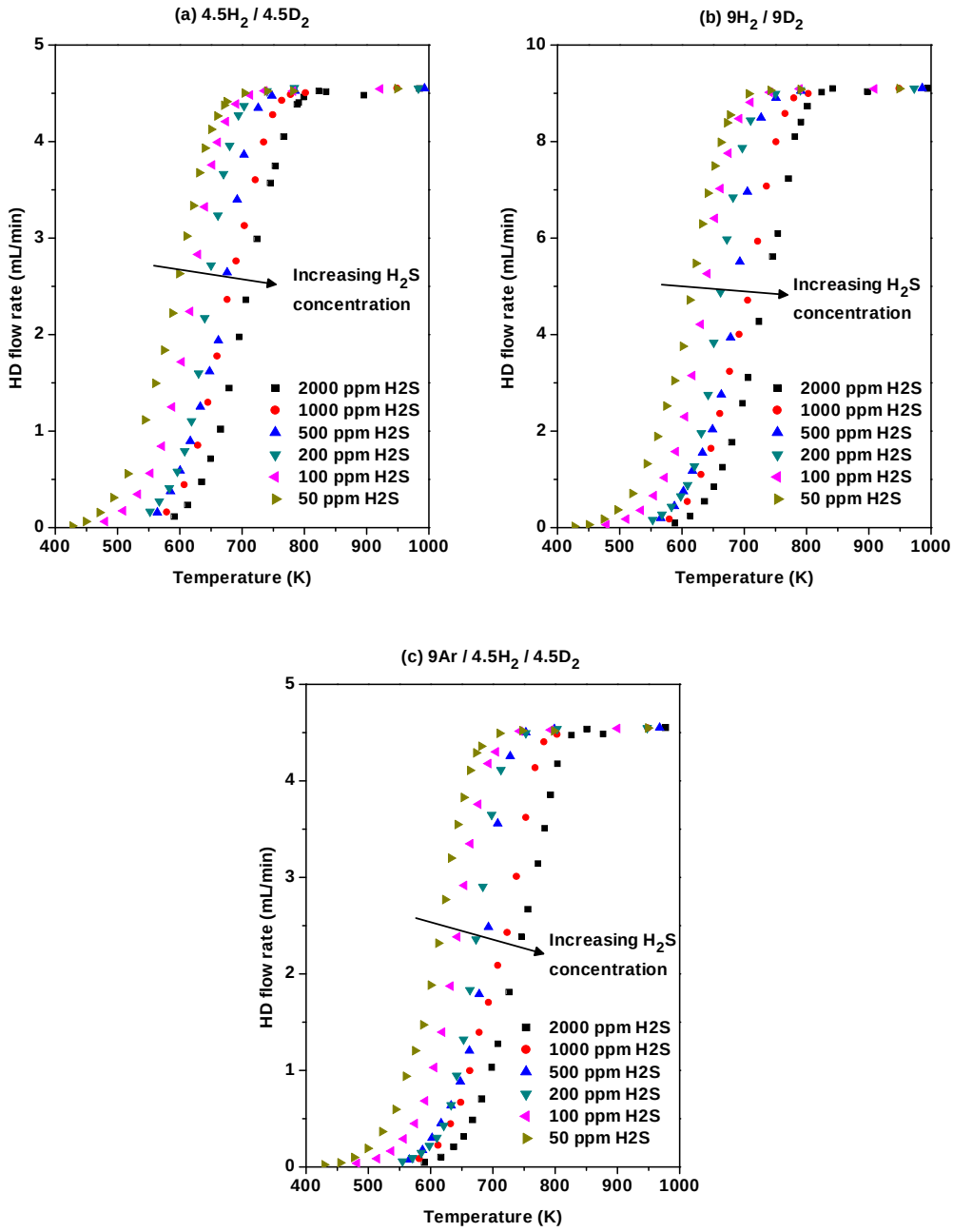

Figure 5.13 HD flow rates exiting a $Pd_{70}Cu_{30}$ catalyst bed with (a) 4.5 mL/min each of H_2 and D_2 in the feed gas, (b) 9 mL/min each of H_2 and D_2 in the feed gas, and (c) 9 mL/min of Ar with 4.5 mL/min each of H_2 and D_2 in the feed gas, each with H_2S concentrations in the feed gas of 2000, 1000, 500, 200, 100, and 50 ppm. Increasing the H_2S concentration in the feed gas decreases the rate of H_2-D_2 exchange over $Pd_{70}Cu_{30}$ with all three $H_2/D_2/Ar$ feed gas combinations.

5.4.4 Comparison of H_2-D_2 exchange over Pd_4S, $Pd_{47}Cu_{53}$, and $Pd_{70}Cu_{30}$ in the presence of H_2S

A comparison of the HD flow rates exiting the Pd_4S, $Pd_{47}Cu_{53}$, and $Pd_{70}Cu_{30}$ foil catalyst beds with (a) 50 ppm H_2S in the feed gas and with (b) 2000 ppm H_2S in the feed gas is shown in Figure 5.14. With both 50 ppm and 2000 ppm H_2S in the feed gas, the rate of HD production over Pd_4S is the highest followed by $Pd_{70}Cu_{30}$ and $Pd_{47}Cu_{53}$. This result also implies that, in the 50 to 2000 ppm H_2S range, the rate of H_2 dissociative adsorption is the highest on Pd_4S followed by $Pd_{70}Cu_{30}$ and $Pd_{47}Cu_{53}$. We have not investigated a wide enough range of PdCu alloy compositions to make a general comment about the effect of alloying Pd and Cu on the rate of H_2 adsorption; however, in the presence of H_2S, the rate of H_2 adsorption on the catalysts in this study decreases with increasing Cu content in the alloy.

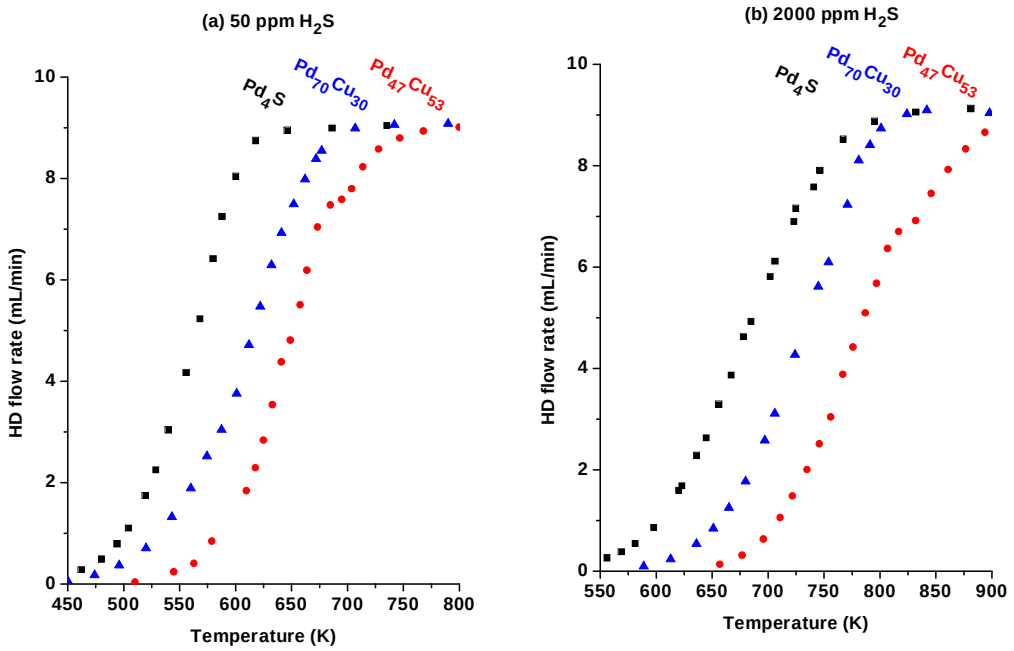

Figure 5.14 Comparison of the HD flow rates exiting Pd_4S, $Pd_{70}Cu_{30}$, and $Pd_{47}Cu_{53}$ foil catalyst beds with (a) 50 ppm H_2S in the feed gas and (b) 2000 ppm H_2S in the feed gas, each with 9 mL/min of H_2 and D_2 in the feed gas. In the 50 to 2000 ppm H_2S range, the rate of HD production over Pd_4S is the highest followed by $Pd_{70}Cu_{30}$ and $Pd_{47}Cu_{53}$.

5.5 Conclusions

In this chapter, the effect of H_2S on H_2-D_2 exchange over Pd_4S, $Pd_{70}Cu_{30}$, and $Pd_{47}Cu_{53}$ was investigated. The results of this investigation were qualitatively the same for all three catalysts. Adding 50 ppm H_2S to the $H_2/D_2/Ar$ feed gas reduced the rate of HD production, relative to the HD production rate in the absence of H_2S, by reducing the rate of H_2 adsorption. Increasing the H_2S concentration in the feed gas up to 2000 ppm decreased the rate of HD production further by decreasing the rate of H_2 dissociative adsorption. It is not clear how H_2S decreases the rate of H_2 adsorption, but it is possible that H_2S, or other sulfur species such as SH or S, blocks H_2 dissociation sites. The rate of H_2-D_2 exchange over Pd_4S was the highest of the catalysts in this study followed by $Pd_{70}Cu_{30}$ and $Pd_{47}Cu_{53}$. Our results show that there may be a link between increasing Cu content in PdCu alloys and reduced H_2 dissociation activity in the presence of H_2S.

Chapter 6

Surface Modification and Sulfidation of $Pd_{47}Cu_{53}$

6.1. Summary and introduction

Previous work at the National Energy Technology Laboratory (B.D. Morreale, Ph.D. thesis, University of Pittsburgh, 2006) linked the presence of small particles of Ni-, Cr-, and Fe-sulfides (contaminants from stainless steel fixtures) on the surface of PdCu alloys to improved sulfur tolerance. We hypothesized that these Ni-, Cr-, and Fe-sulfide particles improve the sulfur tolerance of PdCu alloys by acting as sulfur tolerant H_2 dissociation catalysts. This hypothesis was tested in this thesis by modifying the surfaces of $Pd_{47}Cu_{53}$ alloys with thin (~1 monolayer to 1 μm) films of Ni, Cr, Fe, Co, Mo, Pt, and Pd and measuring the rate of H_2 permeation through the modified $Pd_{47}Cu_{53}$ alloys in the presence of 1000 ppm H_2S. These thin films did not improve the sulfur tolerance of the $Pd_{47}Cu_{53}$ alloy; however, monolayer films of Ni, Cr, Fe, Co, Mo, and Pt unexpectedly catalyzed the corrosion of the $Pd_{47}Cu_{53}$ alloy to $Pd_{13}Cu_3S_7$ and Cu_2S. Our results show that the $Pd_{47}Cu_{53}$ alloy is not thermodynamically corrosion resistant, and its corrosion is kinetically limited by a surface reaction that is catalyzed by small amounts of other metals including Mo, Ni, Co, Fe, Pt, and Cr.

6.2 Experimental

$Pd_{47}Cu_{53}$ surfaces were modified by depositing Mo, Fe, Ni, Co, Cr, Pd, and Pt thin films onto their surfaces. Membrane samples were cut from 25 µm thick $Pd_{47}Cu_{53}$ foils (ATI Wah Chang, 99.0% metals purity). Thin film deposition was performed in an ultra-high vacuum system equipped with a magnetron sputter source (1.3" MAK sputter gun, MeiVac, Inc.). Mo, Fe, Ni, Co, Cr, Pd, and Pt sputtering targets were purchased from ACI Alloys Inc. and were all 99.9% metals purity. Prior to deposition, the substrate surfaces were cleaned by Ar^+ etching. Deposition was performed at constant power (25 W) with a background Ar pressure of 3 mTorr. Film thicknesses were monitored during deposition with a quartz crystal microbalance (Maxtek BSH-150) positioned next to the $Pd_{47}Cu_{53}$ foil and the composition of the film was verified following deposition by analysis with Auger electron spectroscopy (LK Technologies EG3000 electron gun and MINICMA™ electron energy analyzer). Following preparation of the modified $Pd_{47}Cu_{53}$ foil, the vacuum chamber was vented to atmospheric pressure and the membrane foil was mounted in the membrane testing apparatus.

The procedure for making hydrogen permeation measurements, and for characterizing the membrane samples by x-ray diffraction, scanning electron microscopy, and x-ray photoelectron spectroscopy, is given in Chapter 3.

6.3 Results and discussion

$Pd_{47}Cu_{53}$ membrane surfaces were modified by thin films of Fe, Ni, Cr, Co, Mo, Pt, and Pd with thicknesses ranging from ~1 monolayer to 1 µm. Their performance in the membrane testing apparatus was then evaluated by measuring the rate of H_2 permeation through the membranes in the presence of 1000 ppm H_2S. Except for at the very beginning of H_2S exposure, the sulfur tolerance of all of the surface-modified $Pd_{47}Cu_{53}$ membranes was not significantly better than the unmodified $Pd_{47}Cu_{53}$ membrane. Figure 6.1 shows the H_2 fluxes through Pd, unmodified $Pd_{47}Cu_{53}$, $Pd_{47}Cu_{53}$ with a 1 ML Mo film on the surface (1ML Mo / $Pd_{47}Cu_{53}$), and $Pd_{47}Cu_{53}$ with a 1 µm Pd film (1µmPd / $Pd_{47}Cu_{53}$) during exposure to 1000 ppm H_2S at 623 K. The H_2 flux through the unmodified $Pd_{47}Cu_{53}$ membrane decays to zero in less than 5 minutes of H_2S exposure, whereas the Pd membrane is still permeable to H_2 after 6 hours of H_2S exposure. The H_2 flux through the $Pd_{47}Cu_{53}$ membrane with a 1 monolayer Mo film on the surface decays to zero about 20 minutes after H_2S exposure, which is not a significant improvement over the unmodified $Pd_{47}Cu_{53}$ membrane. The sulfur tolerance of the $Pd_{47}Cu_{53}$ membrane with a 1 µm Pd film is significantly better than the unmodified $Pd_{47}Cu_{53}$ at the beginning of H_2S exposure, but the H_2 flux through the 1µmPd / $Pd_{47}Cu_{53}$ membrane decays to zero after about 6 hours of H_2S exposure. Therefore, the sulfur tolerance of the modified $Pd_{47}Cu_{53}$ membranes was not significantly better than the unmodified $Pd_{47}Cu_{53}$ membranes after 6 hours of H_2S exposure and the modified $Pd_{47}Cu_{53}$ membranes did not have better sulfur tolerance than pure Pd.

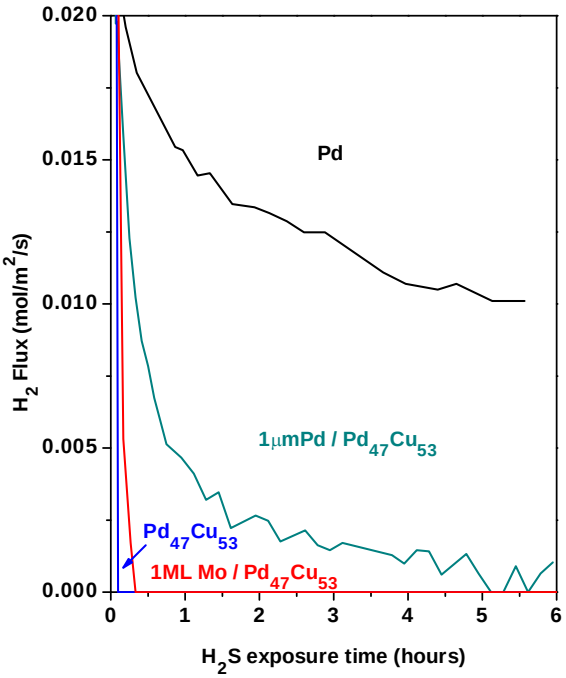

Figure 6.1 H_2 fluxes through Pd, $Pd_{47}Cu_{53}$, $Pd_{47}Cu_{53}$ with a 1 µm Pd film on the surface (1µmPd / $Pd_{47}Cu_{53}$), and $Pd_{47}Cu_{53}$ with a 1 monolayer Mo film on the surface (1ML Mo / $Pd_{47}Cu_{53}$) during exposure to 1000 ppm H_2S at 623 K.

Although modifiying the surface of $Pd_{47}Cu_{53}$ with thin metal films did not significantly improve the sulfur tolerance of the alloy, there was a significant and unexpected difference in the interaction of H_2S with the unmodified and the modified $Pd_{47}Cu_{53}$ alloy. Figure 6.2 shows the x-ray diffraction patterns of a clean $Pd_{47}Cu_{53}$ foil, a $Pd_{47}Cu_{53}$ foil after 6 hours of exposure to 1000 ppm H_2S at 623 K, and a $Pd_{47}Cu_{53}$ foil with a monolayer Mo film on the surface (1 ML Mo / $Pd_{47}Cu_{53}$) after 6 hours of exposure to 1000 ppm H_2S at 623 K. The peak

positions in the diffraction patterns of the clean $Pd_{47}Cu_{53}$ foil and the $Pd_{47}Cu_{53}$ foil after 6 hours of exposure to 1000 ppm H_2S are nearly identical, indicating that the $Pd_{47}Cu_{53}$ alloy resisted bulk sulfidation by H_2S. There are additional peaks in the diffraction pattern of the 1 ML Mo / $Pd_{47}Cu_{53}$ foil exposed to H_2S that are not present in the diffraction pattern of the unmodified $Pd_{47}Cu_{53}$ exposed to H_2S; these peaks are associated with two different sulfide compounds: $Pd_{13}Cu_3S_7$ and Cu_2S. These results suggest that the monolayer film of Mo catalyzed the corrosion of $Pd_{47}Cu_{53}$ to $Pd_{13}Cu_3S_7$ and Cu_2S.

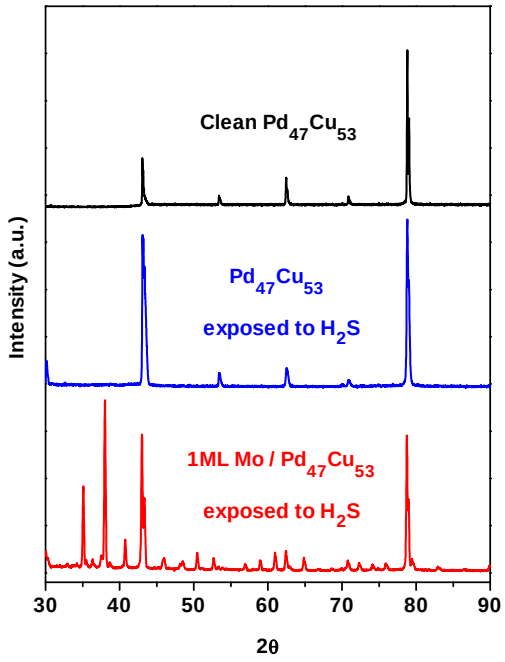

Figure 6.2 X-ray diffraction (XRD) patterns of a clean $Pd_{47}Cu_{53}$ foil, a $Pd_{47}Cu_{53}$ foil after 6 hours of exposure to 1000 ppm H_2S at 623 K, and a $Pd_{47}Cu_{53}$ foil with a monolayer Mo film on the surface (1ML Mo / $Pd_{47}Cu_{53}$) after 6 hours of exposure to 1000 ppm H_2S at 623 K. The monolayer Mo film catalyzed the corrosion of $Pd_{47}Cu_{53}$ to $Pd_{13}Cu_3S_7$ and Cu_2S.

Monolayer films of Fe, Cr, Ni, Co, and Pt also catalyzed the corrosion of $Pd_{47}Cu_{53}$ to $Pd_{13}Cu_3S$. The observation that monolayer-thick metal films catalyze the corrosion of $Pd_{47}Cu_{53}$ indicates that the $Pd_{47}Cu_{53}$ alloy is not thermodynamically corrosion resistant. Corrosion of $Pd_{47}Cu_{53}$ must be kinetically limited by a surface reaction that is catalyzed by the thin metal films. There are several possible surface reactions that must take place for $Pd_{47}Cu_{53}$ to corrode to $Pd_{13}Cu_3S_7$ and Cu_2S. First, H_2S must dissociate on the $Pd_{47}Cu_{53}$ surface to S.

Then diffusion of S from the surface to the subsurface must take place to form bulk $Pd_{13}Cu_3S_7$ and Cu_2S. Either of these surface reactions may be catalyzed by the thin metal films. However, we have evidence that H_2S dissociates readily on the unmodified $Pd_{47}Cu_{53}$ surface. During H_2-D_2 exchange over $Pd_{47}Cu_{53}$ in the presence of 1000 ppm H_2S (Chapter 5), there was a significant amount of HDS and D_2S in the product gas, indicating that H_2S dissociates on the $Pd_{47}Cu_{53}$ surface and reacts with D atoms. Therefore, it is likely that corrosion of $Pd_{47}Cu_{53}$ is not kinetically limited by the H_2S dissociation reaction and the thin metal films may instead catalyze the penetration of S into the $Pd_{47}Cu_{53}$ subsurface. It is possible that these thin metal films strain the surface and reduce the activation barrier to sulfur penetration into the $Pd_{47}Cu_{53}$ subsurface.

Monolayer-thick films of Mo, Fe, Cr, Ni, Co, and Pt catalyzed the corrosion of $Pd_{47}Cu_{53}$ to $Pd_{13}Cu_3S_7$ and Cu_2S. Thicker films of some these metals produced different corrosion products. In some cases, no detectable corrosion products were formed with thicker films. Table 6.1 lists the corrosion products that were detected by XRD after 1000 ppm H_2S exposure to $Pd_{47}Cu_{53}$ foils modified by Co, Cr, Fe, Mo, Ni, Pd, and Pt films with thicknesses varying from 1 monolayer to 1 μm. Co, Mo, and Pd films of 1 nm catalyzed the corrosion of $Pd_{47}Cu_{53}$ to $Pd_{13}Cu_3S_7$ and Cu_2S similarly to the monolayer-thick films of these metals. 10 nm and 100 nm Cr films on the $Pd_{47}Cu_{53}$ surface, however, did not catalyze the corrosion of $Pd_{47}Cu_{53}$ and no bulk sulfides were detected by XRD. 100 nm Co, Fe, and Ni films on the $Pd_{47}Cu_{53}$ surface did not catalyze the corrosion of $Pd_{47}Cu_{53}$, but Co-, Fe-, and Ni-sulfides were detected. Therefore,

monolayer films of Co, Cr, Fe, Mo, Ni, and Pt catalyzed the corrosion of $Pd_{47}Cu_{53}$ to $Pd_{13}Cu_3S_7$ and Cu_2S but thicker films of these metals did not always catalyze the corrosion of $Pd_{47}Cu_{53}$. It is not clear why the monolayer films are more effective at catalyzing the corrosion of $Pd_{47}Cu_{53}$. It is possible that the monolayer films create sufficient strain in the $Pd_{47}Cu_{53}$ surface to allow penetration of S into the subsurface, but thicker films of these metals increase the resistance to diffusion of S into the $Pd_{47}Cu_{53}$ subsurface.

Table 6.1 Corrosion products that were detected by x-ray diffraction following exposure of modified $Pd_{47}Cu_{53}$ foils to 1000 ppm H_2S in H_2 at 623 K. $Pd_{47}Cu_{53}$ surfaces were modified by thin films of Co, Cr, Fe, Mo, Ni, Pd, and Pt with thicknesses ranging from 1 monolayer to 1 µm. Exposure of the 1 µm Pd film film (highlighted) to H_2S produced a corrosion product that has a crystal structure similar to Pd_4S, but with a significant amount of Cu incorporated into its lattice

	1 ML	1 nm	10 nm	100 nm	1 µm
Co	$Pd_{13}Cu_3S_7$ + Cu_2S	$Pd_{13}Cu_3S_7$ + Cu_2S		Co_9S_8	
Cr	$Pd_{13}Cu_3S_7$ + Cu_2S		no "thick" sulfides	no "thick" sulfides	
Fe	$Pd_{13}Cu_3S_7$ + Cu_2S			Fe-sulfide (spalled)	
Mo	$Pd_{13}Cu_3S_7$ + Cu_2S	$Pd_{13}Cu_3S_7$ + Cu_2S			
Ni	$Pd_{13}Cu_3S_7$ + Cu_2S			Ni-sulfide	
Pd		$Pd_{13}Cu_3S_7$ + Cu_2S	$Pd_{13}Cu_3S_7$ + Cu_2S	$Pd_{13}Cu_3S_7$ + Cu_2S	Pd_4S
Pt	$Pd_{13}Cu_3S_7$ + Cu_2S				

Pd films up to 100 nm catalyzed the corrosion of $Pd_{47}Cu_{53}$ to $Pd_{13}Cu_3S_7$ and Cu_2S; however, exposure of a $Pd_{47}Cu_{53}$ foil with a 1 µm Pd film to 1000 ppm H_2S at 623 K produced a corrosion product with a crystal structure that is similar to Pd_4S. Figure 6.3 shows the XRD patterns of a $Pd_{47}Cu_{53}$ foil with a 1 µm Pd film on the surface (1µmPd / $Pd_{47}Cu_{53}$) before H_2S exposure and after 6 hours of exposure to 1000 ppm H_2S in H_2 at 623 K. As expected, the diffraction pattern of the 1µmPd / $Pd_{47}Cu_{53}$ foil before H_2S exposure shows only peaks that are associated with Pd and $Pd_{47}Cu_{53}$. The diffraction pattern of the composite 1µmPd / $Pd_{47}Cu_{53}$ foil after 6 hours of H_2S exposure is dominated by features that are associated with the Pd_4S crystal structure and not the $Pd_{13}Cu_3S_7$ or Cu_2S crystal structures. Therefore, increasing the Pd film thickness from 100 nm to 1 µm increased the selectivity towards Pd_4S production relative to $Pd_{13}Cu_3S_7$ and Cu_2S.

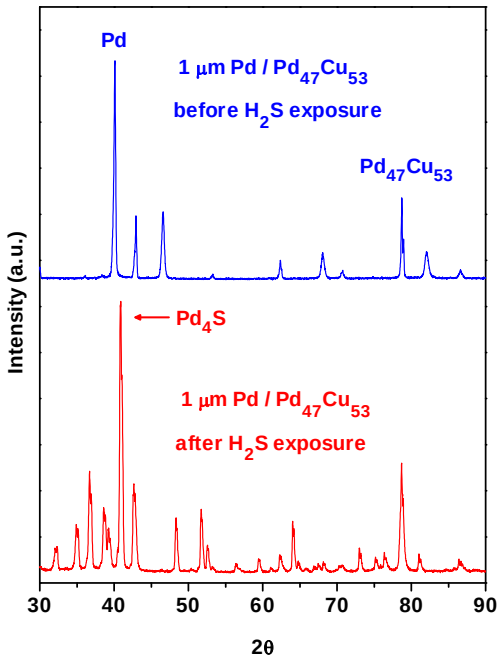

Figure 6.3 XRD patterns of a $Pd_{47}Cu_{53}$ foil with a 1 μm Pd film on the surface before H_2S exposure (top, blue) and after 6 hours of exposure to 1000 ppm H_2S at 623 K (bottom, red). Only peaks associated with Pd and $Pd_{47}Cu_{53}$ are present in the diffraction pattern of composite foil before H_2S exposure. Peaks associated with Pd_4S dominate the diffraction pattern of the Pd / $Pd_{47}Cu_{53}$ foil after 6 hours of H_2S exposure.

Although the crystal structure of the corrosion product that resulted from exposing the 1 μm Pd / $Pd_{47}Cu_{53}$ foil to H_2S is similar to Pd_4S, x-ray photoelectron spectroscopic depth profiling in the near surface region of the 1 μm Pd / $Pd_{47}Cu_{53}$ foil indicates that there was a significant amount of Cu incorporated into the Pd_4S lattice. Figure 6.4 shows an x-ray photoelectron spectroscopy depth profile of the 1 μm Pd / $Pd_{47}Cu_{53}$ foil after 6 hours of exposure to 1000 ppm H_2S

at 623 K. In the near-surface region (~200 nm) of the 1 μm Pd / $Pd_{47}Cu_{53}$, there is a significant amount of Cu, indicating that the thin Pd film extracted Cu from the $Pd_{47}Cu_{53}$ foil substrate during sulfidation. The metal (Pd + Cu)-to-S ratio in the near-surface region is still ~4:1, which is the Pd:S ratio in Pd_4S. Figure 6.5 shows a scanning electron micrograph (SEM) of a cross-section of the 1 μm Pd / $Pd_{47}Cu_{53}$ foil after 6 hours of exposure to 1000 ppm H_2S at 623 K with a sulfur EDS map to highlight the sulfur rich region in the SEM image. After 6 hours of H_2S exposure, the thickness of the sulfur corrosion product was ~4 μm, which is much thicker than the original thickness of the Pd film (1 μm) that was deposited onto the $Pd_{47}Cu_{53}$ foil. XRD, XPS depth profiling and SEM/EDS analysis of the sulfur-exposed 1 μm Pd / $Pd_{47}Cu_{53}$ foil indicate that the thin 1 μm Pd film extracted Cu from the $Pd_{47}Cu_{53}$ foil substrate during sulfidation to produce a corrosion product that has a crystal structure similar to that of Pd_4S but with a significant amount of Cu incorporated into the crystal lattice.

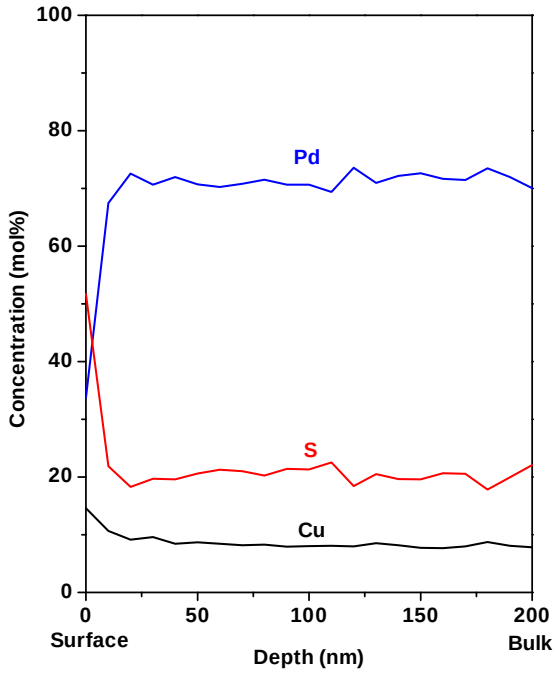

Figure 6.4 X-ray photoelectron spectroscopy depth profile of the $Pd_{47}Cu_{53}$ foil with a 1 µm Pd film on the surface after 6 hours of exposure to 1000 ppm H_2S in H_2 at 623 K showing the Pd, Cu, and S concentrations versus depth from the surface to about 200 nm into the bulk. There is a significant amount of Cu in the near surface region, indicating that the Pd film extracted Cu from the $Pd_{47}Cu_{53}$ foil during sulfidation.

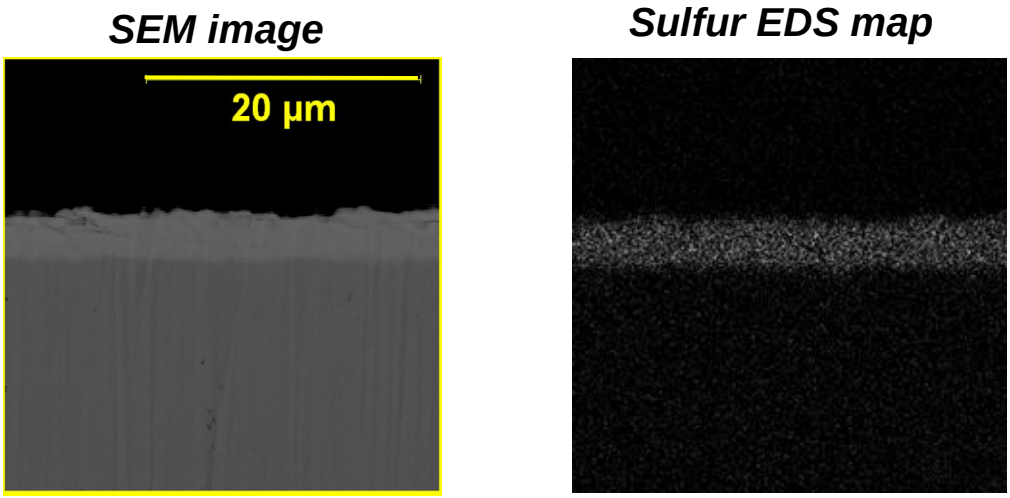

Figure 6.5 Scanning electron micrograph (left) with sulfur energy dispersive spectroscopy map (right) of a cross-section of the $Pd_{47}Cu_{53}$ foil with a 1 µm Pd film on the surface after 6 hours of exposure to 1000 ppm H_2S in H_2 at 623 K. The white region in the sulfur EDS map highlights the sulfur-rich region in the SEM image. The thickness of this sulfur-rich region is ~4 µm, which is much thicker than the original thickness of the Pd film (1 µm). XPS depth profiling (Figure 6.4) indicates that a significant amount of Cu is present in this sulfur-rich film, indicating that the Pd film extracts Cu from the $Pd_{47}Cu_{53}$ foil substrate during sulfidation.

6.4 Conclusions

In an attempt to impart sulfur tolerance in the $Pd_{47}Cu_{53}$ alloy at low temperatures, $Pd_{47}Cu_{53}$ surfaces were modified by thin films of Mo, Fe, Ni, Co, Cr, Pd and Pt with thicknesses ranging from 1 monolayer to 1 µm. Although the sulfur tolerance of the modified $Pd_{47}Cu_{53}$ alloys was not significantly better than the unmodified alloy, valuable insight into PdCu corrosion mechanisms was gained from these experiments. Monolayer-thick films of Mo, Fe, Ni, Co, Cr, and Pt catalyzed the corrosion of $Pd_{47}Cu_{53}$ to $Pd_{13}Cu_3S_7$ and Cu_2S, which suggests that the $Pd_{47}Cu_{53}$ alloy is not thermodynamically corrosion resistant. Corrosion of the $Pd_{47}Cu_{53}$ alloy is kinetically limited by a surface reaction that is catalyzed by these thin films. It is likely that these thin metal films aid sulfur penetration into the $Pd_{47}Cu_{53}$ bulk, perhaps by straining the $Pd_{47}Cu_{53}$ surface. Different corrosion products were formed by depositing thicker films on $Pd_{47}Cu_{53}$ foil surfaces. A 1 µm Pd film on the surface of a $Pd_{47}Cu_{53}$ foil extracted Cu from the $Pd_{47}Cu_{53}$ foil substrate during sulfidation to produce a ~4 µm-thick Pd-Cu-S corrosion product that had a crystal structure similar to that of Pd_4S but with a significant amount of Cu incorporated into the lattice.

Chapter 7

General Conclusions

The aim of this thesis was to understand how H_2S slows hydrogen transport through Pd and PdCu alloy hydrogen separation membranes. Although there are still many gaps in our understanding of sulfur poisoning, we have found that H_2S can inhibit hydrogen transport through Pd and PdCu membranes by two different mechanisms: (1) by producing a low permeability sulfide film on the membrane surface, and (2) by decreasing the rate of H_2 dissociation on the membrane surface.

Throughout this thesis we have used pure Pd and $Pd_{47}Cu_{53}$ as benchmarks for understanding hydrogen transport and sulfur poisoning mechanisms. The $Pd_{47}Cu_{53}$ alloy has been identified as a promising alternative to pure Pd hydrogen separation membranes due in part to its high permeability, which is related to its BCC crystal structure at temperatures less than ~700 K. At temperatures greater than ~800 K, the $Pd_{47}Cu_{53}$ alloy has a FCC crystal structure and a H_2 permeability that is about an order-of-magnitude less than that of BCC $Pd_{47}Cu_{53}$. We have shown for the first time that the surface H_2 dissociation reaction is also significantly different on BCC $Pd_{47}Cu_{53}$ than that on FCC Pd47Cu53; the activation barrier to H_2 dissociation on FCC $Pd_{47}Cu_{53}$ is significantly lower than that on BCC $Pd_{47}Cu_{53}$. In addition, the activation barriers to H_2 dissociation on both BCC and FCC $Pd_{47}Cu_{53}$ surfaces are not significantly higher than the

activation barrier to H_2 dissociation on pure Pd. This thesis has shown that, in the absence of H_2S, Pd can be alloyed with ~50 mol% Cu without significantly reducing H_2 dissociation rates on the surface or the rate of H atom permeation through its bulk.

There is a significant difference in the effect of H_2S on hydrogen transport through Pd and $Pd_{47}Cu_{53}$ membranes, which we believe is due to a difference in how H_2S interacts with the two membranes. At 623 K, the rate of hydrogen permeation through Pd and $Pd_{47}Cu_{53}$ membranes is significantly reduced by exposure to 1000 ppm H_2S, but with significantly different decay patterns. The $Pd_{47}Cu_{53}$ membrane is impermeable to H_2 in less than 5 minutes of H_2S exposure, whereas the Pd membrane is still permeable to hydrogen after 6 hours of H_2S exposure. Compositional analysis of the Pd and $Pd_{47}Cu_{53}$ membranes indicates that H_2S exposure produced a thick (~μm) Pd_4S film on the surface of the Pd membrane. In contrast, sulfur penetrated only a few nanometers into the bulk of the $Pd_{47}Cu_{53}$ membrane. These results have led us to believe that H_2S slows hydrogen transport through Pd and $Pd_{47}Cu_{53}$ membranes by different mechanisms.

H_2S slows hydrogen transport across Pd membranes mainly by producing a Pd_4S film on the Pd surface that is about an order-of-magnitude less permeable to hydrogen than Pd. In contrast to Pd, our results strongly suggest that H_2S blocks hydrogen transport across $Pd_{47}Cu_{53}$ membranes by decreasing the rate of H_2 dissociation on the $Pd_{47}Cu_{53}$ surface. The kinetics of H_2-D_2 exchange over $Pd_{47}Cu_{53}$ in the presence of H_2S (Chapter 5) need to be analyzed with a microkinetic model to understand how H_2S decreases the rate of H_2 dissociation

on the $Pd_{47}Cu_{53}$ surface; but it appears that H_2S (or other sulfur species) blocks a significant fraction of the $Pd_{47}Cu_{53}$ surface for H_2 dissociation. H_2S also decreases the rate of H_2 dissociation on Pd_4S surfaces, but H_2S has a more significant effect on the rate of H_2 dissociation on $Pd_{47}Cu_{53}$ than on Pd_4S.

The effect of H_2S on hydrogen transport across $Pd_{47}Cu_{53}$ diminishes with increasing temperature until H_2S has no effect on hydrogen permeation through $Pd_{47}Cu_{53}$ at temperatures greater than ~900 K. It is likely that the sulfur tolerance exhibited by the $Pd_{47}Cu_{53}$ alloy is related to its resistance to bulk sulfidation. However, it is not well understood why the $Pd_{47}Cu_{53}$ alloy resist bulk sulfidation. Our results indicate that the $Pd_{47}Cu_{53}$ alloy is not thermodynamically sulfidation resistant; its sulfidation is kinetically limited by a surface reaction that is catalyzed by thin metal (Fe, Ni, Co, Cr, Mo, Pt) films on the surface of $Pd_{47}Cu_{53}$. This finding warrants further investigation because understanding why the $Pd_{47}Cu_{53}$ alloy resists bulk sulfidation may lead to the development of advanced membrane materials that could be implemented into a coal gasification process.

Appendix: derivation of the H_2-D_2 exchange kinetic model

The integral mass balance on HD is

$$\int_0^{F_{\mathrm{HD,out}}} \frac{dF_{\mathrm{HD}}}{r_{\mathrm{HD}}} = A, \tag{A1}$$

where dF_{HD} is the differential HD flow rate, $F_{\mathrm{HD,out}}$ is the HD flow rate exiting the catalyst bed, A is the catalyst surface area, and r_{HD} is the HD production rate [90]. The HD production rate, r_{HD}, is given by the microkinetic expression:

$$r_{\mathrm{HD}} = 2k_{\mathrm{des}}\theta_{\mathrm{H}}\theta_{\mathrm{D}} - k_{\mathrm{ads}}P_{\mathrm{HD}}\left(1-\theta_{\mathrm{H}}-\theta_{\mathrm{D}}\right)^2 \tag{A2}$$

where k_{des} is the HD desorption rate constant, θ_H is the coverage of H atoms, θ_D is the coverage of D atoms, k_{ads} is the HD adsorption rate constant, and P_{HD} is the HD partial pressure. Because we are assuming that isotopic effects are negligible, and the partial pressures of H_2 and D_2 are equal for all experiments, the coverages of H (θ_{H}) and D (θ_{H}) atoms are each assumed to be equal to one-half of the total coverage (θ):

$$\theta_H = \theta_D = \frac{\theta}{2}.$$

Therefore, the microkinetic expression for the rate of HD production is:

$$r_{\mathrm{HD}} = 2k_{\mathrm{des}}\left(\frac{\theta}{2}\right)^2 - k_{\mathrm{ads}}P_{\mathrm{HD}}\left(1-\theta\right)^2. \tag{A3}$$

To substitute the microkinetic expression for the rate of HD production, equation (A3), into the mass balance on HD, equation (A1), the HD partial pressure in equation (A3) must be converted into HD flow rate, F_{HD}:

$$r_{HD} = 2k_{des}\left(\frac{\theta}{2}\right)^2 - \frac{k_{ads}F_{HD}P_{total}\left(1-\theta\right)^2}{F_{total}} \tag{A4}$$

where

$$F_{\mathrm{HD}} = \frac{F_{\mathrm{total}} P_{\mathrm{HD}}}{P_{\mathrm{total}}}$$

and P_{total} is the total pressure and F_{total} is the total flow rate. Substituting the HD production rate, equation (A4), into the integral mass balance on HD, equation (A1), gives:

$$\int_0^{F_{HD,out}} \frac{dF_{HD}}{2k_{des}\left(\frac{\theta}{2}\right)^2 - \frac{k_{ads} F_{HD} P_{total} (1-\theta)^2}{F_{total}}} = A \qquad \text{(A5)}$$

Integrating equation (A5) and solving for the flow rate of HD exiting the catalyst bed gives:

$$F_{\mathrm{HD,out}} = \frac{k_{\mathrm{des}} F_{\mathrm{total}} \theta^2}{2k_{\mathrm{ads}} P (1-\theta)^2}\left[1 - \exp\left(\frac{-k_{\mathrm{ads}} PA (1-\theta)^2}{F_{\mathrm{total}}}\right)\right] \qquad \text{(A6)}$$

At steady-state, the change in the coverage of H (and D) atoms is zero:

$$\frac{d\theta_H}{dt} = 0 = 2k_{ads} P_{H2} (1-\theta_H-\theta_D)^2 + k_{ads} P_{HD} (1-\theta_H-\theta_D)^2 - 2k_{des}\theta_H^2 - 2k_{des}\theta_H\theta_D$$

where P_{H2} is the H_2 partial pressure and all of the other variables are defined above. Again, we assume that the coverages of H and D atoms are each equal to one-half of the total coverage:

$$\theta_H = \theta_H = \frac{\theta}{2}$$

Therefore, the change in the coverage of H atoms is given by:

$$\frac{d\theta_H}{dt} = 0 = 2k_{ads} P_{H2} (1-\theta)^2 + k_{ads} P_{HD} (1-\theta)^2 - k_{des}\theta^2 .$$

Solving for θ gives:

$$\theta = \frac{\sqrt{2\frac{k_{ads}}{k_{des}}P_{H2,\,feed}}}{1+\sqrt{2\frac{k_{ads}}{k_{des}}P_{H2,\,feed}}} \tag{A7}$$

where $P_{H2,feed}$ is the partial pressure of H_2 in the feed gas, which is related to P_{H2} and P_{HD} by the stoichiometry of the reaction:

$$P_{H2} = P_{H2,\,feed} - \frac{1}{2}P_{HD}$$

Substitution of the expression for the total coverage of H and D atoms, equation (A7), into the expression for the flow rate of HD exiting the reactor, equation (A6), gives the H_2-D_2 exchange kinetic model:

$$F_{HD,out} = F_{H_2,\,feed}\left[1-\exp\left(\frac{-k_{ads}P_{total}A}{F_{total}\left(1+\sqrt{2\frac{k_{ads}}{k_{des}}P_{H_2,\,feed}}\right)^2}\right)\right]$$

where

$$F_{H_2,\,feed} = \frac{F_{total}P_{H_2,\,feed}}{P_{total}}\,.$$

References

[1] C.P. O'Brien, B.H. Howard, J.B. Miller, B.D. Morreale, A.J. Gellman, Inhibition of hydrogen transport through Pd and $Pd_{47}Cu_{53}$ membranes by H_2S at 350 C, J. Membr. Sci., 349 (2010) 380-384.

[2] C.P. O'Brien, A.J. Gellman, B.D. Morreale, J.B. Miller, The hydrogen permeability of Pd_4S, Journal of Membrane Science, 371 (2011) 263-267.

[3] U.S.E.I. Administration, Annual Energy Outlook 2011 Early Release Overview, in, 2011.

[4] U.S.E.I. Administration, Annual Energy Review 2009, (2009).

[5] S. Sircar, T.C. Golden, Purification of hydrogen by pressure swing adsorption, Sep. Sci. Technol., 35 (2000) 667-687.

[6] S. Adhikari, Hydrogen Membrane Separation Techniques, Ind. Eng. Chem. Res., 45 (2006) 875-881.

[7] P. Kamakoti, B.D. Morreale, M.V. Ciocco, B.H. Howard, R.P. Killmeyer, A.V. Cugini, D.S. Sholl Prediction of Hydrogen Flux Through Sulfur-Tolerant Binary Alloy Membranes, Science, 307 (2005) 569-573.

[8] B.D. Morreale, M.V. Ciocco, R.M. Enick, B.I. Morsi, B.H. Howard, A.V. Cugini, K.S. Rothenberger, The permeability of hydrogen in bulk palladium at elevated temperatures and pressures, J. Membr. Sci., 212 (2003) 87-92.

[9] B.D. Morreale, The Influence of H_2S on Palladium and Palladium-Copper Alloy Membranes, in: Chemical Engineering, University of Pittsburgh, 2006.

[10] B.H. Howard, R.P Killmeyer, K.S. Rothenberger, A.V. Cugini, B.D. Morreale, R.M. Enick, F. Bustamante, Hydrogen Permeance of Palladium-Copper Alloy Membranes Over a Wide Range of Temperatures and Pressures J. Membr. Sci., 241 (2004) 207-218.

[11] M.V.C. Bryan D. Morreale, Robert M. Enick, Badi I. Morsi, Bret H. Howard, Anthony V. Cugini, Kurt S. Rothenberger, The Permeability of Hydrogen in Bulk Palladium at Elevated Temperatures and Pressures, Journal of Membrane Science, 212 (2003) 87-97.

[12] U. Muschiol, P.K. Schmidt, K. Christman, Adsorption and absorption of hydrogen on a palladium (210) surface: a combined LEED, TDS, $\Delta\phi$ and HREELS study, Surface Science, 395 (1998) 182-204.

[13] M.G. Cattania, V. Penka, R.J. Behm, K. Christmann, G. Ertl, Interaction of hydrogen with a palladium (110) surface, Surface Science, 126 (1983) 382-391.

[14] A. Lozano, A. Gross, H.F. Busnengo, Molecular dynamics of H_2 dissociation on H-covered Pd(100), Physical Review B, 81 (2010) 121402(R).

[15] W.M. Bartczak, J. Stawowska, Interaction of dihydrogen with transition metal (Pd, Ni, Ag, Cu) clusters, Structural Chemistry, 15 (2004) 447-459.

[16] W. Dong, G. Kresse, J. Hafner, Dissociative adsorption of H_2 on the Pd(111) surface, Journal of Molecular Catalysis A-Chemical, 119 (1997) 69-76.

[17] S.A. Steward, Review of Hydrogen Isotope Permeability through Materials, in: U.S.D.o. Energy (Ed.), Lawrence Livermore National Laboratory, 1983, pp. 1-21.

[18] D.L. McKinley, Metal alloy for hydrogen separation and purification, in: U.S.A. Patent 3,350,845 (1967).

[19] B.D. Morreale, M.V. Ciocco, B.H. Howard, R.P. Killmeyer, A.V. Cugini, R.M. Enick Effect of Hydrogen-Sulfide on the Hydrogen Permeance of Palladium-Copper Alloys at Elevated Temperatures, J. Membr. Sci., 241 (2004) 219-224.

[20] A.B. Antoniazzi, A.A. Haasz, P.C. Stangeby, The effect of adsorbed carbon and sulphur on hydrogen permeation through palladium, Journal of Nuclear Materials, 162-164 (1989) 1065-`1070.

[21] O. Iyoha, R. Enick, R. Killmeyer, B. Howard, M. Ciocco, B. Morreale, H_2 production from simulated coal syngas containing H_2S in multi-tubular Pd and 80wt% Pd-20wt% Cu membrane reactors at 1173 K, J. Membr. Sci., 306 (2007) 103-115.

[22] A. Kulprathipanja, G.O. Alptekin, J.L. Falconer, J.D. Way, Pd and Pd-Cu Membranes: Inhibition of H_2 Permeation by H_2S, J. Membr. Sci., 254 (2005) 49-62.

[23] R.C. Hurlbert, J.O. Konecny, Diffusion of Hydrogen through Palladium, The Journal of Chemical Physics, 34 (1961) 655-658.

[24] C.H. Chen, Y.H. Ma, The effect of H_2S on the performance of Pd and Pd/Au composite membrane, Journal of Membrane Science, 362 (2010) 535-544.

[25] B.D. Morreale, B.H. Howard, O. Iyoha, R.M. Enick, C. Ling, D.S. Sholl, Experimental and Computational Prediction of the Hydrogen Transport Properties of Pd_4S, Ind. Eng. Chem. Res., 46 (2007) 6313-6319.

[26] M. Kajiwara, Hydrogen permeation properties through composite membranes of platinum supported on porous alumina, Catalysis Today, 56 (2000) 65-73.

[27] S. Wilke, Poisoning of Pd(100) for the dissociation of H_2: a theoretical study of co-adsorption of hydrogen and sulphur, Surface Science, 329 (1995) L605-L610.

[28] S. Wilke, Mechanism of Poisoning the Catalytic Activity of Pd(100) by a Sulfur Adlayer, Physical Review Letters, 76 (1996) 4.

[29] O. Iyoha, R. Enick, R. Killmeyer, B. Morreale, The influence of hydrogen sulfide-to-hydrogen partial pressure ratio on the sulfidization of Pd and 70 mol% Pd-Cu membranes, Journal of Membrane Science, 305 (2007) 77-92.

[30] O.U. Iyoha, H_2 Production in Palladium & Palladium-Copper Membrane Reactors at 1173 K in the Presence of H_2S, in: Chemical Engineering, University of Pittsburgh, Pittsburgh, 2007.

[31] D.L. McKinley, Method for hydrogen separation and purification, in: U.S.A. Patent 3,439,474 (1969).

[32] S.M. Opalka, W. Huang, D. Wang, T.B. Flanagan, O.M. Lovvik, S.C. Emerson, Y. She, T.H. Vanderspurt, Hydrogen interactions with the PdCu ordered B2 alloy, J. Alloys Compd., 446-447 (2007).

[33] J.Y. Yang, C. Nishimura, M. Komaki Effect of H_2S on Hydrogen Permeation of $Pd_{60}Cu_{40}$/V-15Ni Composite Membrane, J. Alloys Compd., 446-447 (2007).

[34] J.Y. Yang, C. Nishimura, M. Komaki Hydrogen permeation of $Pd_{60}Cu_{40}$ alloy covered V-15Ni composite membrane in mixed gases containing H_2S, J. Membr. Sci., 309 (2008) 246-250.

[35] B.D. Cullity, Elements of X-ray Diffraction, Addison-Wesley, 1978.

[36] G. Ertl, J. Kuppers, Low Energy Electrons and Surface Chemistry, VCH 1985.

[37] A. Zubkov, T. Fujino, N. Sato, K. Yamada, Enthalpies of formation of the palladium sulphides, The Journal of Chemical Thermodynamics, 30 (1998) 571-581.

[38] D.L. McKinley, Metal alloy for hydrogen separation and purification, in, U.S.A., 1967.

[39] M.V. Mundschau, X. Xie, C.R. Evenson, A.F. Sammells Dense Inorganic Membranes for Production of Hydrogen from Methane and Coal with Carbon Dioxide Sequestration, Catal. Today, 118 (2006) 12-23.

[40] O. Iyoha, R. Enick, R. Killmeyer, B. Morreale, The influence of hydrogen sulfide-to-hydrogen partial pressure ratio on the sulfidization of Pd and 70 mol% Pd-Cu membranes, J. Membr. Sci., 305 (2007) 77-92.

[41] D.J. Edlund, Hydrogen-permeable metal membrane and method for producing the same, in: U.S.A. Patent 6,152,995 (2000), 2000.

[42] F. Roa, J.D. Way, R.L. McCormick, S.N. Paglieri, Preparation and Characterization of Pd-Cu Composite Membranes for Hydrogen Separation, Chem. Eng. J., 93 (2003) 11-22.

[43] L. Yuan, A. Goldbach, H. Xu, Segregation and H_2 Transport Rate Control in Body-Centered Cubic PdCu Membranes, J. Phys. Chem. B, 111 (2007) 10952-10958.

[44] S. Nam, Y. Seong, J.W. Lee, K. Lee, Preparation of highly stable palladium alloy composite membranes for hydrogen separation, Desalination, 236 (2009) 51-55.

[45] D.L. McKinley, Method for Hydrogen Separation and Purification, in, U.S.A., 1969.

[46] F. Roa, M.J. Block, J.D. Way, The influence of alloy composition on the H_2 flux of composite Pd-Cu membranes, Desalination, 147 (2002) 411-416.

[47] X. Zhang, W. Wang, J. Liu, S. Sheng, G. Xiong, W. Yang, Hydrogen transport through thin palladium-copper alloy composite membranes at low temperatures, Thin Solid Films, 516 (2008) 1849-1856.

[48] L. Yuan, A. Goldbach, H. Xu, Real-time monitoring of metal deposition and segregation phenomena during preparation of PdCu membranes, J. Membr. Sci., 322 (2008) 39-45.

[49] P.M. Thoen, F. Roa, J.D. Way, High flux palladium-copper composite membrane for hydrogen separations, Desalination, 193 (2006) 224-229.

[50] J.Y. Yang, C. Nishimura, M. Komaki Effect of overlayer composition on hydrogen permeation of Pd-Cu alloy coated V-15Ni composite membrane, J. Membr. Sci., 282 (2006) 337-341.

[51] P. Kamakoti, D.S. Sholl, A comparison of hydrogen diffusivities in Pd and CuPd alloys using density functional theory, J. Membr. Sci., 225 (2003) 145-154.

[52] P. Kamakoti, D.S. Sholl, Ab initio based lattice gas modeling of interstitial hydrogen diffusion in CuPd alloys, Phys. Rev. B, 71 (2005).

[53] S.K. Karode, S.S. Kulkarni, Analysis of transport through thin film composite membranes using an improved Wheatstone bridge resistance model, Journal of Membrane Science, 127 (1997) 131-140.

[54] H. Gaohong, H. Xiangyang, X. Renxian, Z. Baolin, An improved resistance model for gas permeation in composite membranes, Journal of Membrane Science, 118 (1996) 1-7.

[55] S.K. Karode, V.S. Patwardhan, S.S. Kulkarni, An improved model incorporating constriction resistance in transport through thin film composite membranes, Journal of Membrane Science, 114 (1996) 157-170.

[56] Y. Zhang, R. Maeda, M. Komaki, C. Nishimura, Hydrogen permeation and diffusion of metallic composite membranes, Journal of Membrane Science, 269 (2006) 60-65.

[57] W.D. Davis, Diffusion of gases through metals. I. Diffusion of gases through palladium, in: U.A.E. Commission (Ed.), 1954.

[58] Y.A. Balovnev, Diffusion of hydrogen in palladium, Russ. J. Phys. Chem., 48 (1974) 409-410.

[59] J.K. Gorman, W.R. Nardella, Hydrogen permeation through metals, Vacuum, 12 (1962) 19-24.

[60] F.A. Lewis, The Palladium-Hydrogen System, Academic Press, New York, 1967.

[61] H. Peisl, Hydrogen in Metals I, Springer-Verlag, Berlin, 1978.

[62] X. Pan, M. Kilgus, A. Goldbach, Low-temperature H_2 and N_2 transport through thin $Pd_{66}Cu_{34}H_x$ layers, Catalysis Today, 104 (2005) 225-230.

[63] Z.S. Wang, G.R. Darling, S. Holloway, The surface temperature dependence of the inelastic scattering and dissociation of hydrogen molecules from metal surfaces, Journal of Chemical Physics, 120 (2004) 2923-2933.

[64] B. Hammer, M. Scheffler, K.W. Jacobsen, J.K. Norskov, Multidimensional potential energy surface for H_2 dissociation over Cu(111), Physical Review Letters, 73 (1994) 1400-1403.

[65] C.T. Rettner, H.A. Michelsen, D.J. Auerbach, Quantum-state-specific dynamics of the dissociative adsorption and associative desorption at a Cu(111) surface, J. Chem. Phys., 102 (1995) 4625-4641.

[66] M.J. Murphy, A. Hodgson, Adsorption and desorption dynamics of H_2 and D_2 on Cu(111): The role of surface temperature and evidence for corrugation of the dissociation barrier, Journal of Chemical Physics, 108 (1998) 4199-4211.

[67] H.L. Abbott, I. Harrison, Microcanonical transition state theory for activated gas-surface reaction dynamics: application to H_2/Cu(111) with rotation as a spectator, J. Phys. Chem. A, 111 (2007) 9871-9883.

[68] J.M. Campbell, C.T. Campbell, The dissociative adsorption of H_2 and D_2 on Cu(110): activation barriers and dynamics, Surface Science, 259 (1991) 1-17.

[69] P.B. Rasmussen, P.M. Holmblad, H. Christoffersen, P.A. Taylor, I. Chorkendorff, Dissociative adsorption of hydrogen on Cu(100) at low temperatures, Surface Science, 287/288 (1994) 79-83.

[70] B.E. Hayden, C.L.A. Lamont, Vibrational and translational energy partition and the barrier to dissociative H_2 and D_2 adsorption on Cu(110), Surface Science, 243 (1991) 31-42.

[71] S. Sakong, G. Axel, Dissociative adsorption of hydrogen on strained Cu surfaces, Surface Science, 525 (2003) 107-118.

[72] B. Hammer, Electronic factors determining the reactivity of metal surfaces, Surface Science, 343 (1995) 211-220.

[73] Q. Sun, J. Xie, Z. Tao, Chemisorption of hydrogen on stepped (410) surfaces of Ni and Cu, Surface Science, 338 (1995) 11-18.

[74] D.A. McQuarrie, Statistical Mechanics, University Science Books, 2000.

[75] R.d. Levie, Estimating Parameter Precission in Nonlinear Least Squares with Excel's Solver, Journal of Chemical Education, 76 (1999) 1594-1598.

[76] L.J. Gillespie, L.S. Galstaun, The palladium-hydrogen equilibrium and palladium hydride, J. Am. Chem. Soc., 48 (1926) 1207-1219.

[77] M. Johansson, E. Skulason, G. Nielsen, S. Murphy, R.M. Nielsen, I. Chorkendorff, Hydrogen adsorption on palladium and palladium hydride at 1 bar, Surface Science, 604 (2010) 718-729.

[78] L.L. Jewell, Review of absorption and adsorption in the hydrogen-palladium system, Applied Catalysis A: General, 310 (2006) 1-15.

[79] A.C. Switendick, Hydrogen in Metals I, Springer-Verlag, Berlin, 1978.

[80] R. Lasser, K.H. Klatt, Solubility of hydrogen isotopes in palladium, Physical Review B, 28 (1983) 748-758.

[81] T.B. Flanagan, The Palladium-Hydrogen System, Annu. Rev. Mater. Sci., (1991) 269-304.

[82] A. Roudgar, A. Gross, Hydrogen adsorption energies on bimetallic overlayer systems at the solid-vacuum and the solid-liquid interface, Surface Science, 597 (2005) 42-50.

[83] M. Mavrikakis, B. Hammer, J.K. Norskov, Effect of Strain on the Reactivity of Metal Surfaces, Physical Review Letters, 81 (1998) 2819-2833.

[84] E.C. Sykes, L.C. Fernandez-Torres, S.U. Nanayakkara, B.A. Mantooth, R.M. Nevin, P.S. Weiss, Observation and manipulation of subsurface hydride in Pd(111) and its effect on surface chemical, physical, and electronic properties, PNAS, 102 (2005) 17907-17911.

[85] M. Johansson, O. Lytken, I. Chorkendorff, The sticking probability of hydrogen on Ni, Pd and Pt at a hydrogen pressure of 1 bar, Topics in Catalysis, 46 (2007) 175-187.

[86] H. Okuyama, W. Siga, N. Takagi, M. Nishijima, T. Aruga, Path and mechanism of hydrogen absorption at Pd(100), Surface Science, 401 (1998) 344-354.

[87] M. Johansson, O. Lytken, I. Chorkendorff, The sticking probability of H_2 in presence of CO on some transition metalsat a hydrogen pressure of 1 bar, Surface Science, 602 (2008) 1863-1870.

[88] P.A. Gravil, Hydrogen, sulphur and chlorine coadsorption on Pd(111): a theoretical study of poisoning and promotion, Surface Science, 430 (1999) 176-191.

[89] W. Huang, S.M. Opalka, D. Wang, T.B. Flanagan, Thermodynamic modelling of the Cu-Pd-H system, Computer Coupling of Phase Diagrams and Thermochemistry, 31 (2007) 315-329.

[90] H.S. Fogler, Elements of Chemical Reaction Engineering, Prentice-Hall International, Inc., 1999.